COMPLEX SHEAR MODULUS RECONSTRUCTION USING ULTRASOUND SHEAR-WAVE IMAGING

BY

MARKO ORESCANIN

DISSERTATION

Submitted in partial fulfillment of the requirements
for the degree of Doctor of Philosophy in Electrical and Computer Engineering
in the Graduate College of the
University of Illinois at Urbana-Champaign, 2010

Urbana, Illinois

Doctoral Committee:

Professor Michael F. Insana, Chair
Professor William D. O'Brien, Jr.
Professor Stephen A. Boppart
Associate Professor Paul S. Carney

ABSTRACT

Many pathological processes in tissues are recognized by morphological changes that reflect alterations of the soft tissue mechanical properties. Ultrasound shear-wave imaging can provide quantitative information about soft tissue mechanical properties, specifically the complex shear modulus. Advancing this field has the potential to bridge molecular, cellular, and tissue biology and to influence medical diagnoses and patient treatment. This dissertation describes several quantitative developments in the field of ultrasound shear-wave imaging. The initial study is a time-domain method for quantitative reconstruction of the complex shear modulus, estimated from the tracked displacement of the embedded spherical scatterer. This study also established a methodology for independent experimental verification of estimated material properties using rheometer measurements. The second study presents a technique for shear-wave imaging using a vibrating needle source for shear wave excitation. An advantage of such an approach is extended bandwidth of the measurement and a well-defined shear wave propagation that can be advantageous in the complex shear modulus reconstruction. This method was used to explore viscoelastic mechanisms in liver tissue and to explore different modeling approaches. It was found that the shear dynamic viscosity provides more contrast in imaging thermal damage in porcine liver, as compared to the shear elastic modulus. The third study was to develop an FDTD 3D viscoelastic solver capable of accurate modeling of shear wave propagation in heterogeneous media. Numerical results are experimentally validated. Furthermore, this numerical framework is used to study complex modulus imaging, specifically a direct algebraic Helmholtz inversion. The practical limitations and complex shear modulus reconstruction artifacts were studied, where it was found that distortions can be minimized simply by imaging the magnitude of the complex shear modulus. The final study was a recursive Bayesian solution to complex shear modulus recon-

struction. A result of this is a stochastic filtering approach that uses *a priori* information about spatio-temporal dynamics of wave propagation to provide low variance estimates of the complex shear modulus. The stochastic filtering approach is studied both in simulation and experiments. The benefit of such an approach is low variance online reconstruction of the complex shear modulus per imaging frequency.

To Maksim and Mara, my family and friends

ACKNOWLEDGMENTS

I would like to extend my gratitude to my adviser, Dr. Michael F. Insana, for his guidance during the course of this work. His valuable suggestions, patience and motivation contributed to the successful completion of my dissertation. He believed in my scientific ability, challenged my work and encouraged me to pursue my ideas during the time we worked together. I am also very grateful to Dr. William D. O'Brien Jr., whose advice and insights were invaluable to my work. Also, I would like to thank the other committee members, Drs. Stephen A. Boppart and Paul Scott Carney, for their valuable assistance and participation.

The Ultrasonic Imaging Laboratory under the supervision of M. F. Insana has been instrumental in the successful completion of this work. I would like to acknowledge Dr. K. S. Toohey, Dr. S. Kalyanam, R. Yapp, D. Mahr, Y. Wang and M. A. Qayyum for their scientific input to my research and for the work that we have published together. Without their input this dissertation could not have been completed.

Lastly, but not least, I am grateful for the unconditional love and support from my family. My deepest gratitude to my Uncle Mikaš who encouraged me to pursue graduate education in the USA and who made this possible for me. I would like to thank my beloved wife Mara for all the love and support I could ask for and for the sacrifices she made to allow me to achieve this goal. My only hope is that I will be able to provide the same loving and unselfish environment during the course of your studies. I dedicate this work to my son Maksim and my wife Mara who were the sole inspiration to complete this dissertation.

This research was supported in part by the National Science Foundation through TeraGrid resources under grant number [TG-DMR080068N] and the National Cancer Institute under award number R01 CA082497.

TABLE OF CONTENTS

LIST OF TABLES

LIST OF FIGURES

LIST OF ABBREVIATIONS

AHI	Algebraic Helmholtz Inversion
EKF	Extended Kalman Filter
ESR	Elastic Sphere Radiometer
KF	Kalman Filter
K-V	Kelvin-Voigt
MAP	Maximum *a posteriori*
MLEF	Maximum Liklehood Ensemble Filter
MRE	Magnetic Resonance Elastography
MRI	Magnetic Resonance Imaging
OCT	Optical Coherence Tomography
PRF	Pulse Repetition Frequency
RF	Radio Frequency
SNR	Signal-to-Noise Ratio
URI	Ultrasound Research Interface
US	Ultrasound
WGN	White Gaussian Noise

CHAPTER 1

INTRODUCTION

1.1 Background

It is well known that tissue pathology is strongly correlated with changes in mechanical properties. One of the earliest diagnostic tools is palpation, the routine physical examination process used by physicians to distinguish between normal and abnormal tissues. Palpation is a method for qualitative estimation of tissue elasticity. A recent clinical study reports that up to 43% of detected breast cancers were detected via palpation compared to 57% detected by mammographic screening [1]. Some of the problems associated with clinical palpation are that it is subjective, dependent on the proficiency of the clinician, and detection is limited by lesion size and depth [2, 3]. Therefore, there exist compelling scientific and practical reasons for developing an imaging modality using contrast in elasticity of the underlying tissue to produce images. The ultimate goal of any elasticity imaging modality is to spatially map soft tissue mechanical properties. The advantages of an elastic image should be reproducibility and a quantitative, objective representation of a soft tissue mechanical properties.

Sources of contrast in elasticity imaging can be divided into physical and biological sources. Physical sources of elasticity contrast are related to the spatial variations in flow velocity of fluids through the extracellular matrix (poroelasticity) and the rate at which the matrix itself mechanically relaxes (viscoelastic) in response to applied forces [4]. On the other hand, biological sources of elasticity strain contrast result from biological changes in the tissue and are poorly understood. For example, in mammary tissues they include edema, hyperplasia, acidosis, fibrosis, desmoplasia and inflammatory responses characteristic of the reaction of breast stroma to cancer cells [5]. Pathological changes generally correlate with changes in tissue stiffness, but

there exists no theoretical framework linking these pathological changes to the exact mechanical behavior at a mesoscale tissue level larger than the cell but smaller than the organ. Many of the hallmarks of human cancer and pathological processes are recognized based on the morphological changes that have roots in biophysical changes that reflect the change of the mechanical parameters of the tissue. The evolution of this field has the potential to bridge molecular, cellular, and tissue biology and lead to new approaches in the treatment of patients [6]. In this thesis we focus on developing methods that can facilitate estimation of the mechanical parameters of the tissue because they have the potential to be directly implicated in medical diagnoses and patient treatment.

Common imaging modalities used in elasticity imaging are ultrasound (US), magnetic resonance imaging (MRI) and optical coherence tomography (OCT). These techniques have shown promise for discrimination between benign and malignant breast lesions [7, 3], for liver fibrosis staging [8, 9], assessing elasticity of myocardium [10], prostate cancer screening [11], and probing the rheological properties of the human brain to diagnose subtle neurodegenerative processes [12], to name a few. The diagnostic value of elasticity imaging stems from the important role of the cellular mechanoenvironment in regulating disease progress, such as tumor growth [13], and from the large contrast observed between various mechanical properties of normal and disease-affected tissue [14, 11, 10, 9].

In this thesis work we will focus on US elasticity imaging. Pulsed-echo ultrasound systems have a unique ability to survey the human body due to the capability of compressional acoustic waves to penetrate deep into soft biological tissues. Meaningful images of the human body are formed from backscattered and reflected signals. One of the most common approaches to image formation in US is the so called B-mode imaging, where the backscattered energy is qualitatively mapped and range gated into images that can produce contrast between different media. These contrasts in US images correspond to the changes in the acoustic impedance of the medium and correspond to brighter or darker regions in the B-mode images. Although qualitative, these observations provide a very powerful diagnostic tool to physicians. During the majority of US exams patients are not exposed to any risks; this is in contrast to imaging technologies involving ionizing radiation, which are known to have quantifiable risks [15].

The variations in bulk modulus for soft biological tissues are in a relatively small range, 10^9 - 10^{11} Pa [16], so compression wave imaging may not always provide the contrast needed to differentiate different tissue types. On the other hand, shear modulus for the soft biological tissues spans a much larger range compared to the bulk modulus, 10^3-10^6 Pa [16]. Therefore, shear modulus could possibly add information to the compression wave based imaging and provide additional contrast for tissue differentiation.

In this thesis the focus is on developing methods for studying complex shear modulus of soft biological tissues and tissue-like materials. This chapter provides the background motivating the quantitative estimation of the complex shear modulus. In Section 1.2 elasticity imaging is introduced and a literature review is provided with emphasis on dynamic methods for shear wave imaging. The need for the complex shear modulus reconstruction is motivated in Section 1.3. Specific aims and conducted research of this thesis are delineated in Section 1.4. Finally, in Section 1.5 the outline of this dissertation is provided.

1.2 Elasticity Imaging

Rheological properties of soft biological tissues are of great importance in medical diagnoses [7, 10] and can be measured using elasticity imaging. Specifically, we focus on the complex modulus, which, with mass density, governs the mechanical wave propagation through soft tissue. Elasticity imaging modalities are a set of techniques for estimating rheological properties of soft biological tissues by modeling the tissue stress-strain relationship as a function of externally applied stress [17].

Elasticity imaging is characterized by several general steps in which the tissue of interest is mechanically stressed, by either external or internal forces, by various methods. Moreover, tissue movement induced by these forces is measured via a phase-sensitive instrument such as ultrasound (or MRI, OCT, etc.) by estimating either a displacement or velocity of the displaced tissue [17]. In the case of US imaging, one can use a broad-band method to collect time-series data and cross-correlation approach to estimate the distance between returned echo fields.

Another approach is to use narrow-band excitations and use pulsed Doppler

method to estimate the mean velocity within the resolution volume. While the cross-correlation method has intrinsically higher resolution compared to the Doppler method, it is subjected to ultrasonic speckle decorrelation induced by out-of-plane motion, non-uniform motion of sub-resolution scatterers, non-uniformity of the ultrasound field and non-rigid tissue deformation leading to loss of echo signal coherence and displacement estimation errors [5].

Doppler estimation of displacement or velocity is characterized by lower resolution but with higher sensitivity to phase changes that can mitigate some of the spatial problems associated with cross-correlation estimation. This is because Doppler estimation is a volumetric measure of the mean motion. From collected time-series data, rheological parameters of tissue are reconstructed quantitatively [18, 19, 20] or qualitatively [21] from the estimated motion.

There are several ways to estimate rheological properties of tissues from the displacement or velocity time-series data. One approach is to use a direct inversion of the wave equation, where the wave equation can be expressed as a function of displacement or velocity and material parameters. Assuming local homogeneity of the material properties, the wave equation can be inverted locally (per pixel) from the collected time-series data to reconstruct viscoelastic material properties [22] per shear wave frequency. Such an approach requires knowledge of the 3D spatial distribution of displacement/velocity for a full 3D inversion. This is not always practical nor feasible; thus, direct inversions are often approximated from 1D or 2D fields which inherently introduce biases and reconstruction artifacts in the inversion process.

Another approach is the phase gradient method [18], where from the collected time-series data of displacement or velocity a spatial phase gradient can be calculated. Spatial phase gradient is directly related to shear wave speed. In order to reconstruct viscoelastic material properties, shear wave velocities are estimated over several frequencies to obtain a frequency-dependant dispersion curve. By fitting the dispersion curve, viscoelastic material properties are estimated. The displacement can be induced by quasi-static compression [3] or dynamic vibration [23, 24, 25].

In this work pulsed Doppler ultrasound methods are used to detect tissue motion induced by dynamic vibration. Different approaches are explored for material properties reconstruction that include both phase gradient and

algebraic inversion method. Emphasis is on the quantitative complex shear modulus estimation using dynamic methods.

1.2.1 Dynamic Elasticity Imaging

In general, dynamic methods for elasticity imaging can be divided into two categories based on the excitation approach. The excitation approach can be through either external or internal excitation methods. External excitation methods are where the vibration of the medium is induced on the boundaries of the body. Internal excitation methods are where the vibration is either remotely induced within the object, such as the acoustic radiation force approach [24, 18, 26] or the magnetomotive force [25], or the mechanical energy of vibration is coupled via a needle inserted into body tissues [20, 27].

External Methods of Inducing Shear Waves

External methods for shear wave excitation are characteristic of MRI-based imaging techniques. These techniques are in general termed magnetic resonance elastography (MRE). Manduca et al. [22] developed a shear wave imaging technique based on the external vibrator capable of exciting harmonic or transient shear waves in the frequency range of 10-1000 Hz. Spatio-temporal wave properties are captured over a volumetric acquisition. Material properties are obtained by localized direct inversion of the wave equation. For such an approach all three components of the velocity vector must be collected over several periods of the excitation signal. This approach can be used to reconstruct viscoelastic material properties.

However, the majority of applications are based on elastic inversion. The direct inversion approach is widely accepted in the MRI community and numerous studies have been conducted in characterizing tissue material properties. McCracken et al. [28] used both transient and harmonic shear wave approaches to study brain stiffness *in vivo* and found that both methods estimated white matter to be stiffer than gray matter. Sinkus et al. [29] used low-frequency mechanical waves to study viscoelastic shear properties of *in vivo* breast lesions. Based on the sample of 15 patients he was able to differentiate between benign and malignant lesions based on the contrast in the elastic modulus. They estimated the elastic shear modulus of malignant

tissue to be three times larger than the elastic modulus of fibroadenoma or the surrounding breast tissue. On the other hand, reconstructed dynamic viscosity did not yield contrast for the differentiation between the different tissue types.

Siegmann et al. [30] conducted a similar clinical study to determine the value of MRE in addition to contrast-enhanced MRI. They found that the combination of MRE and MRI increased diagnostic performance of the exams. In the study, low-frequency mechanical shear waves at 85 Hz were excited. A recent clinical study by Venkatesh et al. [31] targeted elastography of liver tumors. Statistical analysis was performed on the stiffness values for differentiation of normal liver, fibrotic liver, benign tumors, and malignant tumors. They found that malignant liver tumors had significantly higher mean shear stiffness than benign tumors, fibrotic liver and normal liver tissue. Moreover, they report that fibrotic liver had values overlapping with both malignant and benign tumors. Low-frequency shear waves at 60 Hz were used in this study for forming stiffness images.

One of the main drawbacks of the external methods for the excitation of the shear waves is a low-frequency limit of the technique. High attenuation of the shear waves limits the ability of higher frequency waves to propagate to the organs far from the body surface. Moreover, long acquisition times of MRI limit the method to the acquisition of one single harmonic < 100 Hz. It has been reported in the literature that the 3D acquisition time for MRI is not applicable for clinical use, and that most studies use 1D or 2D based estimation to shorten the acquisition time [32, 30].

External, dynamic methods, have been used by the ultrasound community as well. Catheline et al. [33] studied a plane shear wave propagation in gelatin phantoms and beef muscle *in vitro* and demonstrated that these methods can enable one to quantify viscoelastic properties. They used a 1D direct inversion approach and frequency bandwidth of 50-500 Hz. They used a custom-developed ultrasonic scanner capable of imaging at a rate of 3000 frames/s (100 times higher than conventional scanners) to detect fast tissue motion induced by low frequency shear waves.

Internal Methods

There are several approaches of internal shear wave excitation. Material displacement within the object can be produced by a needle or a glass rod vibration [20, 18, 34]. Chen et al. [18] used this approach to estimate shear complex modulus of the beef muscle using shear wave imaging. They were able to study anisotropy of the bovine muscle to find that shear wave speed is grater along the muscle fiber than across of it. He provided estimates of the complex shear modulus for both directions.

Yin et al. [34] used a needle driver to estimate elastic material properties of hepatic fibrosis in an animal model using MRE. They demonstrated that the shear stiffness of liver tissue increases systematically with the extent of hepatic fibrosis. This approach, although invasive, can produce strong displacements in the 10-500 Hz range. However, the methods are limited by the mechanical actuator properties and the possibility of needle slippage for higher frequencies and displacements.

Others have used acoustic radiation force, either by displacing large scattering objects or weakly scattering media such as tissue. Both approaches are based on transferring momentum from an acoustic compressional pulse through scattering or absorptive interaction between the wave and the tissue [35, 36]. Ilinskii et al. [37] developed a theoretical framework for estimating material properties from displaced gas bubbles and spherical scatterers. They were able to quantitatively estimate elastic properties of hydrogel phantoms.

A similar approach was taken by Chen et al. [38], who estimated viscoelastic properties of the gelatin phantoms in the frequency range up to 1 kHz. These methods can be used to estimate the material properties of the medium, shear modulus, surrounding the sphere. A drawback of the approach is that a spherical inclusion has to be either placed in the material or produced in it as in the case of the gas bubbles [37]. This method provides spatially averaged information from the volume surrounding the displaced object.

A different approach was taken by Nightingale et al. [24] who used focused ultrasound to apply localized radiation force within tissue, so called ARFI (acoustic radiation force impulse imaging), where wave momentum is transferred via attenuation. Resulting tissue displacements are mapped using ultrasonic correlation based methods. The tissue displacements are

inversely proportional to the stiffness of the tissue, where a stiffer region of tissue exhibits smaller displacements than a softer tissue region. This is a qualitative assessment of the elasticity. Several other methods based on the ARFI approach have been developed and few of them are implemented in the clinical systems.

Bercoff et al. [26] describes an ARFI based technique, named supersonic shear imaging (SSI), that has been implemented in clinical system. Their approach is to create a quasi-plane shear wave using consecutive acoustic radiation force excitations and to image resulting particle displacements using an ultra-fast, ultrasonic scanner (5000 frames/sec). They are able to provide elastic modulus images of the material properties. Recently, they expanded the proposed method to develop shear wave spectroscopy (SWS) [39, 32] that is capable of providing point reconstructions of viscoelastic material properties from an ROI.

A different approach was to ARFI imaging wast taken with Virtual Touch tissue quantification that has been introduced by Siemens (Siemens AG, Germany) and is still not commercially available as a feature on the systems sold in the USA. Fierbinteanu-Braticevici et al. [40] used the Virtual Touch feature of the Acuson S2000 (Siemens AG, Germany) system in a clinical study to measure shear wave velocities within the ROI of fibrotic livers. They report that they were able to successfully stage liver fibrosis using the proposed method. The Siemens system is only capable of providing information about the elastic modulus or the shear wave speed.

The ability to produce shear waves locally within the imaging media provides the means for better material properties estimation compared to external methods. There are several reasons for this. Deep-lying tissue can be imaged over larger bandwidth of the shear wave excitations compared to the external excitations where in practice excitation frequencies are smaller than 100 Hz. Sterile environment can be preserved with noninvasive, remote excitation, such as in case of ARFI techniques. Moreover, locally well-defined wave propagation enables accurate estimation of material properties compared to external excitation where wave characteristics can be significantly changed due to the propagation path.

Limitation of the reviewed internal methods are dependant on the specific implementation. Challenges in applying these techniques include generating sufficient radiation force to measurably displace deep-lying tissues of a broad

range of stiffnesses, invasive nature of the needle vibrator, tracking small tissue displacements and, where possible, meeting the Food and Drug Administration (FDA) safety recommendation for the spatial-peak temporal-average intensity of 0.72 W/cm^2 *in situ* [41] for ARFI based imaging systems.

1.3 Complex Shear Modulus

Mechanical wave propagation in tissues is governed by mechanical tissue parameters in unbounded media. Specifically, harmonic shear mechanical wave propagation is governed by the complex wave number [42], which depends on frequency, mass density, and complex shear modulus. Changes in mass density and the complex shear modulus represent a direct influence on the wave propagation.

Quantitative estimation of a complex wave number of soft biological tissues generally requires estimation of mass density and shear modulus. Estimated values of mass density of soft biological tissue are within a narrow range of $\rho = 971 - 1220$ [kg/m^3][43, 44, 45, 46]. For lipid-based tissues, density is slightly lower, $\rho = 920 - 970$ [kg/m^3], and for collagen-based tissues, density is slightly higher, $\rho = 1020 - 1100$ [kg/m^3]. These values represent the compilation of results using different estimation methods. Thus, realistic variation in density between tissues can be even smaller. Depending on the tissue structure being tested for shear material properties, density information might not provide the contrast desired for differentiation between different tissues. Therefore, it is common practice to assume in the reconstruction of the complex shear modulus that the mass density is spatially uniform and equal to the mass density of water, $\rho = 1000$ [kg/m^3]. Consequently, estimation of the complex wave number reduces to estimation of the complex shear modulus. Within this thesis we will focus on the quantitative reconstruction of the complex shear mechanical modulus.

One of the fundamental questions that should be asked is: Why do we want to reconstruct the complex shear modulus? Although, from wave physics it follows that wave propagation in viscoelastic media is characterized by the complex shear modulus, most of the reported results are based on the reconstruction of the real component or the elastic shear modulus.

The complex shear modulus describes the frequency dependence of ma-

terial parameters. The relationship between the stress and strain for a linear viscoelastic solid can be defined by a complex modulus $\sigma/\epsilon = G(\omega) = G' - iG''$, where σ is the stress and ϵ is the strain. Exact mathematical forms of G', the storage modulus, and G'', the loss modulus, are determined by the assumed underlying mechanical model of the material [47]. As an example, for a Kelvin-Voigt model $G(\omega) = G' - iG'' = \mu - i\omega\eta$, where μ is the elastic shear modulus, ω is the angular frequency and η is the dynamic shear viscosity. Two common ways of estimating complex modulus parameters are by inversion of the dispersion equation [18, 48, 20] or by the local algebraic inversion method [22].

Moreover, specific techniques are further differentiated based on whether the inversion of the stress-strain relationship aims only at reconstructing elastic material parameters or focuses on realistic viscoelastic behavior. It was reported in the literature that although stiffness is correlated to pathology, it is not a sufficient criterion for diagnosis [39]. Other mechanical parameters such as shear viscosity could be very useful for increasing the mechanical contrast in measurements [49]. Very little is known about the dynamic shear viscosity of tissue or its diagnostic value.

One of the main reasons that most of the current clinical studies are conducted using elastic assumptions about the shear modulus is the lack of evidence in the literature that the loss modulus, G'', carries diagnostic information. In the literature, there exist only a few examples where the benefit of reconstructing the loss modulus has added value to the material properties reconstruction.

Huwart et al. [9] conducted a study to assess the feasibility of using non-invasive MR elastography for determining the stage of liver fibrosis. A clinical study was conducted on 25 patients who had liver biopsy for suspicion of chronic liver disease. MR elastography was performed by transmitting 65 Hz mechanical waves into the liver and material properties were reconstructed using a direct wave inversion approach. They demonstrated that the mean shear viscosity was significantly higher in the patients with cirrhosis (5.19 ± 1.85 Pa·s) than in the patients without cirrhosis (2.39 ± 0.86 Pa·s).

Chen et al. [18] conducted a study on estimating the complex shear modulus of *in vivo* porcine liver. They used an ultrasound shear wave imaging technique based on the estimation of shear wave dispersion for the reconstruction of material properties. The estimated the mean and standard deviation

of elastic and viscous constants obtained from nine different measurements to be $\mu = 2.2 \pm 0.63$ kPa and $\eta = 1.96 \pm 0.34$ Pa. Moreover, via intra-lab comparison, they compared estimated results to in vivo values reported for normal human liver ($\mu = 2.06 \pm 0.26$ kPa and $\eta = 1.72 \pm 0.15$ Pa· s) and normal rat liver ($\mu = 1.76 \pm 0.37$ kPa and $\eta = 0.51 \pm 0.04$ Pa·s). Based on the reported values it follows that there is no statistically significant difference in the mean estimated elastic modulus between the different species. However, based on the viscosity, normal rat liver can be differentiated from the normal porcine and human livers. Differentiation between normal human and porcine liver is not possible.

In contrast there are several studies conducted with results not supporting the evidence of the added value of information in the viscosity reconstruction. As an example, Sinkus et al. [29] conducted an MR elastography study on *in vivo* breast lesions. They tested six breast cancer cases, six fibroadenoma cases and three mastopathy. The *in vivo* results showed a good separation between the cancer cases and benign fibrotic cases based on the mean estimated shear elastic modulus. However, results obtained on the shear viscosity were not shown to be useful for separating malignant from benign lesions.

Providing evidence of an added value of information in reconstruction of the loss modulus can motivate further studies to determine quality of the loss modulus or dynamic viscosity (in the case of KV model) as a diagnostic parameter. Ultimately, contrast to variability (whether from noise or biologic variability) determines the quality of a parameter for specific diagnosis, not just the contrast.

1.4 Specific Aims and Research Conducted

The overall goal of this work is to design shear wave imaging techniques that can facilitate quantitative estimation of mechanical properties, specifically a complex shear modulus. Moreover, evidence is provided of added information value in the loss modulus or the imaginary component of the complex modulus. Spatial maps are provided, in both 2D and 3D, of the reconstructed complex shear modulus. The approach here is comprehensive. It includes experimental studies, analytical studies and the numerical simulations. The experimental approach is based on internal excitation of displacement within

soft tissues and tissue-like materials. By having well-characterized shear wave excitations with large displacements of the material, a better detection SNR is obtained, which benefits estimation of the material properties. Moreover, this approach makes it possible to address a broadband response of the material, enabling understanding of viscoelastic mechanisms within the bandwidth of the measurement.

Ultrasound is used to detect tissue movement. Specifically, the Doppler feature of ultrasound is used to detect tissue displacements. There are many reasons to use ultrasound for this work. Ultrasound is readily available at medical institutions. It is portable, inexpensive and minimally invasive compared to other modalities, which renders it desirable for diagnostic purposes. However, ultrasound is not without limitations. Shear wave propagation is a 3D phenomenon characterized by a three-component velocity vector, and current systems can detect only one component of that vector. Nevertheless, if a quantitative estimate of the complex shear modulus can be provided, medical diagnosis can benefit.

While others seek diagnostic methods, we seek to understand the basic science, and that enables our use of more invasive methods for applying forces. Nevertheless, proposed methods under specific conditions can complement current biopsy procedures and be implemented in clinical settings.

The general accomplishments of this dissertation are:

- Developed analytical and experimental framework for quantitative complex shear modulus estimation from dynamic tissue stimulation.
- Validation of estimated complex shear modulus using independent measurements.
- Developed numerical framework capable of representing shear wave propagation in heterogeneous materials.
- Provided evidence of the added value in the viscosity reconstruction.

The focus of this thesis is to design a shear wave imaging technique that can facilitate quantitative estimation of a complex shear modulus. In vivo studies designed to discover sources of elastic contrast that are related to disease processes are very difficult to conduct because soft biological tissues are heterogeneous, anisotropic, non-linear media with poorly defined boundaries

and complex internal stress fields. Therefore, in order to develop methods for quantitative material property estimation, a well-understood material is needed. The majority of the studies were conducted on homogeneous collagen hydrogels that share key structural and mechanical features of natural and engineered tissues [50]. Several studies were conducted using inhomogeneous phantoms both *in vitro* and *in silico*. This dissertation addresses the complexity of the quantitative material properties estimation of soft biological tissue in the porcine liver case study [49] *ex vivo*. In this dissertation independent validation of our methods is sought through rheometry, but often such validation is difficult to achieve. However, there is a growing body of published results that provide interlab comparisons, and this was used to validate results. Immediate aims are to show that quantitative measurements of the material properties can be made and to investigate the complexity of the material model needed to quantify behavior of the soft biological tissues at the testing bandwidth. The long term goal is to understand how biological sources of contrast in elasticity imaging alter the dynamics of perfused soft-tissue deformation and the value of the diagnostic information embedded in the observed contrast.

1.5 Outline of this Dissertation

The rest of this document is organized as follows. Chapter 2 is a study on the calibration of the acoustic radiation force [51] and the excitation methods defining augmentation of scattering properties of the material as a desirable approach toward acoustic radiation force excited shear wave propagation. This chapter is based on the paper presented at the Society of Photo-Optical Instrumentation Engineers (SPIE) meeting [51].

The problem of complex shear modulus reconstruction from acoustic radiation force step response is explored in Chapter 3. This study was motivated by the results obtained in Chapter 2. Knowing that the displacement of the hard inclusion depended not only on the radiation force but on the surrounding material properties, we proposed a method for reconstructing complex shear modulus from the tracked displacement of the embedded spherical scatterer [19, 52]. Underlying theoretical concepts are reviewed and the possibility of quantitative complex shear modulus reconstruction is explored.

Chapter 3 is modified from a paper published in the *Journal of the Acoustical Society of America* [19].

Chapter 4 is an exploration of dynamic shear wave excitation using a needle as a source. A limitation of the approach in Chapter 3 was that in order to estimate material properties using the proposed method, one would have to have an ability to embed a spherical scatterer. Moreover, the proposed method was bandlimited to <200 Hz. By using a needle source, first, we extended the bandwidth of the measurement, and second, a well-defined shear wave propagation can be used to our advantage in the material properties reconstruction. Chapter 4 is modified from a paper published in the *IEEE Transactions on Ultrasonics Ferroelectrics and Frequency Control* [20].

Chapter 5 is a direct extension of the Chapter 4. We conducted a study on soft tissue to explore viscoelastic mechanisms in excised liver tissue and appropriate models using the proposed method in Chapter 4. Moreover, the effects of thermal damage on the viscoelastic properties of porcine liver are studied. Chapter 5 is modified from a manuscript to be published in *Ultrasonic Imaging* [49].

In Chapter 6, we describe our efforts to numerically model shear wave propagation in heterogeneous media. Finite difference time domain (FDTD) techniques commonly used in seismology were adopted to develop a 3D viscoelastic solver capable of accurate modeling of shear wave propagation in heterogeneous media. A 3D shear wave imaging experimental method is developed to validate numerical results. Moreover, we adapted 3D direct algebraic inversion of the wave equation to reconstruct underlying complex modulus. Both 2D and 3D spatial mapping of the reconstructed modulus is provided. Chapter 6 is modified from a manuscript recently submitted to the *IEEE Transactions on Ultrasonics Ferroelectrics and Frequency Control.*

A recursive Bayesian solution to complex shear modulus reconstruction is explored in Chapter 7. A novel approach in the field uses *a priori* information about spatio-temporal dynamics of wave propagation to provide lower variance estimates of the complex shear modulus compared to phase gradient and algebraic inversion methods. The proposed estimator is studied numerically and experimentally with a 1D cylindrical wave model in homogeneous materials. Chapter 7 is modified and extended from a paper presented at 2010 IEEE International Ultrasonics Symposium.

Finally, Chapter 8 describes the general conclusions about the develop-

ments presented in previous chapters, and provides an outline of possible future directions derived from this dissertation work.

CHAPTER 2

ULTRASONIC RADIATION FORCES FOR ELASTICITY IMAGING OF 3-D TISSUE MODELS

2.1 Introduction

Contrast mechanisms in elasticity imaging are still poorly understood [53]. There is a need for precise and quantitative methods for elasticity imaging that inherently depend on the ability to displace a sample in a well-defined manner. This chapter describes an acoustic radiation force calibration technique.

In vivo breast studies designed to discover sources of elastic contrast that are related to disease processes are very difficult to conduct because breast tissues are heterogeneous, anisotropic media with poorly defined boundaries and complex internal stress fields. A series of studies using hydropolymers that share some of the structural and mechanical features of breast stroma [50] were conducted. From these studies, a molecular-scaled description emerged that relates changes in microstructure to the viscoelastic features.

However, these gels cannot reveal dynamic functional properties normally associated with malignant progression, metabolism, or responses to treatment; many of these features are assumed responsible for disease-specific viscoelastic contrast.

Alternatively, 3-D cell constructs as "living" elasticity imaging phantoms exist and include a scaffold, like that used in engineered tissues, that hosts live cells. For example, fibroblast cells may be mixed with cancerous epithelial cells in a chitosan or matrigel scaffold. With biochemical encouragement, fibroblasts proliferate, respond to molecular signals, and add collagen that stiffens the polymer as in breast stroma. Correlating the mechanical properties of these polymer gels with cell density, collagen production rates, and

This chapter is adapted from M. Orescanin and M. F. Insana, "Ultrasonic radiation forces for elasticity imaging of 3-D tissue models," *Proc. SPIE*, vol. 6513, pp.OH1-11, San Diego, February 2007. Used with permission.

molecular stimulation and inhibition, provides an isolated system for understanding elasticity contrast.

To image mechanical properties of the polymer gels, we must apply known forces to limited spatial areas. Time-harmonic radiation force methods allow for adjustable stress frequencies to increase the signal-to-noise ratio for mechanical properties relative to quasi-static (ramp-and-hold) and impulse stimuli. These methods also allow force application in sterile conditions.

This chapter describes our initial attempts to design radiation force techniques that deform gels for imaging features of the complex compliance/modulus. This initial study focuses on basic system design and calibration. We begin by considering forces generated under continuous-time plane-wave conditions. Experiments are conducted to test pressure-field calibration procedures and extensions of the theory to pulsed force applications. We study movement of a steel sphere in water (acoustic radiometer) and use video and ultrasonic Doppler methods to measure velocity and displacements that can be related to radiation force. We conclude with estimations of the scaffold deformations possible by applying standard experimental approaches.

2.2 Methods

The goal of the proposed method is to generate a calibrated radiation force that remotely deforms polymers. Acoustic pressure fields exert localized forces with a magnitude that depends on the energy density of the field and the scattering and absorption properties of the polymer medium. The force can be modulated in time by transmitting a series of pressure pulses. We adopted a standard radiometric technique for calibrating the primary radiation force that involves deflection of a steel sphere in water [54].

2.2.1 Acoustic Radiation Force

Consider continuous-time plane pressure waves that are incident on an elastic sphere immersed in a non-viscous fluid (water). The force along the direction of wave propagation is

$$F = \pi a^2 Y \langle E \rangle, \tag{2.1}$$

where πa^2 is the projected area of the sphere, Y is the radiation force function, and $\langle E \rangle$ is the time-averaged energy density. The plane-wave energy density is simply $E = p^2(t)/\rho c^2$, where ρ and c are the mass density of the medium and the longitudinal propagation speed, respectively. The radiation force function Y describes the interaction of the sphere with the field. It is determined by the mechanical properties and the geometry of the object and surrounding medium, and is usually expressed as a function of wavenumber k times sphere radius a. The expression [35] for Y was evaluated numerically in Matlab 7.1 (Mathworks, Inc.) for the physical constants of a stainless steel sphere (steel grade 440 cc) given in Table 2.1. Figure 2.1 shows $Y(ka)$ evaluated in ka steps of 0.01 up to $ka = 25$. We avoided the effects of normal-mode resonances (minima) by selecting a source frequency of 1 MHz and a sphere diameter of 1.5 mm. In water at room temperature, $ka \sim 3.2$.

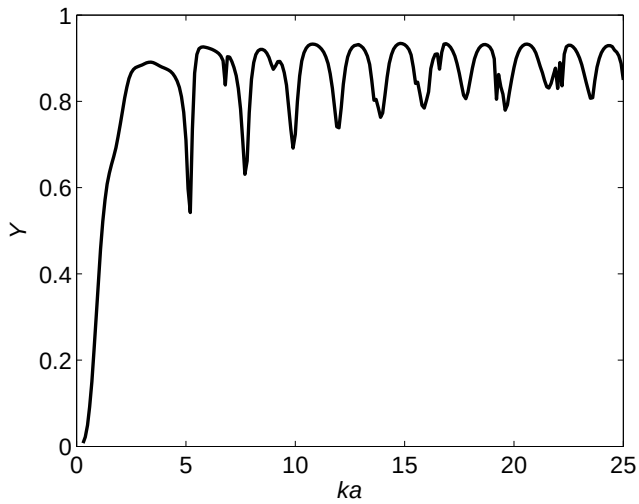

Figure 2.1: The acoustic radiation force function, Y, as the function of ka numerically evaluated for the physical constants given in Table 2.1.

Table 2.1: Physical constants of the steel sphere used to evaluate the radiation force function Y in Fig. 2.1

Density (kg m^{-3})	Compressional Vel. (m s^{-1})	Shear Vel. (m s^{-1})
7809	5240	2978

Equation 2.1 predicts the static force for continuous-time plane waves. Pre-

dictions were possible using measurements of the incident pressure amplitude (in Pa) from a calibrated membrane hydrophone (GEC-Research Ltd., Marconi Research Center, Chelmsford, UK). Predictions were compared with force measurement from an elastic-sphere radiometer (ESR) [54], where the static radiation force F is in equilibrium with the gravitational force mg (Fig. 2.2).

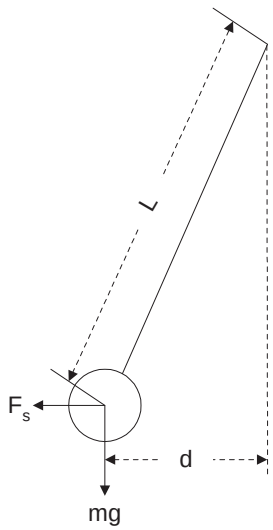

Figure 2.2: Force balance diagram for an elastic sphere suspended in the media in bifilar arrangement.

The relation at equilibrium between sphere displacement d and radiation force F is

$$F = \frac{mgd}{\sqrt{(L^2 - d^2)}} \ , \tag{2.2}$$

where m is the mass of the sphere corrected for buoyancy, g is the gravitational acceleration and L is the length of the thread. The mass of the thread and the adhesive are neglected in the equation.

To measure viscoelastic properties of the material, a dynamic stress field is required. One way to produce a dynamic stress is to use the sum of two narrow-band continuous-wave (CW) pressure fields at frequencies ω_1 and ω_2 where $\Delta\omega = \omega_2 - \omega_1 \ll \omega_1$ [55]. In steady state, the resulting radiation force is $F(t) = F_0(1 + \cos(\Delta\omega t))$; it has static and dynamic components of equal magnitude F_0. The advantage of this approach is that the dynamic force is sinusoidally amplitude modulated at frequency $\Delta\omega$. A drawback of

this method for our application is the large amount of power required by the source transducer to deform the polymers.

We adopted the simpler strategy of using CW bursts at a single frequency. This approach also modulates the force amplitude to generate static and dynamic components. The dynamic force was able to measurably deform the polymer within the power limits of the source, although the dynamic force component has a roughly saw-tooth, rather than sinusoidal time series, as we will show. The radiation force was generated with a 1 MHz, 19-mm-diameter, f/4, broadband, single-element PZT transducer. It was excited with a 1 MHz sinusoidal tone burst voltage of duration s and pulse repetition time T (Fig. 2.3). $T = 2s$ and the nominal frequency of the dynamic radiation force is $1/T$. For example, 50 ms duration bursts yield a dynamic force frequency of 10 Hz. The force frequency can be swept over a broad range to measure the complex compliance spectrum [50], and the transducer can be mechanically scanned across the medium to describe the spatial distribution of properties. The dynamic radiation force was calibrated using ESR techniques. Sphere movements were tracked optically and with Doppler ultrasound.

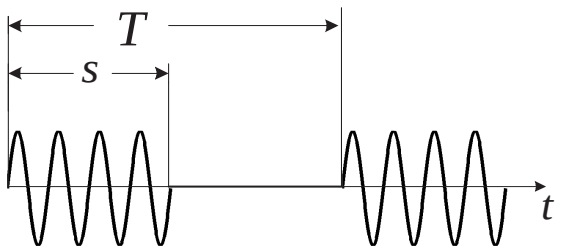

Figure 2.3: Pulsing strategy used for generating dynamic radiation force, where s is the pulse length and T is pulse repetition time.

2.2.2 Optical Method for Measuring Acoustic Radiation Force

Displacement, d, from the static radiation force of a CW pressure wave was measured using a Canon XLH1 HD (high definition) video camera (100 mm EF 2.8 lens). The pixel size of the camera was determined by counting pixels over an image of a ruler. Horizontal and vertical images were acquired in the imaging plane of the sphere and the number of pixels over 1 mm was

counted. The pixel size was found to be 6.10 μm horizontally and 4.55 μm vertically.

Short video clips covering the sphere motion were recorded by the camera in Quicktime format. These clips were later processed using Final Cut Pro 5 software (Apple, Inc.) to produce sequences of uncompressed .tif files, one for each frame. The camera recorded 30 frames per second, where each frame is composed of two interlaced fields. ESR motion was estimated manually by tracking displacement of the sphere between video frames using a matched filter. Due to shutter speed and frame rate limitations of the camera, estimation of dynamic motion of ESR at frequencies greater than 10 Hz were considered unreliable.

2.2.3 Ultrasonic Doppler Method for Measuring Acoustic Radiation Force

Spectral Doppler acquisitions were used to estimate velocity of the sphere during dynamic force applications. Sphere displacement was found by integrating the Doppler velocity over time; the radiation force was found from this displacement estimate using Eq. 2.1. A Siemens Antares Sonoline system using VF5-10 linear array transducer driven by a 7.72 MHz carrier frequency transmitted Doppler pulses. The RF echo signals were recorded using the URI feature of the Antares system and spectral Doppler traces (spectrograms) were computed offline.

The system transmits narrowband Doppler pulses of duration t' on the time interval T_s. The echo signals are digitally sampled by the Antares at 40 Msamples/s. The demodulated complex amplitude V is computed to obtain the in-phase I and quadrature Q components:

$$V(n,k) = I(n,k) + iQ(n,k), \tag{2.3}$$

where $k = 0, 1, ..., M-1$ with M being the number of pulses in the ensemble (slow-time), and $n = 0, 1, ..., P-1$ with P being the number of echo samples recorded after transmitting each pulse (fast-time).

The first moment of the Doppler spectra is an estimate of the mean velocity $\hat{v}$ along the beam axis of the Doppler probe.

The first spectral moment is estimated using the lag-one autocorrelation

estimate [56],

$$\hat{\phi}(n, T_s) = \frac{1}{M-1} \sum_{k=1}^{M-2} V^*(n, kT_s) V(n, (k+1)T_s) \ , \tag{2.4}$$

from which velocity was determined,

$$\hat{v}(n) = \left(\frac{-\lambda}{4\pi T_s} \right) \arg(\hat{\phi}(n, T_s)) \ . \tag{2.5}$$

The RF data were collected using the URI software in spectral Doppler mode, where only one A-line (fixed spatial position) is being continuously sampled. Data were collected in time blocks of 1.2 seconds. At each fast-time sample in the $P = 51$ sample range gate, n, $\hat{\phi}(n, T_s)$ was calculated for the packet of pulses, M. Echo data in the range gate were averaged to obtain one estimate of the autocorrelation function,

$$\hat{\phi}(T_s) = \frac{1}{P} \sum_{n=1}^{P} \hat{\phi}(n, T_s) \ . \tag{2.6}$$

Velocity estimates were also displayed in a spectral Doppler trace. A periodogram was computed for each fast-time sample in some N-point range gate and the results were averaged for display [57]:

$$\hat{S}(f) = \frac{T_s}{MN} \sum_{n=1}^{N} \left| \sum_{k=0}^{M-1} V(n, k) e^{-j2\pi f k T_s} \right|^2 \ . \tag{2.7}$$

2.3 Experimental Results

Experiments were designed to verify the radiation force theory, test for linearity, and explore the feasibility of generating known forces for polymer mechanics experiments. The axes from the single element source transducer and the linear array Doppler probe intersected the 1.5 mm diameter steel sphere at an angle of $\alpha = 30\ ^\circ$. A video camera viewed the scene as illustrated in Fig. 2.4. The acoustic radiation force displaces the sphere from gravitational equilibrium in a direction along the source axis. To compare measured displacements with predictions, we needed to carefully place the

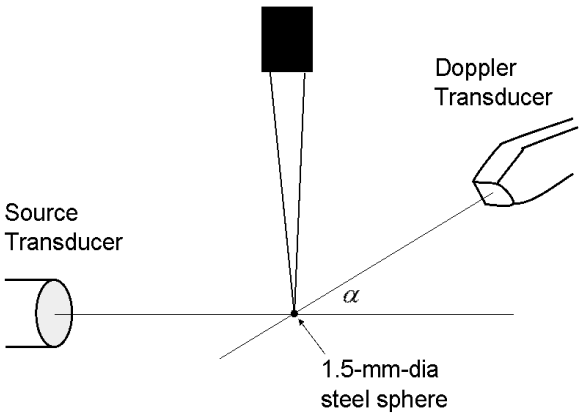

Figure 2.4: Diagram of the source and Doppler transducers relative to the steel sphere as viewed from the video camera.

sphere on the source transducer axis at the radius of curvature where the plane-wave approximation holds. The focal length was found by scanning the 3-D beam profile with a 0.5 mm Marconi hydrophone to find the pressure maximum. We measured a peak pressure amplitude of 91.64 kPa. The water temperature was 21.3 °C where the sound speed is 1487 m s^{-1}. For this geometry, $ka = 3.17$. Substitution of these parameters into Eq. 2.1 predicts a static force of $F = 2.98$ μN.

Sphere motion over time as recorded by the video camera is shown in Fig. 2.5. The steady state displacement is $d = 1.4$ mm for the ESR pendulum length of $L = 47$ mm. Equation 2.2 gives the measured static force of $\hat{F} = 3.51$ μN. Measurement exceeds prediction by 18%.

We also conducted experiments to observe the influence of the pulse length on sphere displacement. The pulse repetition time was held constant ($T = 1.5$ s) while we increased the pulse length from 5 ms to 25 ms to 50 ms. Figure 2.6 shows that longer pulses displace the sphere further, just as expected.

The ESR pendulum is a harmonic oscillator described by a second-order ordinary differential equation (ODE) with constant coefficients. The particular solution of the ODE gives the steady-state displacement that facilitates the comparison between measurement and prediction given above. The homogeneous solution of the ODE, which gives the transient response of the ESR

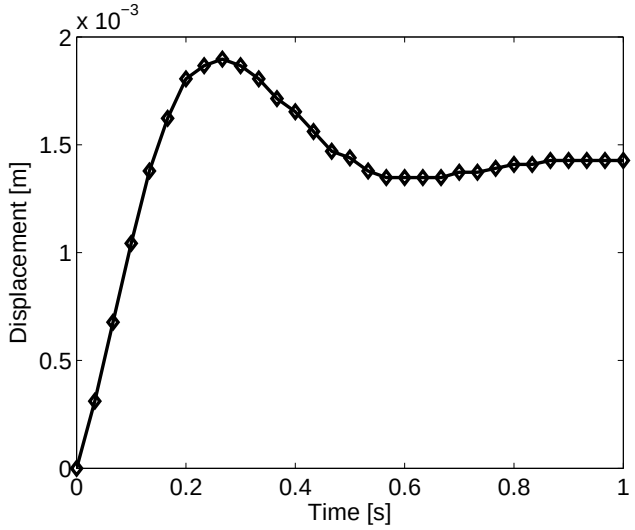

Figure 2.5: Video tracking of the sphere motion for steady radiation forces generated by a CW pressure field.

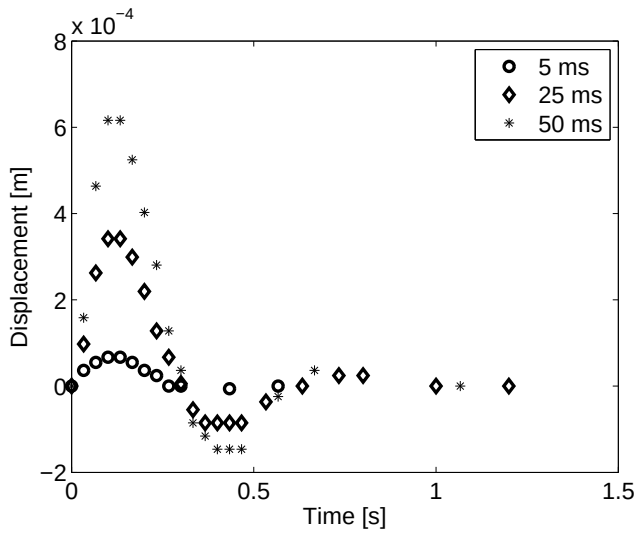

Figure 2.6: Effect of the pulse length s on sphere displacement d for constant pulse repetition time T, where $T \gg s$.

system, seen in Figs. 2.5 and 2.6, will be predicted by simple linear systems analysis if the system was operated in the linear range. Simply stated, linear systems analysis predicts that the displacement-time curve of Fig. 2.5 will be the convolution of the pendulum impulse response $h(t)$ with the applied radiation force function $F(t)$,

$$d(t) = C(s) \int_{-\infty}^{\infty} dt' h(t') F(t - t') \ . \tag{2.8}$$

$C(s)$ is constant with time but a function of pulse length s. The three pulse lengths selected in Fig. 2.6 are much shorter than the period at the resonant frequency of the pendulum (>500 ms). Consequently, the curves in Fig. 2.6 may be considered as scaled impulse response functions of the pendulum, $C(s) \times h(t)$. Applying a step force function $F_0\, u(t)$ as we did experimentally, the normalized predicted displacement curve and measured displacement-time curves are given in Fig. 2.7. The normalized displacement curve is given with

$$d_{norm}(t) = \int_{-\infty}^{\infty} dt' h(t') u(t - t') / d_{max} \ . \tag{2.9}$$

Close agreement validates our assumption of a linear system.

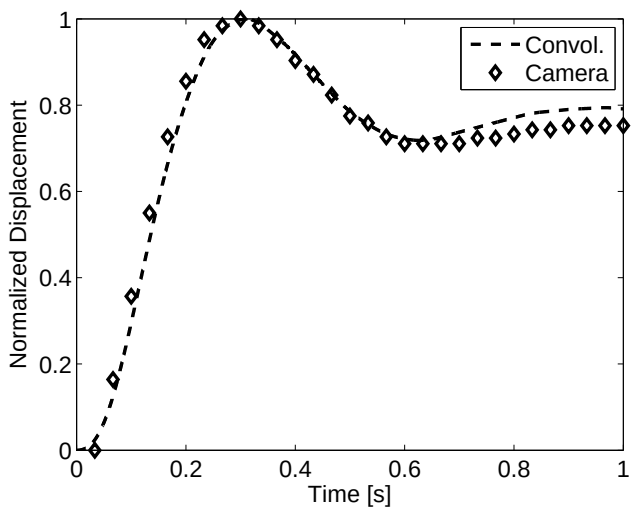

Figure 2.7: Comparison of the observed and predicted ESR sphere displacements. Motion was tracked using the video camera. $s = 50$ ms pulse duration.

The dynamic component of the force was estimated by applying a square-

wave force pulse train generated by a series of CW pressure bursts such that $T = 2s$. The pulse length was varied to span the range of nominal frequencies between 10 Hz and 100 Hz. In Fig. 2.8 we show sphere displacement versus time at 10 Hz. The source-transducer voltage amplitude was 91.64 kPa, the same as for the CW case. It is observed from this figure that the maximum

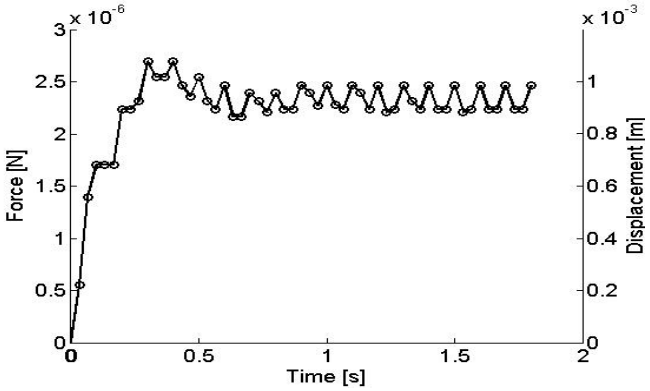

Figure 2.8: Sphere displacement (force) versus time as tracked using the video camera. Applied force frequency = 10 Hz.

displacement in the transition state (from 0 to 1 seconds) is smaller than the maximum in the CW case. The transition band in both cases is of the same length. Once the system reaches steady state, the amplitude of the dynamic component of the force is 0.13 μN. From the figure it can also be verified that the frequency of vibration is 10 Hz. To verify a dynamic component of the force, motion of the sphere was simultaneously observed using Antares Sonoline Doppler system. The Doppler spectral trace of the experiment is presented on the left-hand side of Fig. 2.9.

On the right-hand side of Fig. 2.9 the mean velocity $\hat{v}$ is plotted as a function of time. In both methods, periodogram estimation and pulse-pair processing are implemented on the same data set over the same dwell time with number of pulses M. Both representations of velocity verify the oscillation frequency $f = 10$ Hz of the dynamic component. Since Doppler ultrasound has a much higher rate of sampling than the camera, the influence of different frequencies on the dynamic component of the force was examined. Sampling rate for figures representing estimated mean velocity acquired in Doppler mode is the length of one dwell time (MT_s). Results for

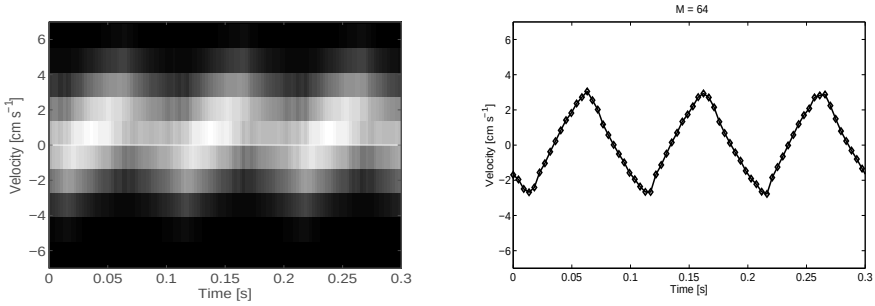

Figure 2.9: (left) The estimated Doppler spectrum. (right) Estimated mean velocity ($\hat{v}$) is presented over the same time period. Both figures represent estimates calculated over the same dwell time with $M = 64$. In the experiment center frequency of the imaging transducer was 7.27 MHz and the PRF was 14204 Hz.

four different frequencies are presented in Fig. 2.10. For the lower frequencies of $f = 12.5$ Hz and $f = 25$ Hz, $\hat{v}$ was estimated over $M = 64$ pulses. For higher frequencies $f = 50$ Hz and $f = 100$ Hz, $\hat{v}$ was estimated over $M = 16$ pulses. It is important to point out that the variance of the estimator is inversely proportional to the number of pulses M that are used for estimation. It can be observed in the above figures that estimated velocity as a function of time, $\hat{v}(t)$, is not a sinusoid function. This motion represents the displacement of a damped oscillator driven by a square wave forcing function with fundamental angular frequency $\omega = 2\pi f$ and $\frac{\omega}{\omega_d} \ll 1$, where ω_d is the angular frequency of the damped motion [58]. Damped motion is caused by the viscous frictional forces within the medium surrounding the sphere. It can also be observed that as the frequency increases, velocity amplitude decreases. Velocity amplitude is directly proportional to the force amplitude; amount of force on the sphere is reduced with the increase in frequency. Estimated ESR motion obtained by optical tracking was compared with the results obtained by the Doppler technique for $f = 10$ Hz. From the displacement curve in Fig. 2.8 at steady state (time interval from 1 s onward), the first derivative over time has been taken to obtain a velocity curve. In order to compare with the Doppler measurements, that curve was interpolated to match the sampling rate of the Doppler system. Further, since measurements were not synchronously collected, the two curves were aligned with respect to their maxima. Moreover, mean value was taken out so that they are zero mean processes.

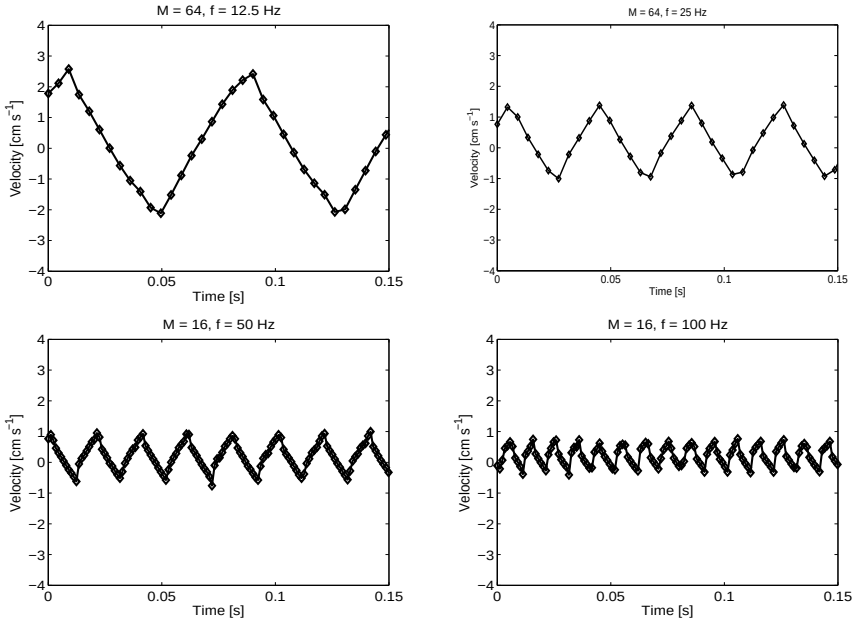

Figure 2.10: This figure illustrates effect of the frequency of the dynamic force on the estimated velocity amplitude.

In Fig. 2.11, a comparison between the two proposed techniques for measuring dynamic component of the motion is presented. Very good agreement

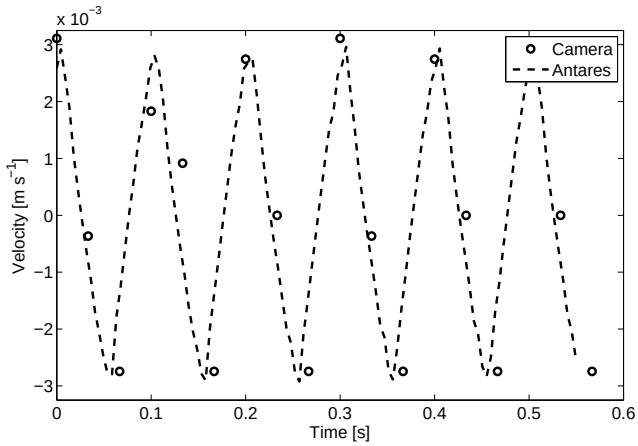

Figure 2.11: Comparison of the estimated velocity of dynamic motion using optical and Doppler methods.

between two measurements, from independent sensors, can be observed.

It can be concluded that the imaging transducer will not influence measurement of the dynamic component of the force. Pulse repetition frequency

used in Doppler measurement is ∼15 kHz; based on the previous results dynamic displacement is negligible. It may bias the result of measuring the static component. For this reason the Antares generated Doppler pulses at the lowest power setting.

Based on the ESR data above, the strain in the polymer was predicted for the same applied radiation forces. Results are shown in Fig. 2.12. Mechanical properties of chitosan and matrigel scaffolds were measured using a mechanical indenter (TA-XTplus, Exponent Stable Micro Systems Ltd., Godalming, UK). For the estimated intervals of stiffness (E), for matrigel (0.8 – 1.4 kPa) and for chitosan (4.3 – 8.0 kPa), the predicted strains are shown in Fig. 2.12. Lower curves for both chitosan and matrigel scaffolds

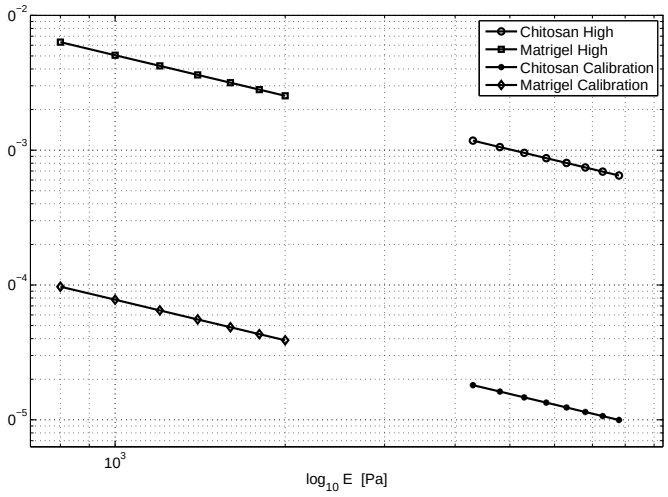

Figure 2.12: Prediction of the sample strains versus polymer stiffness for the forces estimated in the ESR experiments.

represent estimated strain based on the calibration experiment results for 10 Hz oscillation. The lower two curves represent our current capability of straining the polymer materials. By changing from f/4 to f/1 transducer and increasing the excitation voltage by a factor of two, we can maintain linearity and increase pressure amplitude by a factor of 8, which corresponds to the overall increase in force and deformation of 64 times.

2.4 Conclusions

This study demonstrates the feasibility of calibrating both the static and the dynamic ultrasound radiation force using elastic sphere radiometer. The static component of the force was estimated using a high definition video camera. The steady state condition of the static force has been predicted using measured pressure amplitude at the focal point. Disagreement of 18% between the predicted displacement value and the estimated displacement is observed. This disagreement is likely influenced by several parameters. Acoustic pressure measured at the point of maximal intensity where the plane wave approximation is valid is not necessarily equal to the actual acoustic pressure incident on the sphere. The effect of a standing wave forming between the sphere and the transducer can cause a considerable disagreement between the theoretically predicted forces and detected ones [59]. Moreover, PVDF membrane used in the experiments has a variance in pressure estimation of 8% which corresponds to 16% error in force estimation. Thus, 18% difference between predicted displacement value and the estimated displacement is within reasonable error limits. Dynamic radiation force can effectively be produced by exciting a single element transducer with the train of step functions in such a manner that the pulse repetition time is twice longer then the pulse. Motion of the sphere vibrating at frequencies in the range of 10 Hz to 100 Hz was successfully tracked using ultrasound Doppler method. Furthermore, from comparison with the optical method we inferred that the Doppler pulses have negligible influence on the motion of the sphere.

Due to relatively large displacements of the sphere, high (>40 dB) imaging SNR for the tracking and the influence of the sphere's surrounding on the motion of the sphere led to developing a technique that could facilitate material properties reconstruction from the motion of the sphere embedded in the material. In the next chapter, the feasibility of the complex shear modulus reconstruction for practical experimental applications is explored by modeling a time-domain displacement of the stainless steel sphere embedded in the gelatin gel sample.

In this chapter the influence of the viscosity on the motion of the sphere is shown. Damped motion is caused by the viscous frictional forces within the medium surrounding the sphere. This influence cannot be neglected and it must be properly accounted for using an appropriate model. Through the

following chapters of this dissertation realistic and practical models will be discussed that include losses as an important model component needed for quantitative material properties estimation.

CHAPTER 3

MATERIAL PROPERTIES FROM ACOUSTIC RADIATION FORCE STEP RESPONSE

3.1 Introduction

Despite early clinical successes, the visibility of lesions in elasticity imaging can vary widely. Some of the clinical variability may be reduced by improving understanding of elasticity imaging contrast mechanisms and adapting the imaging techniques accordingly. The motivation for the presented approach is to develop a tool to study relationships between the physical and biological sources of contrast across the spectrum of force frequencies used by the various approaches to elasticity imaging. The results from the previous chapter prompted the development of the methods presented here that measure quantitative material properties of hydrogel samples and potentially engineered tissues. Specifically, the complex shear modulus is estimated.

Quasi-static elasticity imaging methods apply a ramp force suddenly and hold it constant while strain is imaged over time [50]. The methods are "quasi-static" for patient imaging because modest forces (1-5 N) are manually applied slowly ($\sim$1 s ramp on) to the breast surface through the ultrasound transducer. Quasi-static methods interrogate tissues at a very low applied-load frequency bandwidth that is bounded from above at approximately 1 Hz and from below at 0.01 Hz depending on the total acquisition time for the strain image recording sequence [60]. At the other load bandwidth extreme are acoustic radiation force imaging methods [24]. A focused push-pulse applies a weak impulse force deep in tissue for about 1 ms, after which displacements are imaged in time as the tissue relaxes. This load bandwidth is nominally 100-1000 Hz depending on experimental details. Other acoustic-based approaches, including ultrasound-stimulated vibro-acoustic spectogra-

This chapter is adapted version from M. Orescanin, K. S. Toohey, and M. F. Insana, "Material properties from acoustic radiation force step response," *Journal of the Acoustical Society of America*, vol. 125, no. 5, pp. 2928-2936, 2009. Used with permission.

phy [61], shear wave elasticity imaging [62], and harmonic motion imaging [63], probe load bandwidths somewhere between these two extremes.

It is difficult to design studies to discover disease-specific sources of elasticity contrast for any of these imaging techniques. In vivo breast tissue properties are spatially heterogeneous, frequently anisotropic, and have poorly defined boundaries. Hence complex internal stress fields are common, making it difficult to even rigorously define a modulus. Excised tissue samples are nonrepresentative because of changes caused by the lack of perfusion, decomposition, or use of fixatives. Gelatin hydrogels are structurally simpler, homogeneous, and able to mimic some properties of breast stroma as required for imaging system development [60]. However, hydrogels do not mimic cell-driven dynamic properties normally associated with malignant progression or responses to treatment; many of these features are assumed associated with tumor contrast.

We are exploring the use of 3-D cell cultures [64]. While they suffer many of the same problems experienced in excised tissue measurements, they have the advantage of containing living mammary cells embedded in hydrogel volumes. The cells can be biochemically or mechanically stimulated and then observed under sterile conditions. Cell cultures do not simulate the tumor macroanatomy, but they can mimic the responses of tumor-cell clusters to their microenvironment. Gels combine geometric simplicity for ease of mechanical measurements with dynamic cellular processes that can be independently verified via optical microscopy.

Many biological tissues and all of the gels we considered are biphasic polymers, which means their mechanical properties are determined by a polymeric matrix (solid phase) embedded in a liquid (fluid phase). The mechanical responses of multiphasic polymers depend significantly on the rate at which force is applied. For example, the complex shear modulus is known to vary widely with force frequency in lightly-crosslinked amorphous polymers [65], breast tissues [23], and even within individual cells of the body [66].

The purpose of this chapter is to establish an experimental and theoretical framework for the estimation of the complex shear modulus from the transient motion of a displaced rigid spherical object. The approach is to use a radiation force technique for estimating shear modulus and shear viscosity of gel types often used in 3-D cell cultures and engineered tissues. These measurements will eventually be made over the bandwidth of force frequen-

cies used in various elasticity imaging techniques. This chapter focuses on the application of Doppler measurements to describe transient dynamic responses of gelatin gels to a step change in radiation force. Particle velocity estimates are related to modulus and viscosity through a second-order rheological model. The results provide an estimate of the impulse response function of shear wave imaging.

3.2 Methods

The goal of the proposed method is to remotely and quantitatively estimate material properties using acoustic radiation force. Acoustic pressure fields exert localized forces with a magnitude that depends on the energy density of the field and the scattering and absorption properties of target media. Gelatin gels are used in this study that describes the measurement system and rheological models applied for material property estimation.

3.2.1 Acoustic Radiation Force

In quasi-static ultrasonic elasticity imaging methods, an external mechanical force is applied to the surface of the medium, and the induced deformation is imaged as strain using speckle tracking methods. Forces applied to the surface result in a spatially diffuse stress-field distribution where boundaries everywhere in the medium affect deformations at each point. Interpretation of strain maps is challenging under these conditions. Alternatively localized stress fields may be applied using acoustic radiation force. By remotely exerting a locally oscillating stress field at the desired frequency, the object responds with an harmonic deformation that is mostly decoupled from the boundaries. The size of the vibrating region and the amplitude and phase of vibration depend on the material properties and field pattern of the acoustic wave.

Acoustic radiation force is generated when momentum of the acoustic wave is transferred to the propagation medium via attenuation and scattering interactions. We study low-attenuation gels to which a strongly scattering sphere is embedded. Scattering from the sphere efficiently couples the acoustic field to the gel to induce forces that measurably deform gels at relatively

low acoustic intensity. Without added scatterers, the attenuation coefficient of gelatin gels is small compared with biological tissues (<0.02 dB/mm at 1 MHz for gelatin concentrations less than 10%)[67] and when compared to the scattering coefficient from a steel sphere cast into a gelatin gel.

For sphere diameters small compared with the beam width (1.5 mm and 6 mm, respectively), we can assume local plane waves and the time-averaged force on the scattering sphere is approximately [35]

$$F = \pi a^2 Y \bar{E} \ . \tag{3.1}$$

The quantity a is the sphere radius and Y is the radiation force function as determined by the mechanical properties and geometry of the sphere and the surrounding gel. $\bar{E}$ is the average energy density of the incident field. The time average is over several cycles of the carrier frequency (microseconds) but typically varies over the period of the amplitude modulation (milliseconds). We measured the acoustic radiation force on a steel sphere suspended in water and found it agreed with the prediction of Eq. 3.1 within experimental error [51].

3.2.2 Source Transducer

Figure 3.1 illustrates the experiment depicting a gel sample containing a stainless steel sphere. Force is applied by the acoustic field of a circular, 19-mm-diameter, f/4, PZT element that is transmitting sine-wave bursts at the resonant frequency of 1 MHz. Bursts 200 ms in duration were transmitted every 2 s to induce a maximum sphere displacement >20 μm for gels containing 3% w/w gelatin. The pressure field from the source transducer was measured in water using a recently calibrated PVDF membrane hydrophone (GEC-Research Ltd., Marconi Research Center, Chelmsford, UK). The results were used to estimate a primary radiation force at 60 μN [51]. The error on the force estimate was approximately 16% of the mean value, and was determined primarily by the uncertainty in pressure estimates. The sphere was positioned on the beam axis at the 76-mm radius of curvature of the source. The location of the sphere was tracked in time by measuring and integrating the instantaneous sphere velocity.

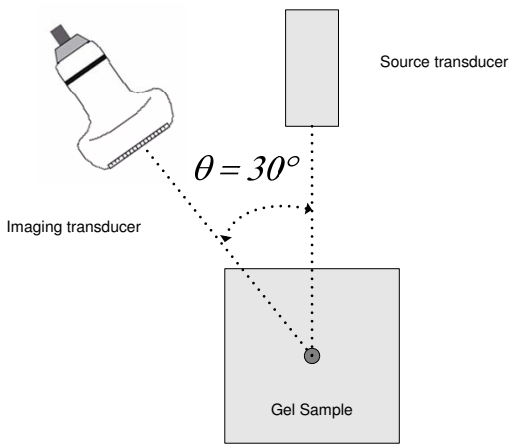

Figure 3.1: Diagram of the experiment to measure viscoelastic properties of gel samples. Acoustic force applied by a source transducer displaces a sphere embedded in the gel. An imaging transducer tracks the induced motion of the sphere.

3.2.3 Sphere Velocity and Displacement Estimation

A Siemens Sono-line Antares system was used to estimate sphere velocity via pulsed Doppler methods. A VF5-10 linear array transducer was driven by 1 cycle, 7.27 MHz voltage pulses to transmit nominally 2.5 cycle, 7 MHz acoustic pulses. Doppler pulse transmission was repeated for a fixed beam-axis position on the time interval $T_s = 76.8$ μs. RF echo waveforms were sampled at 40 Msamples/s using the Ultrasound Research Interface (URI) of the Antares system [68] and stored for offline processing. The axes of the source transducer and linear array intersected at the 1.5-mm-diameter steel sphere, and the beam axes were separated by $\theta = 30°$ as illustrated in Fig. 3.1.

The demodulated complex envelope $V[n, m']$ was computed for each Doppler echo waveform. The sample index $1 \leq n \leq N$ counts echo samples within an echo waveform in what is commonly referred to as "fast time." The index $1 \leq m' \leq M'$ counts the waveforms in "slow time."

We compute the lag-one correlation function estimate between adjacent pairs of echo waveforms using

$$\hat{\phi}[n, m] = V^*[n, 2m-1]\, V[n, 2m] \;, \quad m' = 2m - 1 \;. \tag{3.2}$$

The change of index from m' to m ($1 \leq m \leq M$) avoids counting by 2. The estimate of instantaneous sphere velocity $\hat{v}_s$ from complex correlation estimates is [56, 57]

$$\hat{v}_s[m] = \left(\frac{-c}{4\pi f_c T_s \cos\theta} \right) \frac{1}{N_0} \sum_{n=n_0}^{n_0+N_0-1} \arg(\hat{\phi}[n,m]) \ , \tag{3.3}$$

where c is the compressional-wave speed of sound in the gel medium (1.5 mm/μs), n_0 marks the first fast-time sample in the region of interest near the sphere-echo peak, N_0 is the number of fast time samples in the region of interest, and $\arg(\cdot)$ indicates the phase angle obtained from the arctangent of the ratio of imaginary to real parts of the argument. High-pass filtering in slow time, which is frequently used in blood flow measurements (wall filter), was unnecessary because scattering from the gel was negligible compared to the sphere.

Finally, sphere displacement is estimated by integrating velocity estimates, $\hat{x}(t) \equiv \int_0^t \hat{v}_s(t')dt'$, where $t' = 2mT_s$. Integration was performed numerically using a cumulative trapezoidal scheme [69].

3.2.4 Hydrogel sample construction

Gelatin gel samples (250 bloom strength, Type B, Rousselot, Buenos Aires, Argentina) were constructed to test acoustic radiation force measurements of shear modulus and viscosity. Gelatin powder and distilled water are heated in a water bath at a temperature of $65 - 68$ °C for one hour and periodically stirred. When the sample is cooled to 50 °C, 0.1% by weight formaldehyde is added and thoroughly mixed. Molten gelatin is poured into a cylindrical sample mold (diameter 7.5 cm, height 5.5 cm). Two or three stainless steel spheres 1.5 mm in diameter are widely dispersed within the cooling gel just prior to gelation. Samples with 3% or 4% w/w gelatin concentrations are homogeneous except for the isolated spheres that are separated by at least 1.5 cm.

Narrowband through-transmission measurements of compression-wave speed and attenuation coefficient [67] were made on samples without steel spheres and with 4% gelatin concentration. Measurements made at 21 °C in degassed water were first calibrated using a castor oil sample. Two phantoms were

measured every 0.5 MHz between 7 and 12 MHz. The slope of the attenuation coefficient as a function of frequency was estimated to be 0.027 $\pm$ 0.003 dB mm^{-1} MHz^{-1}. Using no alcohol in the sample, the average speed of compressional waves was $c = 1506 \pm 0.34$ m s^{-1} over the frequency range of the measurement.

The material properties of the gelatin gels were verified independently through oscillatory rheometer experiments. Parallel plate shear experiments were conducted on an AR-G2 rheometer (TA Instruments, New Castle, USA). Circular specimens, 25 mm in diameter and 2-4 mm high, were molded from the same gelatin used to make the large samples containing spheres. After 1 day of gelation, the specimens were removed from the molds and bonded to parallel plate fixtures using cyanoacrylate (Rawn America, Spooner, WI, USA). Five percent strain was applied over a frequency range from 0.1 Hz to 10 Hz with 10 sample points per decade of frequency. For both concentrations of gelatin, the measured storage modulus was averaged over the test range giving 321$\pm$14 Pa and 640$\pm$17 Pa for 3% and 4% gelatin concentrations.

3.2.5 Modeling

The rheological behavior of hydrogels on a scale larger than the ultrasonic wavelength may be described as that of a continuum [65]. We propose to model the displacement $x(t)$ of a sphere embedded in gelatin as a simple harmonic oscillator,

$$M_t \frac{d^2x(t)}{dt^2} + R\frac{dx(t)}{dt} + kx(t) = F(t) \ . \tag{3.4}$$

$F(t)$ is the driving force, M_t is the total mass on which the force acts, R is a damping constant related to the mechanical impedance of the gel (see Appendix A), and k is an elastic constant. Because the uniaxial load is applied along the source transducer beam axis and movement of the sphere is in the same direction, x and F are the axial components of the corresponding vectors. For a step change in force over time from a constant value to zero, $F(t) = F_0(1 - \text{step}(t))$, the homogeneous solution for displacement obtained

from Eq. 3.4 has the form

$$x(t) = \begin{cases} x_0 & t \leq 0 \\ Ae^{-\alpha t}\cos(\omega_d t + \varphi) & t > 0 \end{cases} . \tag{3.5}$$

A is the displacement amplitude, $\alpha = R/2M_t$, $\omega_d = \sqrt{\omega_0^2 - \alpha^2}$ is the resonant frequency with damping, and $\omega_0 = \sqrt{k/M_t}$ is the resonant frequency without damping. From the initial conditions, $A = x_0/\cos\varphi$ and $\tan\varphi = -\alpha/\omega_d$.

It is important to include the surrounding gel in estimating the dynamic inertia of the system [70]. The total mass that reacts to the radiation force is $M_t = M_s + M_a$, where M_s is the mass of the sphere and $M_a = \frac{2}{3}\pi a^3 \rho_g$ is the added mass of surrounding gel, where a is the sphere radius and ρ_g is the density of the gel. The next step is to relate the constants k and R to rheological parameters μ and η.

The viscous drag force F_d experienced by a 1.5-mm sphere as it moves through incompressible and viscous gel at velocities <10 mm/s has a Reynolds number on the order of 0.02. Consequently Eq. 3.4 gives the linear approximation $F_d(t) = -R\,\upsilon_s(t)$, and the classic Stokes equation for R is [71]

$$R = 6\pi a\eta \ , \tag{3.6}$$

where the parameter η has the SI units Pa·s. In the Appendix A, we show that R is the mechanical resistance or the real part of the impedance. This implies that η may be interpreted as the shear damping parameter, which within the frequency range of the experiments is defined as $\mu_2 + \mu_1 a/c_s$, where μ_2 is shear viscosity or the imaginary part of the complex shear modulus μ', μ_1 is the real part of the complex shear modulus μ' and c_s is the shear wave velocity.

Ilinskii et al. [37] applied an analysis parallel to Stokes' derivation to show that the elastic constant in the restoring force equation, $F_r(t) = -kx(t)$, is

$$k = 6\pi a\mu \ , \tag{3.7}$$

where μ, with the SI units Pa, approximates the shear elasticity, μ_1 (see Appendix A).

Combining Eqs. 3.5-3.7, sphere displacement is modeled in terms of shear elasticity and shear damping parameter. The approach is to measure M_t and

a independently and then numerically fit normalized displacement estimates $\hat{x}'(t) = \hat{x}(t)/\hat{x}_0$ to model values $x'(t) = x(t)/x_0$ obtained from Eqs. 3.5-3.7 with μ and η as free parameters. Normalization scales and shifts the response so that displacements have values between 0 and 1. Thus μ and η are estimated without knowledge of the applied force magnitude F_0.

3.3 Results

We verified the proposed model and assumptions by conducting radiation force experiments. The 1 MHz source transducer transmitted 200 ms voltage bursts with the same amplitude in each experiment. Originally at rest, the sphere was suddenly displaced away from the transducer by the pulse a maximum distance x_0 (see Fig. 3.2) before being released to return to its original location. The imaging probe measuring the sphere velocity was transmitting and receiving Doppler pulses during the entire process.

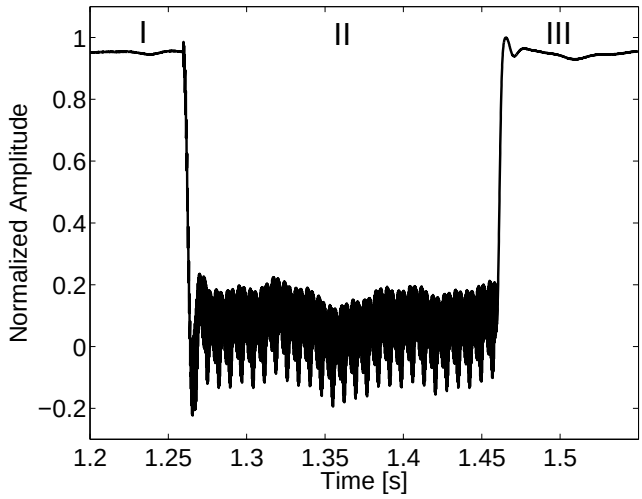

Figure 3.2: Measurement of sphere displacement versus slow time as determined from the change in Doppler echo phase. The sphere is embedded in a 3% gelatin gel. Region I is a time period before radiation force is applied and the sphere is at rest. Region II is a time period during which the source transducer is transmitting a 1 MHz CW burst and the sphere is displaced away from the source. Oscillations indicate cross-talk between the source and Doppler probes. Region III is the time period after the source is turned off and the sphere returns to its original position.

The RF echo waveform in Fig. 3.3 shows that each Doppler pulse causes

the steel sphere to ring. Because the echo signal-to-noise ratio for tracking sphere velocity was very high, Doppler pulse durations were set to 2.5 cycles to temporally resolve the first echo from subsequent ringing echoes. Echo phase is estimated near the peak of the first echo in Fig. 3.3.

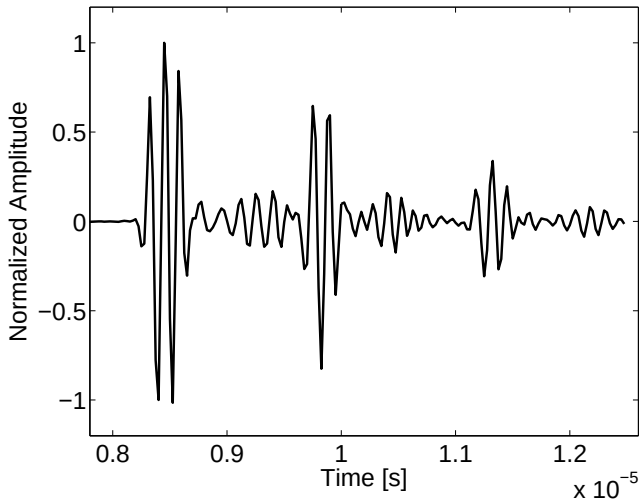

Figure 3.3: Example of a broadband Doppler echo waveform versus fast-time. A single transmitted pulse is reflected from a steel sphere in 3% gelatin gel. Multiple echoes indicate ringing of the sphere.

From the data of Fig. 3.2, we can illustrate the process for a specific experiment. The spectral Doppler acquisition was initiated (Region I). After approximately 1.26 s, the source transducer was turned on for 200 ms (Region II). The phase of the Doppler echo from the sphere changed as the sphere was displaced by the acoustic force. On the time axis of the figure at 1.46 s, the source transducer is turned off (this time is set to $t = 0$ in Eq. 3.5) and the sphere returns to the equilibrium position with the response of a slightly underdamped oscillator. We analyzed sphere displacement data as the source pulse was turned off rather than turned on to avoid cross-talk between the source and Doppler probes as seen in Fig. 3.2, region II.

Figure 3.4 is an example of a comparison between a measured displacement time series $\hat{x}'[m]$ and samples from the best-fit model $x'[m]$ as a function of slow time, $2mT_s$. For an M-point displacement time series with normally distributed random error, the material parameters μ and η are chosen to

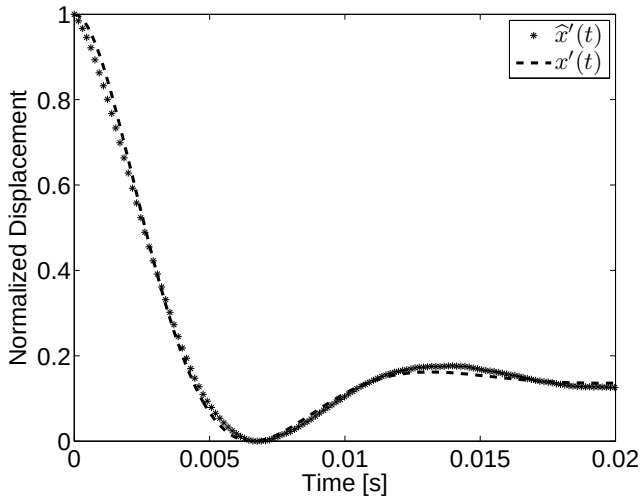

Figure 3.4: Normalized sphere displacement measurements $\hat{x}'(t)$ from region III in Fig. 3.2 are compared with the model equation $x'(t)$ from Eq. 3.5. The minimum least-squares fit ($r^2 = 0.996$) was obtained for 3% gelatin gel aged one day to find $\mu = 317$ Pa and $\eta = 0.57$ Pa s.

give the smallest residual sum of squares [72],

$$r^2 = 1 - \frac{\sum_{m=1}^{M}(\hat{x}'[m] - x'[m])^2}{\sum_{m=1}^{M}(\hat{x}'[m] - \overline{x}')^2} \ , \quad \bar{x}' = \frac{1}{M}\sum_{m=1}^{M}\hat{x}'[m] \ , \tag{3.8}$$

where r^2 is bounded from above by 1 (perfect agreement between data and model) and from below by zero, although it can be negative.

For small displacements, there is close agreement between measurements and the model suggesting that gel deformation is linear as required by Eq. 3.5. Furthermore, if the normalized displacement is time invariant, then we may express the model as a linear system

$$x(t) = \int_{-\infty}^{\infty} dt \; h(t - t') \; (1 - \mathrm{step}(t'))$$

with impulse response

$$h(t) = -\frac{dx}{dt} = Ae^{-\alpha t}\left(\alpha\cos(\omega_d t + \varphi) + \omega_d \sin(\omega_d t + \varphi)\right). \tag{3.9}$$

Equation 3.9 enables prediction of the displacement for any time-varying applied load for which the gel responds linearly.

Measurements of μ and η for 3% and 4% gelatin gels conducted over four days are presented in Fig. 3.5 and Fig. 3.6, respectively. Without adding a strong chemical cross linker, gelatin gels slowly increase their cross-link density, and thus gels continue to stiffen over days. Although gelatin gel responses are not strictly time invariant, the change in the impulse response is negligible over the duration of any experiment. Estimated values of the modulus and shear damping for gels with $C = 4\%$ gelatin concentration are larger than that at 3% for each day of the study. Gilsenan and Ross-Murphy [73] found that the shear modulus varies with the square of gelatin concentration, $\mu \propto C^2$, by 1-5%. Our data in Fig. 3.5 gives a concentration dependence of $C^{2.7}$ on day 1 and $C^{2.4}$ on day 3. Similarly, Fig. 3.6 shows that the shear viscosity coefficient increases linearly with gelatin concentration on day 1 and as $C^{1.3}$ on day 3, which are similar to the Gilsenan and Ross-Murphy result of $\eta \propto C^{1.1}$. Our viscosity measurements are considerably smaller than theirs commensurate with our higher load-frequency bandwidth. Our measurements are comparable to those reported by others using similar acoustic radiation force techniques [74, 26].

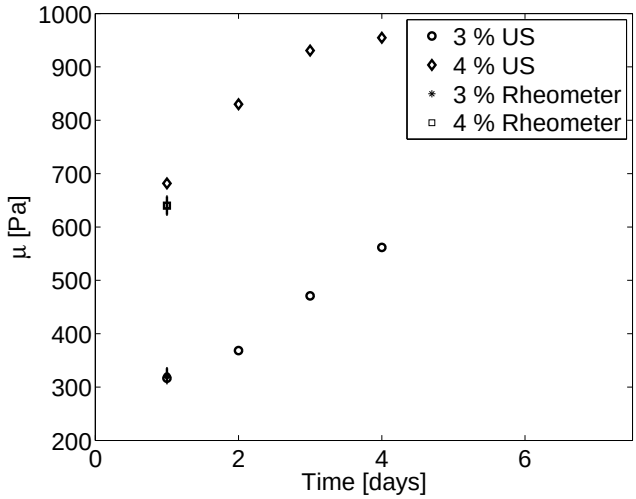

Figure 3.5: Shear modulus as a function of gel age for 3% and 4% gelatin concentrations. Rheometer estimates of μ made on day 1 are also shown with error bars indicating ± 1 sd.

As indicated in Fig. 3.5, rheometer measurements of the shear storage modulus were also made on day 1 for both gelatin concentrations. Five rheometer measurements were made on five different 3% gelatin samples to

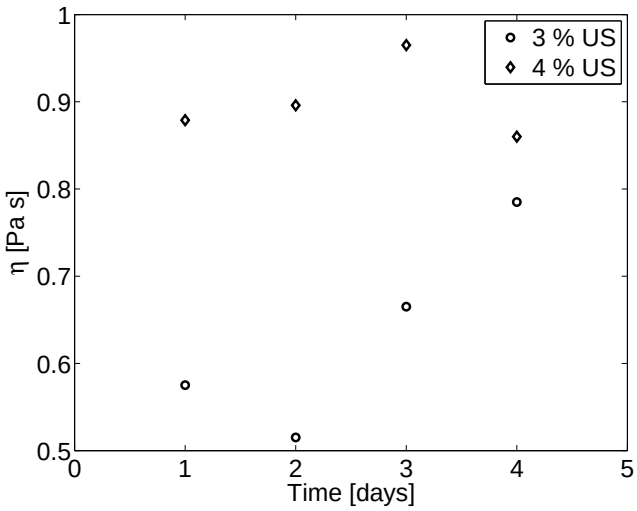

Figure 3.6: Shear damping parameter as a function of gel age for 3% and 4% gelatin concentrations.

yield a mean and standard deviation of $\mu_r = 321 \pm 14$ Pa. The comparable radiation force estimate was 317 Pa. Three measurements were made on three different 4% samples to find $\mu_r = 640 \pm 17$ Pa. The comparable radiation force estimate is 681 Pa. Considering the rheometer measurements as a standard, radiation force estimates of shear modulus are accurate well within the observed day-to-day change in mean values. We were unable to obtain independent estimates of shear viscosity for the gels.

Radiation force measurements may also be used to estimate the shear speed c_s and shear viscosity μ_2; both are defined in the Appendix. At the end of the Appendix, we show that $\mu_1 \simeq \mu$, $\mu_2 = \eta - \mu_1 a/c_s$, and at low force frequencies where $\omega^2\mu_2^2 \ll \mu_1^2$ we obtain the elastic result, $c_s \simeq \sqrt{\mu_1/\rho}$. Applying the 3% gelatin sample results at 24 hours following gelation, $\mu = 317$ Pa and $\eta = 0.57$ Pa·s, we estimate $c_s = 0.56$ m s^{-1} and $\mu_2 = 0.14$ Pa·s. Our estimates are comparable to those reported by others using similar acoustic radiation force techniques [26, 38].

Intra-sample precision variability was estimated by measuring μ multiple times for a single sphere in one gelatin sample. The percent standard deviation was found to be approximately 3.5% of the mean; for example, $\mu = 317 \pm 11$ Pa. Boundary variability, i.e., proximity of each steel sphere to the gel sample surfaces, was examined by averaging μ measurements for different spheres placed in one gelatin sample. That standard deviation was

approximately 7% of the mean. Inter-sample variability for μ was larger, 20% of the mean, primarily because of differences in gel preparation. The relatively small random experimental error is a consequence of the high echo signal-to-noise ratio.

3.4 Discussion

Mechanical parameter values are primary factors determining the ultrasonic sampling rate for pulsed-Doppler velocity estimation. Discussion near Eqs. 3.5 - 3.7 explains that the time-varying displacement amplitude, the frequency, and the phase are functions of μ and η. Estimation accuracy and precision will vary with the sampling rate depending on the bandwidth of the displacement spectrum. For linear gels, the displacement spectrum is the spectrum of the applied force filtered by the mechanical system response of the gel, $H(\omega;\mu,\eta)$. $H(\omega;\mu,\eta)$ is the temporal Fourier transform of Eq. 3.9 parameterized by the material properties.

The model spectrum of interest is the squared magnitude of the temporal Fourier transform of $x'(t)$ from Eq. 3.5. It has the Lorentz form,

$$|X'(\omega)|^2 = \frac{1}{\alpha^2 + (\omega - \omega_d)^2} \ .$$

The 3 dB, 6 dB, and 20 dB bandwidths of the displacement spectrum are, respectively, $\Delta\omega = R/M_t$, $\sqrt{3}R/M_t$, and $\sqrt{99}R/M_t$. Therefore the upper limit on angular frequency is

$$\omega_{max} \quad = \quad \omega_d + \Delta\omega/2 \quad = \quad \sqrt{\omega_0^2 - \alpha^2} + B\alpha \ , \tag{3.10}$$

where $B = 1$, $\sqrt{3}$, or $\sqrt{99}$ for the 3 dB, 6 dB, or 20 dB bandwidths.

To illustrate, Fig. 3.7 displays the displacement spectrum corresponding to the parameters for measurements on day 1 for 3% gelatin-concentration samples. The highest frequency in the 3 dB bandwidth is found from Eq. 3.10 to be $f_{max} = \omega_{max}/2\pi = 120$ Hz. The highest frequencies in the 6 dB and 20 dB bandwidths are 152 Hz and 510 Hz, respectively.

The sampling theorem for bandlimited signals states that minimum sampling rate needed to avoid aliasing is twice the value of the the maximum

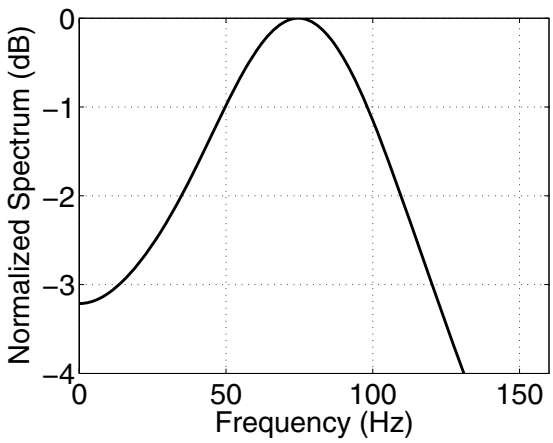

Figure 3.7: Power spectrum of displacement for model parameters from 3% gelatin 24 hours after gelation: $\mu = 317$ Pa and $\eta = 0.57$ Pa·s. Characteristic parameters are the natural frequency $w_d/2\pi = 76.1$ Hz, half bandwidth $\Delta w/4\pi$ =44 Hz, and maximum frequency at the 3 dB limit $f_{max} = 120.1$ Hz.

frequency in the bandwidth. However, we must further increase the rate by the number of pulses in the velocity estimator ensemble, M_e. That is,

$$\begin{aligned} f_s &\geq 2M_e f_{max} = \frac{M_e}{\pi}\left(\sqrt{\omega_0^2 - \alpha^2} + B\alpha\right) \\ &= \frac{M_e}{\pi}\left(\sqrt{\frac{6\pi a\mu}{M_t} - \left(\frac{3\pi a\eta}{M_t}\right)^2} + \frac{3\pi B a\eta}{M_t}\right). \end{aligned} \tag{3.11}$$

For the experiments described in the previous paragraph, where we adopt the 6 dB bandwidth limit and $M_e = 2$, the pulse-repetition frequency (PRF $= f_s$) must exceed 608 Hz to avoid aliasing.

To decide on an acceptable lower bound on the sampling frequency, we over-sampled the Doppler measurements at $f_s = 13$ kHz. We then incrementally downsampled this waveform sequence, being careful to apply the appropriate low-pass anti-aliasing filter as the Nyquist frequency changed, before processing. We thus obtained μ and η estimates as a function of f_s. We observed that a 15 dB bandwidth ($B = \sqrt{31}$) was sufficient to eliminate estimation errors within the intra-sample random error range of 7%. If the echo signal-to-noise ratio was reduced, for example, in stiff gels where sphere displacement is small or for low-scattering spheres, M_e could be increased to

compensate as given by Eq. 3.11. There is also a tradeoff between time resolution for velocity estimates and distance to the target, in our case the sphere depth. Increasing f_s reduces the depth for the maximum unambiguous range to $c/2f_s$ [56].

We have evaluated Eq. 3.11 for a range of μ and η values estimated for gels and for the typical experimental parameters $M_e = 2$, $M_t = 14.7$ mg and $B = \sqrt{31}$ (15 dB bandwidth). The corresponding minimum Doppler-pulse sampling rates are plotted in Fig. 3.8. It is important to point out that Eq. 3.11 is valid only for the Lorentz spectrum characteristic of the Kelvin-Voigt model, with total mass M_t as defined above. Changing the model to, for example, a three-element Zener model [75], would require a new analysis to establish the minimum sampling frequency.

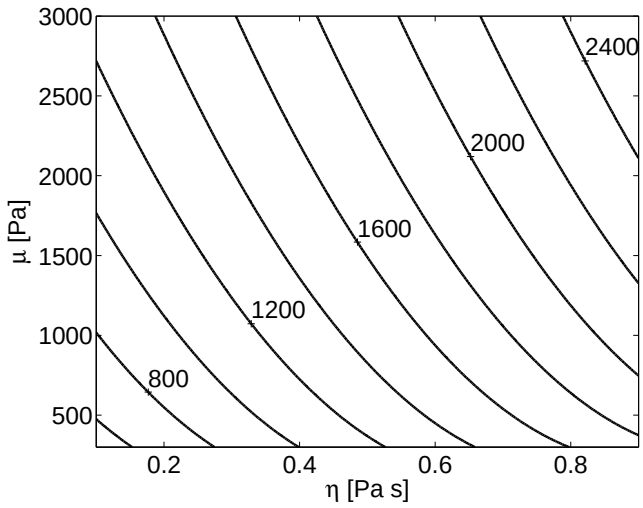

Figure 3.8: Contour plot of the minimum sample frequency (i.e., pulse repetition frequency) in Hz from Eq. 3.11 as required to estimate μ and η as a function of these same material properties. We used a fixed ensemble size $M_e = 2$, $B = \sqrt{31}$ (15 dB bandwidth), and $M_t = 14.7$ mg. For example, for $\mu = 1.5$ kPa and $\eta = 0.5$ Pa s, $f_s \geq 1.6$ kHz.

Quick estimates of μ and η may be made for a well-calibrated experimental system. If M_t and a are known, then η can be found directly from the 3dB bandwidth of the step response, $\eta = M_t \Delta\omega_{3\ dB}/6\pi a$. Applying this result and an estimate of the spectral peak to the expression for resonant frequency ω_d, we can estimate μ.

3.5 Conclusion

In this chapter a technique was developed as a natural extension of our previous work on the calibration of the acoustic radiation force. The presented method uses a damped harmonic oscillator model to accurately predict the movement of a hard sphere embedded in a congealed hydrogel to a sudden change in acoustic radiation force. This result suggests that the gel responds linearly to the force. A contribution of this work is how to relate parameters of the harmonic oscillator to the mechanical impedance of the system and material parameters as derived in Appendix A. The coefficients of the complex shear modulus (shear elasticity and shear dynamic viscosity) are estimated with 7% intra-sample random experimental error by interpreting model parameters in terms of rheological elements. The radiation force estimates of modulus at two gel concentrations closely agree with independent measurements of the gels using a rheometer. This simple but accurate technique is designed to measure viscoelastic properties of 3-D cell cultures remotely to maintain sterile conditions.

There are several disadvantages of the proposed approach. Complex shear modulus can be estimated only at one point where the estimated value depends on the volume averaged material properties around the spherical scatterer. Although the procedure is experimentally fairly simple for the proposed testing of the gelatin phantoms, translation to 3D cell cultures due to the technical problems of embedding spherical scatterers could be challenging. Moreover, application of the technique for *in vitro* or *in vivo* becomes even more challenging. In order to mitigate some of these drawbacks of the proposed method and to move toward the technique that could eventually spatially map the complex shear modulus we decided to analyze propagated shear waves through the medium. From Appendix A it follows that during the sphere displacement part of the system energy is lost on wave propagation, both shear and compressional, where latter was neglected for the given bandwidth. In the next chapter we focus on the propagation of the shear waves in the isotropic homogeneous media and the techniques for the wave excitation.

Gelatin phantoms are weakly viscous. Most of the energy loss of the second order system stems from the radiation of the viscoelastic shear waves. In order to accurately model displacement of the sphere, dynamic viscosity had

to be included. In the next chapter effects of the viscosity will be more apparent as it governs shear wave propagation via complex shear modulus.

CHAPTER 4

SHEAR MODULUS ESTIMATION WITH VIBRATING NEEDLE STIMULATION

4.1 Introduction

During the last decade, several shear-wave estimation techniques have emerged as tools for measuring shear modulus of biological tissues [48, 76, 26, 77]. These dynamic techniques apply an acoustic radiation force or contact vibrator to generate shear waves in the medium that are imaged by phase-sensitive medical imaging methods, e.g., ultrasonic, MR, or optical. In this chapter we describe an ultrasonic Doppler technique that maps shear wave energy generated by a vibrating needle at frequencies between 50 and 450 Hz to estimate the complex shear modulus. It builds on a growing shear-wave imaging literature for estimating the regional elastic modulus [78, 34].

The approach in this chapter is to use a mechanical actuator to harmonically drive a stainless steel needle placed in the medium to generate narrow-band cylindrical shear waves. Shear waves are imaged in a radial plane using a multi-lag phase estimator, which leverages the narrow-band wave feature to extend standard pulse-pair (lag-one) processing for reduced velocity variance. A multi-lag phase estimator is adapted from weather radar literature. Performance of the multi-lag phase estimator is evaluated experimentally and through simulation. We use a phase-gradient technique to estimate shear wave speed from estimated particle velocities at each frequency, and we fit those results to rheological model predictions relating shear wave dispersion to the complex modulus of the medium. Thus we obtain spatially-averaged modulus estimates for hydrogel media that can be independently verified to assess accuracy and precision.

The reminder of this chapter is organized as follows. Section 4.2 reviews

This chapter is adapted from M. Orescanin and M. F. Insana, "Shear modulus estimation with vibrating needle stimulation," *IEEE Transactions on Ultrasonics, Ferroelectrics and Frequency Control*, vol. 57, no. 6, pp. 1358-1367, 2010. Used with permission.

the standard approach toward ultrasound Doppler velocity estimation and presents the theoretical framework for the adapted multi-lag estimator. Furthermore, we discuss the cylindrical shear wave model and the rheological models applicable to the given material. Moreover, we develop a spatial phase-gradient estimator for the estimation of the shear wave speed and formulate a least squares approach toward reconstruction of material parameters. In Section 4.3 we compare both numerical and experimental results of assessing the performance of the proposed multi-lag phase estimator. We present results of the material properties estimation for two gelatin concentrations. We discuss the possibility of a more complex model in Section 4.4 and finally summarize our findings in Section 4.5.

4.2 Methods

The aim of the proposed method is to accurately measure the complex shear modulus of soft biological media. These initial studies measure properties of collagenous hydrogels that share key structural and mechanical features of natural and engineered breast tissues [50].

4.2.1 Temporal Phase and Velocity Estimation

The shear wave imaging experiment is depicted in Fig. 4.1. A mechanical actuator (SF-9324, PASCO Scientific, Roseville, CA) was adapted to hold a stainless-steel needle. The needle is 1.5 mm in diameter (17 gauge) and 13 cm long. The actuator is driven by an arbitrary waveform generator transmitting 500 ms pure-tone voltage bursts in the frequency range of 50 Hz to 450 Hz. The voltage amplitude ranged from 5 V to 15 V. The needle vibrates along the z axis, thus generating cylindrical shear waves that propagate radially for several millimeters. Harmonic shear waves are tracked with a linear-array transducer BW-14/60 (SonixRP, Ultrasonix Medical Corporation, Richmond, BC). The axis of the vibrating needle is oriented $\theta = 35 \pm 5$ degrees from the Doppler beam axis.

The ultrasound system was used to estimate particle velocity via pulsed Doppler methods. A linear array transducer driven by 6-cycle, 6.67 MHz voltage pulses generated echo waveforms with a center frequency of $f_c = 6$

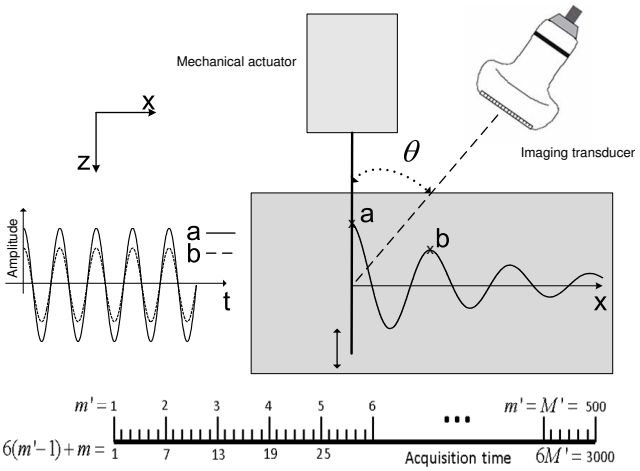

Figure 4.1: Diagram of the experiment to measure viscoelastic properties of gel samples. The mechanical actuator is driving a stainless steel needle. Momentum of the needle displacement is transferred to the medium as cylindrical shear waves. A linear array Doppler probe tracks the induced transverse motion of scatterers as shear waves propagate. At the bottom is a timing diagram for the (up to) 3000 Doppler pulses transmitted at each position along x.

MHz. Doppler pulse transmission was synchronous with actuator excitation. At each lateral position x, up to 3000 Doppler pulses were emitted at a rate of 10 kHz so the total acquisition time was $T_s \leq 300$ ms. The beam-axis position was shifted laterally 0.46 mm, one array element, after each packet transmission, except near the field edges where the beam was electronically steered. The lateral beam increment was verified using a phantom (ATS Laboratories, model 539). 128 A-lines were recorded per RF frame with beam interpolation turned off. RF echo waveforms were sampled at 40 Msamples/s (fast time) and internally downsampled to 20 Msamples/s.

Typical Doppler velocity estimation is based on pulse-pair phase-shift estimation measurements using lag-one autocorrelation [79]. Acquisition time is divided into $M' = 500$ records of 0.6 ms, the temporal-phase sampling interval, where $1 \leq m' \leq M'$. Within each record there is an ensemble of six echoes from $M = 6$ pulse transmissions. The index $1 \leq m \leq M$ counts the echo waveforms in "slow time" sampled on the interval $T_{\text{prf}} = 0.1$ ms within the ensemble. The analytic signal of the echo waveform V and its complex conjugate V^* were entered into the lag-one correlation estimator of temporal

phase,

$$\hat{\phi}[\ell, n, m'] = \frac{1}{M-1} \sum_{m''=M(m'-1)+1}^{M(m'-1)+M-1} V^*[\ell, n, m''] \, V[\ell, n, m''+1] \; . \tag{4.1}$$

The process was repeated for each of $1 \leq n \leq N$ echo range samples in the A-line range and for the $1 \leq \ell \leq L$ A-lines at lateral indices along the x axis of the array. Phase estimates are approximately constant with range, and therefore values are averaged spatially over 10 range samples using a running mean: $\bar{\phi}[\ell, n', m'] = \sum_{n''=n'}^{n'+10} \hat{\phi}[\ell, n'', m']/10$ for $1 \leq n' \leq N - 9$.

From these data, we estimate the instantaneous particle velocity $\hat{v}$ as a function of time and space for each frame of RF data (see Fig 4.2) using [56, 57]

$$\hat{v}[\ell, n', m'] = \left(\frac{-c}{4\pi f_c T_{\text{prf}} \cos\theta} \right) \arg(\bar{\phi}[\ell, n', m']) \quad , \tag{4.2}$$

where c is the compressional-wave speed of sound in the medium (1.5 mm/μs) and $\arg(\bar{\phi})$ indicates the phase angle of spatially-averaged estimates. High-pass "wall" filtering is disabled for these acquisitions. The term $\hat{v}$ estimates the z-axis component of particle velocity where we track the sign of $\arg(\bar{\phi})$ to indicate movement toward or away from the transducer.

Time-harmonic shear wave excitation produces a narrow velocity spectrum, which correlates the echo data within each M-pulse ensemble record. Therefore we may combine multiple phase lags within the ensemble to improve performance.

4.2.2 Lag-k Phase Velocity Estimator

Lag-k estimation of the mean velocity has been investigated by several authors within the weather radar community [57, 80], where it is called poly-pulse-pair processing. This method is able to reduce velocity estimation variance for narrow-band Doppler echoes when the echo signal-to-noise ratio (SNR) is less than 30 dB. The improvement is due to averaging phase estimates whose fluctuations are caused by zero-mean echo-signal noise.

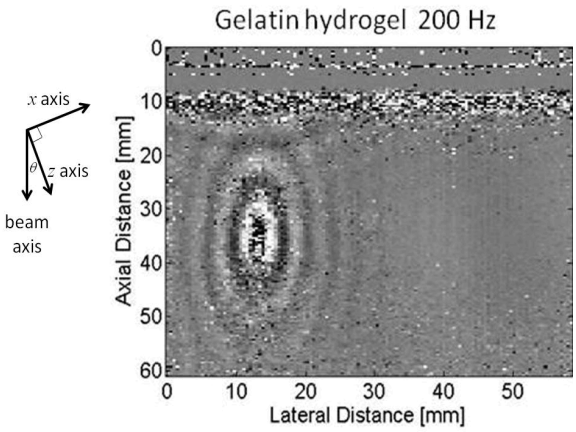

Figure 4.2: Particle velocity image $\hat{v}(x\cos\theta, z\cos\theta)$ in gelatin from one RF frame. Shear waves are generated by a needle moving near the elliptical center. The x, z axes (Fig. 4.1) are rotated $\theta = 30^o$ counterclockwise about the needle.

Lag-k estimation is a generalization of Eq. 4.1,

$$\hat{\phi}[\ell, n, m', k] = \frac{1}{M-k} \sum_{m''=M(m'-1)+1}^{M(m'-1)+M-k} V^*[\ell, n, m''] \, V[\ell, n, m''+k] \ , \tag{4.3}$$

where P correlation estimates are computed within each M-pulse record such that $1 \leq k \leq P < M$. We spatially average estimates along the z-axis and combine the $P = 5$ estimates at a point while eliminating phase-angle ambiguity via

$$\arg(\bar{\phi}[\ell, n', m']) = \frac{1}{10P} \sum_{n''=10(n'-1)+1}^{10(n'-1)+10} \sum_{k=1}^{P} \frac{1}{k} \arg(\hat{\phi}[\ell, n'', m', k]) \ . \tag{4.4}$$

Choosing $P = 1$ reduces Eq. 4.4 to the lag-one autocorrelation estimate. Equation 4.4 estimates may be applied to Eq. 4.2 to find $\hat{v}(t)$ (Fig. 4.1, left plot), and then further processed to estimate the shear-wave phase speed from estimates of spatial phase (Fig. 4.1, right plot and Fig. 4.2) as shown below.

The maximum detectable particle velocity $\hat{v}_{\max}$ is limited by the $\pm\pi$ bound

on temporal phase. For the lag-one estimate of Eq. 4.1, Eq. 4.2 gives $\hat{v}_{\max} = c/4f_cT_{\text{prf}}$. The disadvantage of the lag-k phase estimate of Eq. 4.4 is the k-fold reduction in $\hat{v}_{\max} = c/4f_cT_{\text{prf}}k$.

4.2.3 Rheological Models

Like many soft tissues, gelatin gels can be modeled as linear viscoelastic media. Our goal in this section is to relate observed properties of particle displacement waves to the viscoelastic properties that characterize media in which they travel. Beginning with a solution to the wave equation for elastic solids, we extend the result to include the frequency-dependent complex modulus of viscoelastic media. The results depend on the assumed rheological model describing dynamic behavior of the medium. We then show how temporal phase estimates are applied to the estimation of shear-wave phase speed. The wave speed dependence on applied force frequency, viz., dispersion, is used to estimate the complex modulus.

The Navier wave equation for particle displacement vector $\boldsymbol{u} = (u_x, u_y, u_z)$ [m] in a homogeneous elastic solid is [42],

$$\rho \frac{\partial^2 \boldsymbol{u}}{\partial t^2} = (\lambda + \mu)\nabla\nabla \cdot \boldsymbol{u} + \mu\nabla^2\boldsymbol{u} + \rho\boldsymbol{f} \ , \tag{4.5}$$

where λ and μ are Lamé constants [Pa], ρ is the mass density of the medium [kg/m^3], and $\boldsymbol{f} = (f_x, f_y, f_z)$ is the external body force per unit mass of the medium [m/s^2]. Let $\mathbf{x} = (x, y, z)$ and $r^2 = x^2 + y^2$.

A needle is inserted into gel along the z axis and vibrated harmonically without slipping at radial frequency ω along z with force $\boldsymbol{f} = (0, 0, f_z(\mathbf{x}, t))$ where $f_z(\mathbf{x}, t) = f_0(r)\, e^{-i\omega t}$. That force displaces the needle as $\boldsymbol{u} = (0, 0, u_z(\mathbf{x}, t))$ where $u_z(\mathbf{x}, t) = u_0(r)\, e^{-i\omega t}$. If the needle length and the medium dimensions are both larger than several wavelengths, we can model the experiment as a source radiating into an infinite homogeneous medium. These shear waves diverge cylindrically from the needle along r, and $f_0(r) = C\mu\delta(r)/\pi\rho r$ where C [m] is a dimensionality constant and $\delta(r)/\pi r = \delta(\mathbf{r}) = \delta(x)\delta(y)$ is the 2-D

Dirac delta. Lacking compressional waves, $\nabla \cdot \boldsymbol{u} = 0$, and Eq. 4.5 reduces to

$$\begin{aligned} -\omega^2 u_z(\mathbf{x},t) &= \frac{\mu}{\rho}\nabla_r^2 u_z(\mathbf{x},t) + f_z(\mathbf{x},t) \\ -k_s'^2 u_0(r) &= \nabla_r^2 u_0(r) + C\delta(r)/\pi r \ , \end{aligned} \tag{4.6}$$

where the elastic shear-wave number $k_s' = \sqrt{\rho\omega^2/\mu} = \omega/c_s$ for shear-wave speed $c_s = \sqrt{\mu/\rho}$, and $\nabla_r^2 = \frac{\partial^2}{\partial r^2} + \frac{1}{r}\frac{\partial}{\partial r}$.

We now solve Eq. 4.6 for u_0, the z component of particle displacement within the x, y plane. Leveraging polar symmetry, a solution is found by taking the Hankel transform of Eq. 4.6 and solving for $U_0(\xi) \triangleq \mathcal{H}u_0(r) = C/(\xi^2 - k_s'^2)$. The inverse transform yields the spatial part of displacement [42],

$$\begin{aligned} u_0(r) &= \mathcal{H}^{-1}U_0(\xi) = \frac{i\pi C}{2}H_0^{(1)}(k_s' r) \\ &\simeq \sqrt{\frac{-\pi C^2}{2k_s' r}}e^{i(k_s' r - \pi/4)} \ . \end{aligned} \tag{4.7}$$

The exact solution (first form) includes $H_0^{(1)}$, a zeroth-order Hankel function of the first kind. The approximate solution (second form) includes the asymptotic expansion of $H_0^{(1)}$ for large $k_s' r$ [81]. At 50 Hz, $k_s' r \simeq 3$ at 1 cm from the needle.

Applying the correspondence principle [82, 83], we can extend the above solution for linear *elastic* solids to include linear *viscoelastic* solids. To do this, we represent the dynamics of viscoelastic media with a complex shear modulus from the Kelvin-Voigt (K-V) rheological model, $\mu = \mu_1 - i\omega\eta$, where μ_1 is the elastic shear constant and η is the dynamic viscous constant of the K-V model. The wave number for viscoelastic media is now complex, $k_s = \sqrt{\rho\omega^2/\mu} = k_s' + i\alpha_s$, where α_s is the shear-wave attenuation coefficient. Also, shear speed can vary with frequency for the K-V model [84],

$$c_s(\omega) = \omega/\Re\{k_s\} = \sqrt{\frac{2(\mu_1^2 + \omega^2\eta^2)}{\rho(\mu_1 + \sqrt{\mu_1^2 + \omega^2\eta^2})}}$$

and

$$\alpha_s(\omega) = \Im\{k_s\} = \sqrt{\frac{\rho\omega^2(\sqrt{\mu_1^2 + \omega^2\eta^2} - \mu_1)}{2(\mu_1^2 + \omega^2\eta^2)}} \ . \tag{4.8}$$

Equation 4.8 relates μ_1, η to measurements of shear wave dispersion [48] and attenuation. Our next step is to estimate c_s from the spatial phase of harmonic shear wave propagation.

4.2.4 Shear Speed From Spatial Phase Gradient

The z component of particle velocity is, from Eq. 4.7,

$$\begin{aligned} v(x,t) &= \frac{\partial}{\partial t} u_0(x)\, e^{-i\omega t} = \sqrt{\frac{\pi\omega^2 C^2}{2k_s x}} e^{i(k_s x - \omega t - \frac{\pi}{4})} \\ &= V_0(x) e^{i\gamma(t)} e^{i\psi(x)} \ . \end{aligned} \tag{4.9}$$

Since we measure velocity in the x, z plane (Fig. 4.1), we replace r with x. The last form of the "complex" velocity expression of Eq. 4.9 separates velocity magnitude $V_0(x)$ from the temporal and spatial phase factors. Because k_s is complex, it requires some algebra to show the spatial phase gradient is

$$\frac{d\psi}{dx} = \frac{\omega}{c_s(\omega)} \ . \tag{4.10}$$

Thus c_s is estimated from the spatial phase gradient of particle velocity. In practice, phase is sampled along the x axis at a constant interval equal to the transducer array pitch, $X = 0.46$ mm, such that $x[\ell] = \ell X$.

Let $\hat{v}'$ be the analytic signal of particle velocity estimates from Eq. 4.2. Recall that we compute as many as 500 temporal velocity estimates at each location in the $x[\ell], z[n']$ image plane. Beginning with the left-most A-line in Fig. 4.1, we compute a four-sample running mean in space and average 40 values in time (after the transient wave has dissipated) to form spatiotemporally-averaged estimates,

$$\bar{\psi}[\ell', n'] = \frac{1}{40} \sum_{m'=301}^{340} \frac{1}{3} \sum_{\ell''=\ell'}^{\ell'+3} \hat{v}'^{*}[\ell'', n', m']\, \hat{v}'[\ell''+1, n', m'] \ . \tag{4.11}$$

Phase $\bar{\psi}[\ell', n']$ is a function of space via $x[\ell'], z[n']$.

In Appendix B we show that $d\psi/dx$ from (5.2) is approximately $(\arg \bar{\psi})/X$. Similar to that found by Hoyt et al. [85] for crawling wave imaging, the

average shear speed is

$$\hat{c}_s(\omega) = \frac{\omega X}{\langle \arg(\bar{\psi}[\ell', n']) \rangle_{\Omega(\omega)}} \ , \tag{4.12}$$

where $\langle \cdot \rangle_{\Omega(\omega)}$ indicates that we further spatially average values over area Ω near the vibrating needle where the velocity SNR > 20 dB. Area Ω includes a subset of indices ℓ', n' that becomes smaller with ω because attenuation increases and needle vibration amplitude decreases with frequency. The standard deviation of $c_s(\omega)$ estimates is found using the number of independent samples within $\Omega(\omega)$ as the degrees of freedom. The number of independent samples was estimated from the 2D autocovariance function for $\hat{v}(x, z)$.

Analogous to the maximum detectable particle velocity in Section 4.2.1, we can estimate the minimum detectable shear-wave velocity from the bound on the spatial phase argument: $|\arg(\hat{\psi})| < \pi$. The minimum detectable shear wave velocity from Eq. 4.12 is therefore $\omega X/\pi$.

We close this section by comparing measurements of spatial phase in a gelatin gel with the exact and large-argument approximate predictions in Fig. 4.3. Clearly the approximation is accurate within measurement error even for $k_s' x = 1$.

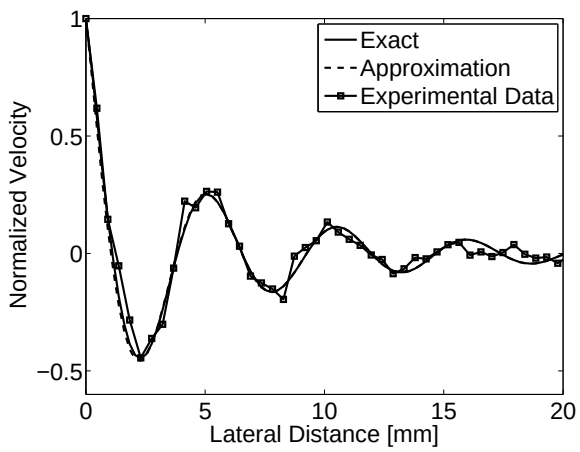

Figure 4.3: Comparisons of the exact (solid line) and approximate (dashed line) solutions to the cylindrical wave equation with measured values for 4% gelatin gel (solid-squares line) at $\omega/2\pi = 150$ Hz. Good agreement between the three justifies the phase gradient approach of Eq (4.12). Note $k_s' x \simeq 1$ at $x = 1$ mm.

4.2.5 Complex Modulus From Shear Wave Dispersion

Viscoelastic parameters μ_1 and η are estimated by comparing modeled and measured data using least-squares fitting techniques: predicted values are obtained from Eq. 4.8 and measured values from Eq. 4.12. Assuming measurement errors are normally distributed $\mathcal{N}(0, \sigma^2)$, the maximum-likelihood principle suggests that estimates $\hat{\mu}_1, \hat{\eta}$ are given by the parameters that minimize the sum of weighted, squared residuals,

$$\min \sum_{j=1}^{J} \left(\frac{\hat{c}_s(\omega_j) - c_s(\omega_j; \mu_1, \eta)}{\sigma_j} \right)^2 . \tag{4.13}$$

There are J frequencies in the bandwidth at 50 Hz intervals. Minimization was performed using a Levenberg-Marquardt method with precalculated analytical gradients [86].

4.2.6 Gelatin Gel Samples

Gelatin samples (250 bloom strength, Type B, Rousselot, Buenos Aires, Argentina) were constructed to test the method. Gelatin powder and distilled water are heated in a water bath at $65 - 68$ °C for one hour and periodically stirred. When the sample is cooled to 50 °C, 0.1% by weight formaldehyde is added and thoroughly mixed. We also mixed in cornstarch particles, 3% by weight, to introduce random acoustic scatterers. Molten gelatin is poured into cylindrical molds (11.3 cm diameter, 7.5 cm height) and allowed to congeal. Homogeneous samples with 4% or 8% w/w gelatin concentrations were tested.

Material properties of the same gelatin gels were tested in a parallel-plate shear rheometer (Model AR-G2, TA Instruments, New Castle, DE) using additional samples. Samples 2.5 cm in diameter and 0.2-0.4 cm high were removed from their molds one day after gelation and bonded to the rheometer plates using cyanoacrylate (Rawn America, Spooner, WI). Five percent shear strain was applied. For each of the 4% and 8% gelatin concentrations, five samples were tested and the measured relaxed shear modulus was averaged giving, respectively, $\mu_1 = 571 \pm 67$ Pa and $\mu_1 = 2286 \pm 315$ Pa. Parameter η cannot be estimated by this method. While shear modulus increased quadratically with gelatin concentration, no change was detected with the

addition of cornstarch particles.

4.3 Results

4.3.1 Phase Estimator Performance

The performance of the lag-k phase estimator ($P = 5$) compared to lag-1 estimator is known to depend on the echo SNR and the correlation between ensemble echoes, i.e., the relative Doppler spectral bandwidth [87, 80]. To help us decide when to apply each estimator, we simulated an ensemble of RF echo signals in one spatial dimension and time so we could measure velocity variances.

Doppler-pulse echo simulations assumed constant particle velocities in the range gate that varied between 0 and 8 cm/s. This range was observed experimentally in gelatin at 100 Hz needle vibration. We modeled scatterers using a white Gaussian random field scanned by a linear time-invariant pulse-echo system with 6-cycle pulses and other parameters given in Section 4.2.1. Zero-mean, additive, white Gaussian noise was added to echoes to adjust the echo SNR.

Estimator performance was quantified from the errors observed using simulated echo data. If $\mathrm{var}(\hat{v}_1)$ and $\mathrm{var}(\hat{v}_k)$ are measured variances for the lag-1 and lag-k particle velocity estimates ($M = 6$ for both), the percent improvement for the lag-k estimator relative to lag-1 is given by the factor

$$\xi = 100 \left(1 - \sqrt{\frac{\mathrm{var}(\hat{v}_k)}{\mathrm{var}(\hat{v}_1)}} \right) , \tag{4.14}$$

which can be positive or negative. The echo simulator was validated by comparing velocity variances measured from simulated data to those predicted [88].

Figure 4.4 shows the improvement as a function of the fractional Doppler bandwidth that is normalized by the maximum detectable velocity $2\hat{v}_{\max}$. This normalized bandwidth is labeled σ_{vn} in Fig. 4.4. At high echo SNR (40 dB), the lag-k estimator provides advantages only for extremely narrow-band Doppler spectra. At 10 dB echo SNR, however, there is a 60% - 70% im-

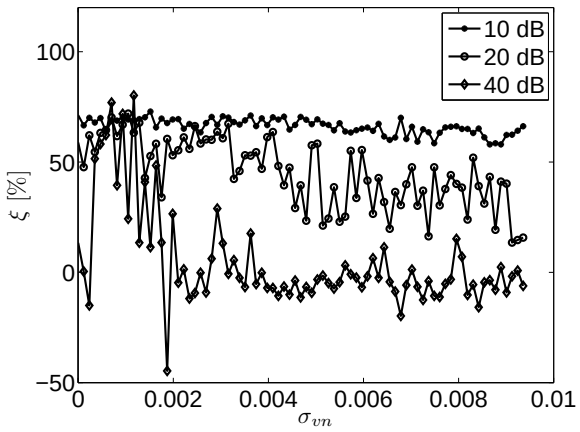

Figure 4.4: Percent improvement ξ is plotted as a function of normalized Doppler spectrum width σ_{vn} for 10, 20 and 40 dB echo SNR ratio. Results are from simulated echo data.

provement at all bandwidths. In the 20-30 dB range of echo SNR, of greatest experimental interest, the advantage is primarily at low bandwidth. Because of long wavelengths, particle velocity in shear-wave imaging is nearly constant within a range gate. Pulse bandwidth, which has the largest effect on Doppler spectral bandwidth, dictates the relative advantage of lag-k estimation over lag-1. We also estimated ξ for experimental data. Shear wave recordings were repeated 19 times for 4% gelatin concentration at 100, 300 and 400 Hz. The improvement factor is plotted in Fig. 4.5 as a function of lateral distance from the needle source. We find that, although the echo SNR is constant with x, the improvement factor ξ increases with x, suggesting the greatest advantage of lag-k estimation is at low particle velocity (low amplitude shear waves). The advantage stems from the reduction in Doppler bandwidth that accompanies lower mean velocity.

4.3.2 Modulus Measurements in Gelatin

Measured shear-wave dispersion curves for 4% and 8% gelatin samples are shown in Fig. 4.6. For both concentrations, measurements of three gel samples are shown along with best-fit dispersion model curves from Eq. 4.8. Values for μ_1 and η obtained by minimizing Eq. 7.7 are listed in Table 4.1 along with mean values ± sd and rheometer estimates of μ_1. Correlation co-

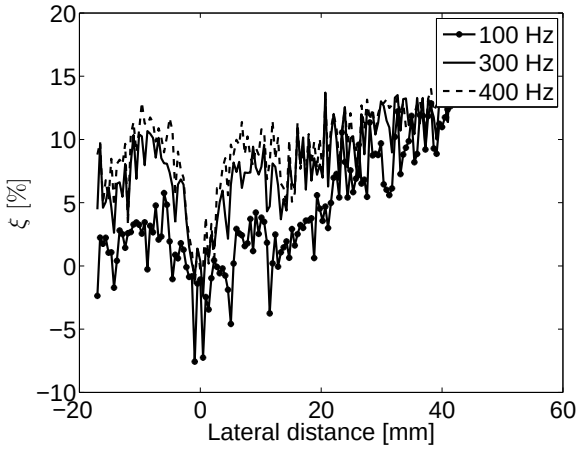

Figure 4.5: Percent improvement ξ is plotted as a function of lateral distance from the source for 100, 300 and 400 Hz shear wave frequencies. Results are measured from gelatin gels.

Table 4.1: Viscoelastic parameter measurements for gelatin gels.

4% Gelatin	μ_1 [Pa]	η [Pa s]	r^2
Sample1	469	0.18	0.87
Sample2	564	0.17	0.83
Sample3	680	0.27	0.85
Average	571 ± 105	0.21 ± 0.06	
Rheometer	571 ± 67		
8% Gelatin	μ_1 [Pa]	η [Pa s]	r^2
Sample1	3323	0.47	0.1
Sample2	3173	1.34	0.8
Sample2	2708	0.7	0.5
Average	3068 ± 321	0.84 ± 0.45	
Rheometer	2286 ± 315		

efficients of the fit, r^2, were computed using the method of Cameron [72] as adapted for our application [19]. The actuator voltage amplitude was 15 V. Three dispersion measurements and corresponding best-fit model curves are displayed for one 4%-concentration gelatin sample in Fig. 4.7. Measurements were acquired for 5, 10, and 15 V mechanical actuator voltage amplitudes that provided three different particle displacements at the needle surface.

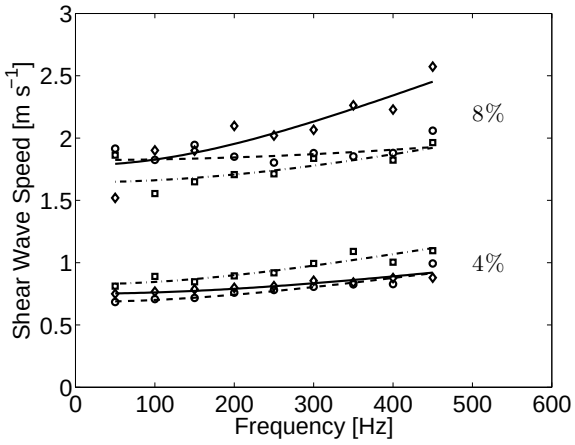

Figure 4.6: Measurements of shear wave dispersion in six samples, three each with 4% and 8% gelatin concentration. Lines are best-fit dispersion models used to estimate the complex moduli listed in Table 4.1. For both concentrations, measurements from sample 1 are indicated by a circle, sample 2 by a diamond, and sample 3 by a square.

Particle displacement amplitudes at 50 Hz estimated in gel regions immediately adjacent to the needle gave peak measured displacement amplitudes of $u_{5\mathrm{V}} = 86$ μm, $u_{10\mathrm{V}} = 185$ μm and $u_{15\mathrm{V}} = 255$ μm. Particle displacement amplitudes at 450 Hz were found to be much smaller $u_{5\mathrm{V}} = 0.3$ μm, $u_{10\mathrm{V}} = 0.7$ μm and $u_{15\mathrm{V}} = 1$ μm. From these data, we estimated μ_1 at 5, 10, and 15 V to be, respectively, 476, 482, and 469 Pa. We also estimated η and found values of, respectively, 0.21, 0.21, and 0.18 Pa·s. Close agreement among estimates at the three applied strains supports the assumption of linearity in gelatin between 50 and 450 Hz.

4.4 Discussion

We compared rheometer measurements to shear-wave estimates of μ_1 in the previous section to validate results. Although the two measurements are based on different rheological models, direct comparisons between some parameters are possible [89]. The Maxwell model is often used in the constitutive equation describing shear rheometry. We found a third-order Maxwell model represents rheometer measurements in gelatin [4] with the time-varying

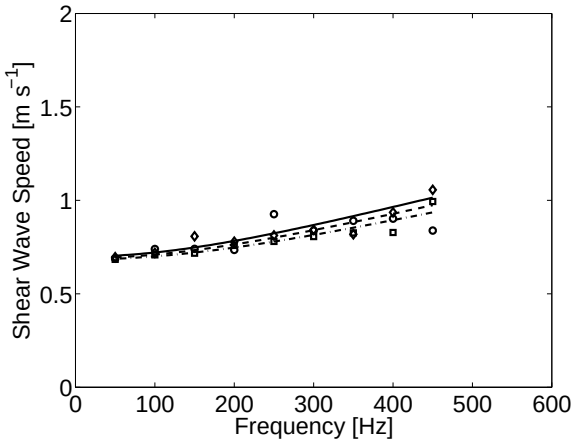

Figure 4.7: Measurements of shear wave dispersion in one 4% gelatin sample for actuator voltages set to 5, 10, and 15 V. Lines are best-fit dispersion models used to estimate the complex modulus. Equivalence of the three responses demonstrates the linear mechanical response of the gelatin gel.

shear modulus

$$G(t) = G_0 + G_1 e^{-t/\tau_1} + G_2 e^{-t/\tau_2} + G_3 e^{-t/\tau_3} \ , \tag{4.15}$$

for constants G_i and τ_i. The *relaxed modulus* of the Maxwell model is G_0, which we obtain at $t \gg \tau_{\max}$ where $G(t \to \infty) \simeq G_0$. Comparing this result with the complex modulus of the K-V model in the frequency domain, $\mu(\omega) = \mu_1 - i\omega\eta$, it can be shown that G_0 from rheometry is comparable to μ_1 from shear wave imaging. These values may be compared in Table 4.1. Unfortunately, no similar relationship exists between η and Maxwell model parameters. We compared measurements in fresh and damaged liver tissues with those reported by other labs using different techniques, and we found general agreement for $c_s(\omega)$ [49]. Inter-lab consistence may help validate viscoelastic measurements in complex-structured tissues.

Rheological models help us parameterize the viscoelastic behavior of materials: the Kelvin-Voigt model describes creep while the Maxwell model describes stress relaxation. Of the two, the Kelvin-Voigt model is thought to be more representative of shear wave propagation through gelatin. However, the Zener model (series connection of an elastic spring and a Kelvin-Voigt unit) is the simplest model that predicts both phenomena in linear viscoelastic polymeric solids [75]. We now summarize its frequency response in the

context of our analysis.

The complex modulus that results from the Zener model is given by [75]

$$\mu^Z(\omega) = \mu_1 \frac{1+\omega^2\tau_\sigma\tau_\epsilon}{1+\omega^2\tau_\sigma^2} - i\omega\mu_1\frac{\tau_\epsilon-\tau_\sigma}{1+\omega^2\tau_\sigma^2}\ , \tag{4.16}$$

where $\mu_1 = \mu^Z(0)$ is the relaxed modulus and τ_σ and $\tau_\epsilon \geq \tau_\sigma$ are time constants.

The complex wave number for the Zener model is $k_s^Z = (\rho\omega^2/\mu_Z)^{1/2} = \omega/c_s^Z + i\alpha_s^Z$, which can be expressed in terms of shear wave speed and attenuation coefficient using

$$\begin{aligned} c_s^{K,Z}(\omega) &= \omega/\Re\{k_s^{K,Z}\} \\ &= \sqrt{\frac{2(\Re\{\mu^{K,Z}\}^2+\Im\{\mu^{K,Z}\}^2)}{\rho(\Re\{\mu^{K,Z}\}+\sqrt{\Re\{\mu^{K,Z}\}^2+\Im\{\mu^{K,Z}\}^2})}} \end{aligned}$$

and

$$\begin{aligned} \alpha_s^{K,Z}(\omega) &= \Im\{k_s^{K,Z}\} \\ &= \sqrt{\frac{\rho\omega^2(\sqrt{\Re\{\mu^{K,Z}\}^2+\Im\{\mu^{K,Z}\}^2}-\Re\{\mu^{K,Z}\})}{2(\Re\{\mu^{K,Z}\}^2+\Im\{\mu^{K,Z}\}^2)}}\ . \end{aligned} \tag{4.17}$$

K, Z indicates that parameters from either the Kelvin-Voigt or Zener models may be applied.

We estimated parameters of the Zener model for the same gelatin sample data described above, and we list them in Table 4.2. These may be compared with results from Table 4.1. The small difference between μ_1 results for the K-V model in the two tables depends on whether data from three samples were first averaged and then fit to a model (Table 4.2) or vice versa (Table 4.1).

Equation 4.17 is fit to the averaged dispersion measurements from 4% and 8% gelatin concentration, and the results are shown in Fig. 4.8. Averaged measurements are also plotted with standard errors indicated. For both models, the shear speed at low frequency is $\sqrt{\mu_1/\rho}$, increasing monotonically with ω. However the Kelvin-Voigt model is unbounded $c_s(\infty) \to \infty$ while the Zener model is bounded by $c_s(\infty) \to \mu_1(\tau_\epsilon/\tau_\sigma)$. In the 50-450 Hz shear-wave bandwidth, the two models agree within measurement uncertainties

Table 4.2: Estimated parameters from Zener and Kelvin-Voigt models are compared with G_0 from rheometry in 4% and 8% gelatin.

Gelatin	μ_1 [Pa]	τ_ϵ [ms]	τ_σ [ms]
Z: 4%	563	0.5	0.2
K-V: 4%	570		
Rheometer: 4%	$G_0 = 571 \pm 67$		
Z: 8%	2836	0.53	0.21
K-V: 8%	2919		
Rheometer: 8%	$G_0 = 2286 \pm 315$		

and therefore each represents measurement in gelatin gels equally. Only at higher frequencies do the two models diverge.

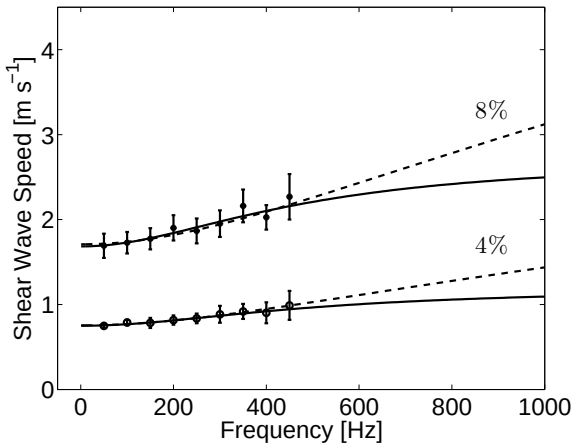

Figure 4.8: Average shear-wave dispersion measured for 4% and 8% gelatin concentrations and best-fit model curves. The dashed lines are for the Kelvin-Voigt model and solid lines are for the Zener model. Error bars indicate one standard error based on measurements from three samples each.

Frequency characteristics of viscous losses have also been quantified using a quality factor $Q(\omega) = -\Re\{k_s^2\}/\Im\{k_s^2\}$ or its inverse Q^{-1} called the dissipation factor [75]. The relaxation peak of the Zener model is located at $f_0 = 1/(2\pi\tau_0)$ where $\tau_0 = \sqrt{\tau_\epsilon \tau_\sigma}$ and represents a peak of viscous losses. For the estimated properties for 4% and 8% gelatin, estimated relaxation peaks are located at $f_0^{4\%} = 503$ Hz and $f_0^{8\%} = 481$ Hz respectively.

4.5 Conclusion

This chapter presents a method for measuring the complex shear modulus of hydrogel samples. Eventual applications of these measurements include the basic-science goal of following changes in the mechano-environment of 3-D cell cultures undergoing malignant cell transformations and tumor development. More detailed knowledge of cellular mechanobiology on the scale of a millimeter is expected to help illuminate the role of elasticity imaging in cancer diagnosis.

Vibrating a thin needle along its long axis generates shear waves. This geometry provided closed form solutions to the shear wave equation that yielded a Green's function describing how wave energy propagates and is dissipated in the surrounding medium. Long needles induce extended and predictable fields of shear waves that yield high velocity signal-to-noise ratios for materials characterization below 450 Hz. Time-harmonic waves, imaged under steady-state conditions, use lag-k estimators of phase, thus improving the reliability of shear-wave dispersion measurements for modulus estimation. This approach lends itself to accurate estimation of the complex shear modulus parameters. Accuracy of the elastic shear modulus estimates was verified through comparisons with the relaxed modulus from parallel-plate rheometry, where agreement was observed.

The current method is based on an inversion of the shear-wave dispersion equation. One limitation of this method is that measurements at several frequencies must be obtained to estimate each complex modulus value. Furthermore, material homogeneity and reflectionless boundaries are assumed within the measurement region, which is a reasonable assumption for our proposed applications. Therefore the phase-gradient method is an acceptable method for measuring a modulus from velocity estimates.

One alternative approach to needle vibration is to apply an amplitude-modulated acoustic radiation force to a sphere placed in the medium [19, 90, 38]. An oscillating sphere produces shear wave energy that also has known closed-form expressions, and thus permits quantitative mechanical analysis of the medium. However the dipole radiation pattern is more complex and more heterogeneous within any Doppler imaging plane. Yet radiation force offers the best opportunity for extending the stimulus force frequency above 500 Hz, where clear distinctions among rheological models become more apparent.

The displacement amplitude of mechanical actuators mechanically loaded by a needle placed in a viscous gel is significantly reduced at higher frequencies either because of the actuator itself or needle slippage. The signal-to-noise ratio for velocity estimates becomes the limiting factor when imaging shear waves above 500 Hz not only because precise force patterns are difficult to generate but also because of wave divergence and absorption at distances greater than a couple millimeters from the source. The overall conclusion is that accurate measurements of the complex shear modulus may be achieved with needle vibration in viscoelastic hydrogels up to 450 Hz.

In order to explore the frequency landscape of material response, a higher-order model, or standard solid body model, was considered that has a frequency dependant elastic shear modulus. Probing the frequency response of the shear modulus could yield valuable insight into viscoelastic mechanisms for different tissues which could lead to potentially valuable clinical information.

The higher-order Zener model was considered for characterizing hydrogel response within the given bandwidth of the measurement. Within the testing bandwidth, hydrogel exhibits strong elastic behavior and differences between the two models are negligible. Therefore, either model is representative of gelatin gels between 4% and 8% concentrations. Increasing the measurement bandwidth above 450 Hz would provide a means to differentiate between the two models. In soft biological tissue with larger viscous response, it would be possible to differentiate between the two models where the Zener model could provide more insight into the complex dynamics of the perfused mammary tissues.

In the next chapter the developed experimental method is used to study complex material properties in fresh and thermally damaged porcine liver. Liver was chosen as the biological phantom for the proposed technique characterization and as a medium to study modeling of the soft tissue mechanics. Moreover, in order to invoke larger contrasts in soft tissue mechanical response, porcine liver was thermally damaged to enhance viscoelastic changes in the material.

CHAPTER 5

DISPERSION AND SHEAR MODULUS MEASUREMENTS OF PORCINE LIVER

5.1 Introduction

Rheological models of organ and tissue material properties are playing significant roles in developing image-guided medical diagnoses and surgical procedures. During the previous two decades, advances in instrumentation and modeling have led to improvements in elasticity imaging and its interpretation for discriminating benign from malignant breast lesions [7, 3], staging liver fibrosis [8, 9], monitoring tumor ablation [91], assessing myocardial function [77, 10], screening for prostate cancer [11], and probing neurodegenerative processes in the human brain [10]. The diagnostic information provided by elasticity imaging originates with the important role of the *microscopic* cellular mechanoenvironment in establishing homeostasis and regulating disease progression [13, 92]. It is thought that these microscopic effects influence the appearance of tissues in elasticity images by modifying *macroscopic* tissue structures. Rheological modeling aims to summarize the material properties of complex-structured media by representing it as a simple mechanical system characterized by just a few parameters. When the mechanical response of the model system closely represents tissue measurements, we assign model parameters to represent tissue properties at the spatiotemporal scale of the measurement. The value of elasticity imaging depends on how well the model parameters represent tissue behavior.

The principal aim of this chapter is to observe how well standard rheological models represent measurements of shear-wave speed in parenchymal tissues. The complex modulus of fresh, ex vivo, porcine liver is estimated because the modulus can be modified by heating the tissue, measurements

This chapter is adapted from M. Orescanin, M. A. Qayyum, K. S. Toohey, and M. F. Insana, "Dispersion and shear modulus measurements of porcine liver," *Ultrasonic Imaging*, accepted for publication. Used with permission.

could be readily verified through literature comparisons, and the results contribute to the accumulating data on assessments of thermal tissue damage induced during ablation procedures. Standard linear-solid two-parameter (Kelvin-Voigt or K-V) and three-parameter (Zener) rheological models [89] are used in this study to model the complex shear modulus.

This chapter follows the presented approach in Chapter 4 where the basic measurement applies pulsed-Doppler techniques to image particle velocities v associated with shear-waves radiating from a harmonically vibrating needle placed in the liver tissue sample [20]. The phase speed of cylindrical shear wave estimates $\hat{c}_s$ is measured from the spatial-phase gradient $\nabla\psi$. Speed estimates are numerically fit to modeled values to find the complex shear modulus, μ [84]. From μ and liver density ρ, the shear attenuation coefficient can be estimated.

5.2 Methods

5.2.1 Tissue Preparation

Six freshly-excised whole porcine livers were obtained in pairs during three different days from the Department of Animal Sciences at the University of Illinois. Mechanical studies were conducted on one fresh and one heated liver sample as illustrated in Fig. 5.1. Each organ appeared to be healthy and free of obvious lesions or other structural anomalies. Livers were placed in iced saline (0.9% sodium chloride) immediately after harvesting and then transported to the lab for measurement. Once in the lab, fresh livers were warmed in normal saline at 23 °C for one hour before mechanical testing.

Thermally damaged livers were prepared by placing a fresh liver in saline heated to 47 °C for 90 minutes. The aim was to thermally denature proteins [93] and modify the collagen cross-linking to alter the viscoelastic properties of the liver. After the heating period, livers were cooled in 23 °C saline for one hour prior to mechanical testing. All liver measurements were made at 23 °C within 8 hours of harvesting.

Following each experiment, a small liver sample was prepared for histological study. Tissues were fixed with formalin, embedded in paraffin for sectioning and stained with hematoxylin and eosin. Slides were examined for

structural changes that might correlate with mechanical measurement observations. No significant histological changes were observed. Examples of fresh and thermal-damaged tissues can be seen in Fig. 5.1.

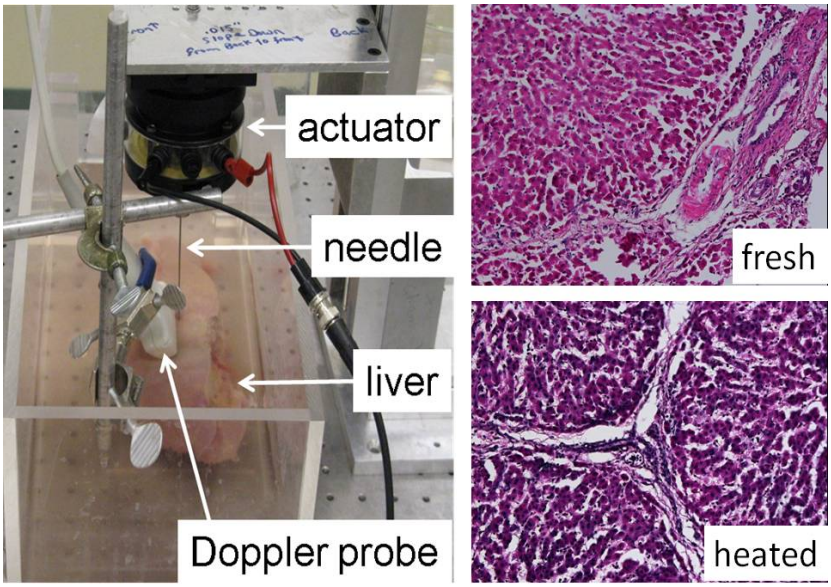

Figure 5.1: (left) Photograph of a shear-wave imaging experiment using fresh porcine liver. (right) Histological sections of fresh and thermally damaged porcine liver samples at 20x magnification.

5.2.2 Shear-Wave Phase Speed Estimation

A 17-gauge stainless-steel needle (13 cm long) was inserted 3-5 cm into a liver sample (Fig. 5.1) and vibrated sinusoidally in time along its long axis by a mechanical actuator (SF-9324, PASCO Scientific, Roseville, CA). The actuator was driven by 500-ms-duration pure-tone voltage bursts (15 V) from a waveform generator at single frequencies in the range of 50 Hz to 300 Hz. In this range, the measured vibration amplitude was 10-250 μm. Vibration generates harmonic shear waves that propagate radially from the needle for several millimeters before the mechanical energy is absorbed. Shear waves are tracked with a Doppler probe, where actuator motion and Doppler transmissions are electronically synchronized. Imaging the needle and adjacent tissues simultaneously, we found there was negligible needle slippage.

A Sonix-RP system was used to estimate particle velocity as shear waves passed through the liver. A BW-14/60 linear-array transducer was driven by 6-cycle Doppler pulses at a center frequency of 6.67 MHz and a Doppler angle of 35 ° ± 5 °. The peak echo frequency was found to be ∼6 MHz. We used the default beamformer for the array resulting in 128 A-lines separated laterally by a 0.46-mm array pitch. We acquired a 3000-pulse ensemble of echoes at each of the 128 lateral spatial locations at a pulse repetition frequency of 10 kHz. Echoes were sampled in fast time at 40 Msamples/s and then downsampled internally by a factor of two before data were transferred for off-line processing on a PC. We summarize the estimation of shear wave speed from the Doppler echoes below; however, readers are referred to [20] for details.

The first 500-1000 Doppler traces are discarded to eliminate the shear-wave transient as the needle begins to vibrate. Particle velocity $\hat{v}(r, t, t_s)$ is then estimated from an ensemble grouping of six sequential echo traces in slow-time t_s using autocorrelation techniques [79]. This process yields ∼400 temporal velocity estimates at each radial location r and range time t. Note that in the shear-wave image shown below, the lateral dimension is r and the axial dimension is $z = ct/2$, where c is the compressional velocity. Shear speed c_s is estimated from the spatial wave phase as we now explain.

Let $\hat{v}'[\ell, n, m]$ be the discrete form of the complex analytic signal for particle velocity, where ℓ, n, m are integers. Here $r = \ell X$, $t = nT$, and $t_s = mT_s$ for sampling intervals in radial position, fast and slow times, $X = 0.46$ mm, $T = 25$ ns and $T_s = 0.1$ ms, respectively. We further average 40 velocity estimates along slow time (after the transient wave has dissipated) and compute a four-sample running mean in radial position to form the shear-wave spatial-phase estimate,

$$\bar{\psi}[\ell, n] = \frac{1}{40} \sum_{m=1}^{40} \frac{1}{3} \sum_{\ell'=\ell}^{\ell+3} \hat{v}'^{*}[\ell', n, m]\, \hat{v}'[\ell' + 1, n, m] \ . \tag{5.1}$$

At angular shear-wave frequency ω and tissue location $(r, z) = (\ell X, cnT/2)$, the shear-wave phase speed estimate is

$$\hat{c}_s(\omega, r, z) = \frac{\omega X}{\arg \bar{\psi}[\ell, n]} \ . \tag{5.2}$$

Equation 5.2 is a practical implementation of the phase gradient expression, $d\bar{\psi}/dr = \omega/c_s(\omega)$, which is derived in [20] based on the discussion in [85].

5.2.3 Complex Modulus Estimation

The complex shear modulus $\mu(\omega)$ is estimated from the shear speed dispersion curve, $c_s(\omega)$. The association between the two functions is through the complex shear wave number, $k_s(\omega) = \omega/c_s(\omega) + i\alpha_s(\omega) = (\rho\omega^2/\mu)^{1/2}$, where $\alpha_s(\omega)$ is the shear-wave attenuation coefficient and ρ is mass density. Expressing k_s in terms of real $\Re\{\cdot\}$ and imaginary $\Im\{\cdot\}$ components yields

$$c_s(\omega) = \omega/\Re\{k_s\} = \sqrt{\frac{2(\Re\{\mu\}^2 + \Im\{\mu\}^2)}{\rho(\Re\{\mu\} + \sqrt{\Re\{\mu\}^2 + \Im\{\mu\}^2})}} \tag{5.3}$$

and

$$\alpha_s(\omega) = \Im\{k_s\} = \sqrt{\frac{\rho\omega^2(\sqrt{\Re\{\mu\}^2 + \Im\{\mu\}^2} - \Re\{\mu\})}{2(\Re\{\mu\}^2 + \Im\{\mu\}^2)}} \tag{5.4}$$

that require adoption of a rheological model to carry out the computations.

The Kelvin-Voigt model illustrated in Fig. 5.2a is frequently employed in imaging experiments where forces are applied to a viscoelastic material and strain is measured over time. The complex modulus for the Kelvin-Voigt model,

$$\mu^K(\omega) = \mu_1 - i\omega\eta_K \ , \tag{5.5}$$

has one elastic and one viscous component in parallel. The elastic shear constant is μ_1, which is also referred to as the relaxed modulus because $\mu^K|_{\omega\to 0} = \mu_1$. The dynamic viscosity constant is η_K. Viscous dissipation of shear wave energy is also quantified by the quality factor $Q(\omega) = -\Re\{k_s^2\}/\Im\{k_s^2\}$, whose inverse is the dissipation factor Q^{-1} [75]. For the Kelvin-Voigt model,

$$Q^{-1}(\omega) = \omega\tau \ , \tag{5.6}$$

where $\tau = \eta_K/\mu_1$ is a relaxation time constant. The frequency dependance of Q^{-1} shows that K-V dissipation is unbounded and increasing with frequency. Thus the Kelvin-Voigt model describes the viscoelastic behavior of liver tissues as a low-pass filter of shear wave energy.

The Zener model illustrated in Fig. 5.2b adds an elastic element in series

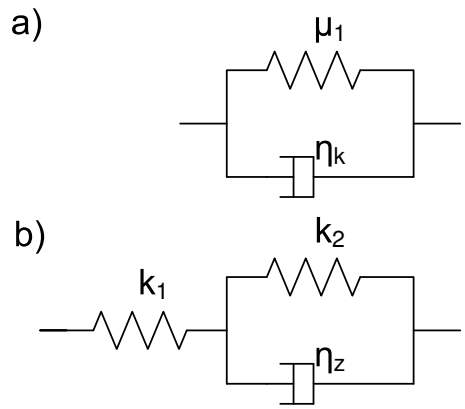

Figure 5.2: Parametric representations of the standard linear-solid two-parameter (Kelvin-Voigt) and three-parameter (Zener) rheological models. μ_1 is the elasticity shear constant, $\eta_{k,z}$ is the dynamic viscosity constant for the K-V or Zener models, and $k_{1,2}$ is an elastic spring constant.

with the K-V unit to allow for more complex dynamic behavior [75]. It has been shown to accurately represent the viscoelastic behavior of human liver, in vivo, in the shear frequency range of 25 to 62.5 Hz [94]. The complex modulus obtained from the Zener model is

$$\mu^Z(\omega) = \mu_1 \frac{1 + \omega^2 \tau_\sigma \tau_\epsilon}{1 + \omega^2 \tau_\sigma^2} - i\omega\mu_1 \frac{\tau_\epsilon - \tau_\sigma}{1 + \omega^2 \tau_\sigma^2} , \tag{5.7}$$

where $\mu_1 = \mu^Z \mid_{\omega \to 0} = k_1 k_2/(k_1 + k_2)$ is the relaxed modulus and $\tau_\sigma = \eta_Z/(k_1 + k_2)$ and $\tau_\epsilon = \eta_Z/k_2 \geq \tau_\sigma$ are associated relaxation times. For the Zener model,

$$Q^{-1}(\omega) = \omega(\tau_\epsilon - \tau_\sigma)/(1 + \omega^2 \tau_\epsilon \tau_\sigma) . \tag{5.8}$$

Systems represented by the Zener model exhibit purely elastic behavior at both ends of frequency spectrum where $Q^{-1} \to 0$. Moreover, there exists a relaxation peak at $\omega_0 = 1/\sqrt{\tau_\epsilon \tau_\sigma}$ and viscous losses are greatest. Thus the Zener model describes the viscoelastic behavior of liver tissue as a band-stop filter of shear wave energy.

5.2.4 Rheometer Testing

Liver samples were cut into cylindrical slabs to measure the shear stress relaxation using a controlled shear-strain rheometer (TA Instruments, Model

AR-G2, New Castle, DE, USA). The rheometer had parallel circular plate fixtures, each 25 mm in diameter. Liver samples were first cut into slabs approximately 5 mm thick and then cut into cylinders 25 mm in diameter using a circular punch. To avoid having samples slip when torqued, a waterproof sandpaper was fixed to the upper and lower rheometer plate surfaces. A small compressive load (<0.1 N) was applied to samples to ensure contact with the sandpaper and minimize slippage. A 5 % rotational strain was applied to each sample for a period of 30 minutes with a one-second ramp-on time to study shear relaxation. Time-varying torque measurements were analyzed to estimate relaxation moduli through a third-order generalized Maxwell model as previously described [19]. No preconditioning was applied to liver samples.

5.2.5 Liver Density

The mass density of liver samples was estimated in an independent measurement by applying Archimedes' principle. Liver samples free from major blood vessels were cut into roughly 10 g cubes and submerged into a beaker with 400 g of distilled water at 23 °C. Samples immediately sank to the bottom. Sodium chloride (Sigma Aldrich, inc., St. Louis) was added in 0.5 g increments and dissolved until the sample began to float. Then sodium chloride was added in 0.05 g increments until the liver became neutrally buoyant. Assuming the density of water is 1.00 g/cm^3 and the density of sodium chloride is 2.16 g/cm^3, we computed the density for three fresh and three thermally-damaged samples. Results are summarized in Table 5.1.

Table 5.1: Measured density of fresh and thermally damaged porcine liver at 23 °C.

Fresh tissue [g/cm^3]	TD tissue [g/cm^3]
1.05	1.06
1.07	1.05
1.05	1.05
1.06 ± 0.01	1.06 ± 0.004

Our measurement values agree with others from the literature, where the density of porcine liver was reported to be 1.064 g/cm^3 at 37 °C [95]. Our

intention was not to characterize samples based on density, but to demonstrate that there is not a measurable difference between densities that could bias modulus estimates.

5.3 Results

Figure 5.3 is an example of a particle velocity image showing 100 Hz shear waves propagating from a vibrating needle through fresh porcine liver. The needle is located near the center of the dark ellipse. The shape of the wavefront is tilted because of the 35○ angle between the Doppler beam axis and the needle axis. Under these conditions, shear waves propagate at least one wavelength, about 16 mm.

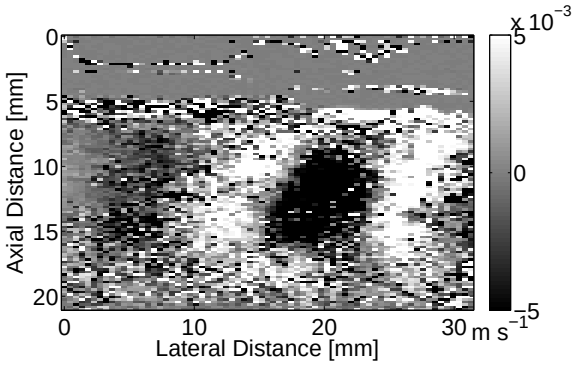

Figure 5.3: Particle velocity image of a 100 Hz shear wave in fresh porcine liver tissue from one RF frame. Waves are generated by a needle vibrating near the dark elliptical center. The top surface of the sample is located at a depth of 5 mm.

Shear speed measurements between 50 and 300 Hz in steps of 50 Hz are computed for each of the three fresh and three thermally damaged liver samples. Values plotted in Fig. 5.3 are the average of the three samples at a given frequency. The Kelvin-Voigt and Zener models were numerically fit to the measured data using methods described previously [20]. Lines plotted in the figure result from the parameters that gave the least-squares fit of model functions to speed measurements. Table 5.2 lists those parameters along with μ_1 estimates obtained from rheometer stress-relaxation measurements on samples from the same livers. Applying K-V model parameters to Eq. 5.4,

Table 5.2: Estimated viscoelastic parameters.

Rheo. Model	Porcine Liver	μ_1 [kPa]	η_K [Pa s]		
K-V	Fresh	2.2	1.8		
K-V	Therm. Dam.	5.0	5.8		
			k_1 [kPa]	k_2 [kPa]	η_Z [Pa s]
Zener	Fresh	1.8	6.2	2.6	4.99
Zener	Therm. Dam.	3.7	18	4.6	12
Rheom., 2% Strain	Fresh	0.06 ± 0.03			
Rheom., 5% Strain	Fresh	0.09 ± 0.02			
Rheom., 2% Strain	Therm. Dam.	0.14 ± 0.01			
Rheom., 5% Strain	Therm. Dam.	0.15 ± 0.06			

we found at 100 Hz that $\alpha_s = 0.94$ cm^{-1} for fresh liver and $\alpha_s = 0.79$ cm^{-1} for thermally damaged liver.

We conducted a two-sample, unpaired, two-tailed Student's t-test of the null hypothesis that heating does not alter the shear speed of liver. Hypothesis testing was conducted at each frequency in Fig. 5.4 where shear speeds were estimated. The untested assumption is that tissue samples from the fresh and thermally damaged classes of liver are normally distributed with equal variance. There were three measurement samples from each liver class, and we estimated class means from those samples. Therefore there are four degrees of freedom. We found for speed estimates at the six frequencies that the corresponding p value fell in the range of $0.0145 \leq p \leq 0.0458$. Therefore we must reject the null hypothesis at the significance level of 0.05 and conclude, within the limits of the assumptions, that shear speed measurements of fresh and thermally damaged liver are distinct.

There is a small difference between dispersion curve models seen in Fig. 5.4 (left). Consequently, either rheological model may be used to represent measured shear speeds within measurement error. From the model parameters of Table 5.2, we generated mechanical dissipation curves Q^{-1} for the two models via Eqs. 5.6 and 5.8 and plotted them in Fig. 5.4 (right). While the K-V model predicts a monotonic increase in wave energy loss with shear-wave frequency, the Zener model exhibits a dissipation resonance peak at $\omega_0/2\pi = 153$ Hz for fresh tissue and $\omega_0/2\pi = 135$ Hz for thermally damaged liver tissue. Above ω_0, the two models clearly diverge. Unfortunately, we

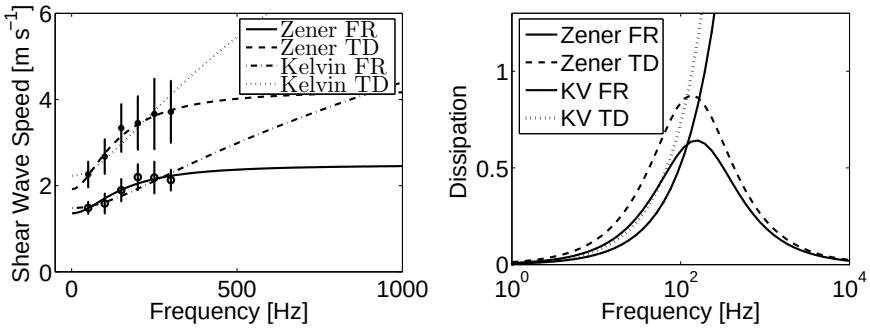

Figure 5.4: Comparison of shear wave speeds (left) and dissipation factors (right) as a function of frequency for the Kelvin-Voigt and Zener models for both fresh (FR) and thermally-damaged (TD) porcine liver. Measurements are indicated by points that specify the mean ± 1 SD.

were unable to obtain reliable shear speed estimates above 300 Hz in liver. We discuss the possible implications of this observation in the next section.

5.4 Discussion

The complex modulus was estimated from shear wave images obtained in large tissue samples that included at least one entire liver lobe. Reflected waves at tissue boundaries were negligible because of high shear-wave attenuation. We considered that non-physiological conditions, such as the lack of liver perfusion and room temperature measurements, could affect the results as compared with in vivo findings. Others [96] found that non-perfused porcine livers were stiffer and more viscous under cyclic compressive loads, and the effects were found to be more pronounced when large preloads were applied to the liver. The shear-displacement amplitudes in our study produced strains <1% and there was no preload. Consequently, liver perfusion and temperature were not expected to be a major influence on viscoelastic properties, provided there was little degradation of the protein structure.

We attempted to validate our shear-wave measurements of the elastic shear constant μ_1 through comparisons with independent rheometer measurements of μ_1. We found reasonably close agreement between rheometer and shear-wave estimates for gelatin in a previous study [20]; however, Table 5.2 shows no such agreement for liver tissue. Estimates of μ_1 derived from the two techniques can be expected to agree for linear viscoelastic media, as we found

gelatin to be, but liver parenchyma is known to deform nonlinearly. Indeed, Liu and Bilston [97] found that shear relaxation moduli measured for bovine liver demonstrated significant strain and strain-rate sensitivities above 0.2% strains. Lacking an independent standard measurement, we decided to compare our measurements with those published by other labs.

In Fig. 5.5 (left) our measurements from Fig. 5.4 may be compared to those of Chen et al. [18] who applied a shear-wave dispersion ultrasound vibrometry (SDUV) method to in vivo porcine liver. The principal experimental differences are their use of radiation force and their use of perfused liver measured near normal body temperature. These authors measured speed from the spatial phase shift over a distance of 3-5 mm in liver and assumed the K-V model when relating dispersion to modulus constants. There is close agreement between shear speed estimates for the two labs up to 300 Hz. It is not surprising then that the complex modulus constants from the two labs are similar for porcine liver: 2.2 kPa, 1.8 Pa·s (UIUC) and 2.4 kPa, 2.1 Pa·s (Mayo). The agreement suggests that liver perfusion, temperature, and measurement technique are not major factors in shear-wave measurements of μ_1.

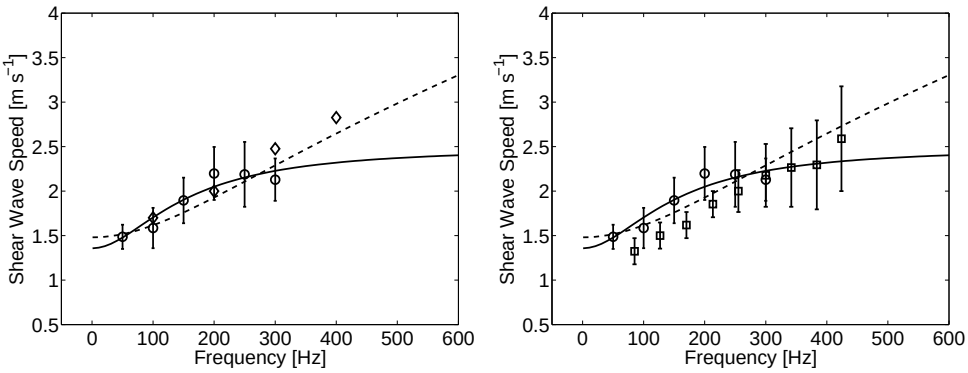

Figure 5.5: Shear wave speed measurements in fresh ex vivo porcine liver from Fig. 5.4 are compared with two other measurement sets reported in the literature. Our measurements (circle-labeled points with error bars in both plots) and best-fit model curves are compared with the measurements of (left) Chen et al. ([18], Fig. 6d), as indicated by diamond-labeled points, and (right) Deffieux et al. ([39], Fig. 11, second volunteer), as indicated by square-labeled point with error bars. The K-V model values are indicated by the dashed curve and the Zener model values are indicated by the solid curve.

In Fig. 5.5 (right) our same measurements may also be compared to those

of Deffieux et al. [39]. They developed a supersonic shear imaging technique (SSI) for in vivo shear wave spectroscopy (SWS), and they adopted the K-V model to relate shear speed to modulus constants. Their in vivo measurements on healthy livers of human volunteers yielded speed estimates that are statistically comparable to ours made on excised porcine liver. Shear speed values appear to be slightly lower for human data relative to pig, which is consistent with the slightly lower value of μ_1 reported by Chen et al. citechen09 for humans via MRE methods relative to pigs. Although the findings are consistent and perhaps expected given known differences in lobular collagen content between humans and pigs, none of the observed species-specific differences in shear properties can be considered statistically significant when measurement uncertainties are considered.

Conversely, heating increased the stiffness and viscosity of ex vivo liver tissue, as detected by the significant increase in shear wave speed observed (Fig 5.4). Assuming the heating regimen that we adopted [93] produces protein denaturation and coagulative necrosis similar to that found following in vivo liver ablation procedures [98], then it seems that thermally-induced biochemical changes to liver tissue influence the complex modulus to a greater extent than variations in anatomical structure. For example, the histology displayed in Fig 5.1 showed no apparent thermally-induced changes in cellular architecture. We estimate a doubling of μ_1 in thermally damaged liver compared to fresh liver. Others found as much as a fourfold increase in μ_1 that varied systematically with heating time and rate [99]. Previous results formed the basis for more recent studies exploring the use of elasticity imaging methods to track the growth of thermal lesions during ablation procedures [100, 101]. Our contribution to these results is the findings of Table 5.2 that the dynamic viscosity constant η increases threefold after thermal damage as compared to a doubling of μ_1. Thus η could be a more robust parameter for viscoelasticity imaging of thermal lesion growth in the 50-300 Hz bandwidth provided its measurement uncertainty is comparable to that observed for μ_1.

Our technique does not provide enough measurement bandwidth to conclude whether one rheological model is more representative of liver dispersion. It is possible that our inability to easily sense shear-wave energy in liver above 300 Hz could be an indication that dissipation increases with frequency, as occurs directly with the K-V model. Fitting the first-order Zener model to liver

dispersion measurements predicts a dissipation resonance at $\omega > \omega_0 \simeq 150$ Hz, and the nonintuitive result that attenuation should decrease with frequency. Adding more Kelvin-Voigt units in series with the first-order Zener model (Fig. 5.2b), each having increasing resonance frequency, would provide more degrees of freedom for modeling. Yet our confidence in modeling results degrades as the number of fit parameters increases without also increasing data samples. It is also true that as shear-wave frequency increases, the amplitude of the mechanical actuator is reduced [20], and the potential for the needle slipping against the tissue is greater.

Determining the lowest-order constitutive model that best represents dispersion data up to about 1 kHz could provide new insights into the sources of viscoelastic tissue contrast created through disease processes or applied therapeutics. Model parameters conveniently summarize macroscopic rheological behavior of tissues, which offers us intuition regarding the relative degrees of elastic and dissipative responses that we often relate to constituent tissue components. What are the components of tissue that interact with shear wave energy? We believe that, with extension of the measurement bandwidth, some of the answers are emerging. Specifically, consider the work of Frizzell et al. [102] and Madsen et al. [84] who made measurements at 2-14 MHz, a frequency band five orders of magnitude higher.

At shear-wave frequencies below 500 Hz, the wavelength is on the order of centimeters. At 8 MHz, the wavelength is just 6 μm. One might expect modulus values to vary significantly between these bandwidths if tissue structures larger than cells were responsible for the interaction. In the 50-300 Hz range for porcine and human liver, we measured shear speeds between 1-3 m/s and shear attenuation coefficients less than 2 cm^{-1}. At frequencies of 2-14 MHz, Frizzell and Carstensen and Madsen et al. each independently measured shear-wave speeds at room temperature for bovine, rodent, and canine liver samples in the range of 10-60 m/s and shear attenuation coefficients in excess of 10^4 cm^{-1}. Yet they found for bovine liver in the MHz range and assuming a K-V model that $\mu_1 = 2.3$ kPa, in line with measurements made at much lower frequencies, e.g., those in Table 5.2. They also found $\eta = 0.013$ Pa·s, lower by two orders of magnitude in the MHz frequency range as compared to the Hz range. (Note that η is weighted by frequency in the expression for shear attenuation coefficient.) The apparent frequency dependence of η is evidence that the K-V model is incomplete.

A similar conclusion was reached by others independently. It was found that a power-law relationship describing shear attenuation, which is based on the Kelvin-Voigt model, was unable to represent the fractional power-law relationship observed in soft biological tissue [23]. Szabo and Wu [103] reached the same conclusion during their study of polymer materials. They proposed a theoretical framework based on the K-V model that expands the dynamic viscosity component with fractional-derivative-like terms, effectively making a frequency dependent η for the K-V model. This modification implies that classical models with combinations of springs and dashpots cannot model the shear modulus over the measurable frequency range. However, below 300 Hz, we and others found that the modulus is sensitive to thermal history and yet parametric models respond similarly so it is unnecessary to choose one over another.

Conversely, the elastic shear constant μ_1 measured in the frequency range of 50-300 Hz is comparable to values measured in the MHz range, which suggests that μ_1 could be frequency independent as predicted by the K-V model. Shear measurements between 500 Hz and 1 MHz are needed to verify frequency independence. Parameter μ_1 appears to be invariant for liver among the mammalian species examined. While there are obvious macrostructural differences among the livers of various species, the cellular biochemistry and structure are very similar as are μ_1 estimates. Heating tissues, however, increases the average stiffness as it induces cellular necrosis and collagen fiber cross-linking. Thus shear-wave energy interacts primarily with protein and other molecular-scale structures that are common among species but can change with disease. Absorption of shear wave energy in liver is much stronger than scattering at all frequencies, apparently even more so than it is for compressional waves [104].

5.5 Conclusion

Several aspects of shear wave imaging in soft biological tissues are studied and yield the following conclusions. First, the Kelvin-Voigt rheological model predicts an elastic shear constant $\mu_1 \sim$2 kPa for liver tissue over two distinct bandwidths of shear-wave frequencies: 50-300 Hz and 2-14 MHz. The elastic shear constant is invariant with mammalian species and degree of perfu-

sion. Yet μ_1 is a sensitive indicator of thermal damage, a process known to modify tissue macromolecules. The dynamic viscosity "constant" η for liver tissue was found to vary significantly between the same two measurement bandwidths, and yet it exhibits greater sensitivity than μ_1 to thermal damage. Taken together, the data suggest the K-V model may be an incomplete model but is adequate for assessing thermal effects below 300 Hz. Dispersion measurements made at shear-wave frequencies between 0.5 and 1000 kHz are needed to define the most appropriate and concise rheological model for representing viscoelastic behavior of liver.

Second, shear waves interact with mammalian tissue predominantly at the molecular scale through absorption. Consequently, elasticity imaging contrast from disease-induced changes can be expected to occur at a subcellular scale, and is not greatly affected by tissue structures larger than a cell. Macromolecular changes that increase the complex modulus in heated liver could have counterparts in disease formation and therapeutic responses that also provide contrast. We need to more closely consider the role of molecular processes in elasticity contrast, and to more completely probe the shear-wave frequency landscape to find constitutive models that concisely represent tissues.

The third and most important contribution of this chapter, is the evidence that reconstruction of complex shear modulus has an added value in information. This is reflected in our finding that the viscous component can provide more contrast in detection of thermal damage than the elastic component. For the given conditions of the experiment, we have found a twofold increase in the value of estimated shear elastic modulus versus threefold increase in the value of estimated shear dynamic viscosity assuming K-V model.

In summary, the proposed method for the reconstruction of the complex shear modulus based on the phase gradient approach was successfully used in characterization of fresh and thermally damaged porcine liver. Results suggest that dynamic viscosity exhibits greater sensitivity to thermal changes in soft biological tissues. Hence, it can provide more contrast in the reconstruction of the underlaying soft tissue material properties.

CHAPTER 6

3-D FDTD SIMULATION OF SHEAR WAVES FOR EVALUATION OF COMPLEX MODULUS IMAGING

6.1 Introduction

The goal of the work presented in this chapter is to image the spatial variability of complex shear modulus constants in heterogeneous media. For this work, we adapted a widely-used technique that directly inverts the wave equation [105, 22]. It allows for the estimation of modulus constants as a function of position and at individual shear-wave frequencies. Shear waves are sensed by scanning the medium with pulsed Doppler pulses to estimate particle velocities as described previously [20]. Velocity maps are processed to reconstruct modulus images using the Algebraic Helmholtz Inversion (AHI) method [106]. This algorithm operates under the assumptions that medium dynamics are linear, isotropic, and piecewise homogeneous. It is found that dynamic imaging techniques can yield artifacts in elastic shear modulus images near the surface of heterogeneities, and these artifacts appear to be related to approximations made when processing data to form images.

To study limitations imposed by the various assumptions, a 3-D shear-wave simulator is developed that accurately represents wave propagation in heterogeneous media. Gelatin phantom studies, with known geometry and mechanical properties, cannot address all of these questions, largely because gelatin gels exhibit a relatively weak viscous response, unlike many soft tissues. A finite-difference time-domain analysis was developed for simulating shear-wave propagation in time and three spatial dimensions for heterogeneous media (3-D FDTD solver). These numerical methods are based on an extensive seismic research literature, e.g., [107, 108, 109]. In this chapter, the sensitivity of various assumptions intrinsic to the AHI algorithm is tested by

This chapter is adapted from M. Orescanin, Y. Wang, and M. F. Insana, "3-D FDTD Simulation of Shear Waves for Evaluation of Complex Modulus Imaging," *IEEE Transactions on Ultrasonics, Ferroelectrics and Frequency Control*, 2010. Used with permission.

comparing imaging results from simulated and experimental data.

The rest of this chapter is organized as follows. In Section 6.2 the adopted 3-D FDTD numerical approach is described. Furthermore, the adaptation of the algebraic Helmholtz inversion is presented in Subsection 6.2.2. Experimental verification of the proposed numerical approach is presented in Section 6.3 together with the AHI inversions on both numerical and experimental phantoms. In Section 6.4 the effect of viscosity on the AHI reconstructions is studied with the help of the proposed simulator. A summary of findings is presented in Section 6.5.

6.2 Methods

The next section describes the forward problem of simulating shear waves induced by a vibrating needle. We then summarize the inverse problem by describing our adaptation of the AHI algorithm for modulus image formation. Finally, we describe the experimental techniques used to validate the 3-D FDTD solver for simulating shear waves.

The following section uses the notation ∂_t to represent a partial derivative operator $\partial/\partial t$ applied to values to the right of the symbol.

6.2.1 Numerical Approach

Although the equations of motion can be formulated in several ways, we chose a velocity-stress formulation for an assumed isotropic medium [107]. That is, we propagate in time distributions of velocity and stress at spatial points on a regular grid to which material properties (complex modulus and density) and sources of mechanical energy are assigned. The velocity maps may be related directly to Doppler-detected particle velocity fields measured experimentally.

Generally a system of nine first-order hyperbolic equations is needed to describe wave propagation in 3-D space. Shear waves were generated by a needle vibrating sinusoidally along its long axis, in part, to minimize compressional wave energy and thus reduce the computational load. Assuming negligible compression, we may zero the normal stress components and assume an incompressible medium to describe pure shear-wave propagation.

The remaining six first-order hyperbolic equations expressed in terms of stress tensor σ and velocity vector v for a viscoelastic medium are

$$\begin{aligned}
\rho\partial_t v_x &= \partial_y\sigma_{xy} + \partial_z\sigma_{xz} \\
\rho\partial_t v_y &= \partial_x\sigma_{yx} + \partial_z\sigma_{yz} \\
\rho\partial_t v_z &= \partial_x\sigma_{zx} + \partial_y\sigma_{zy} \\
\partial_t\sigma_{xy} &= (\mu + \eta\partial_t)\,(\partial_y v_x + \partial_x v_y) \\
\partial_t\sigma_{xz} &= (\mu + \eta\partial_t)\,(\partial_z v_x + \partial_x v_z) \\
\partial_t\sigma_{yz} &= (\mu + \eta\partial_t)\,(\partial_z v_y + \partial_y v_z)\ .
\end{aligned} \tag{6.1}$$

The mass density is ρ and is assumed to be spatially constant throughout the medium. The complex shear modulus is $G(\boldsymbol{x},\omega) = \mu(\boldsymbol{x}) - i\omega\eta(\boldsymbol{x})$, where $\mu(\boldsymbol{x})$ is the elastic shear constant and $\eta(\boldsymbol{x})$ is the dynamic viscous constant that can each vary with position $\boldsymbol{x}$. This form of G results from selecting the Kelvin-Voigt model.

As Virieux [107] describes, stable spatial discretization is achieved with the finite-difference grid illustrated in Fig. 6.1. Time is uniformly sampled via $t = n\Delta t$ for integer n and interval Δt. Similarly, space is uniformly sampled where integer indices i, j, k count intervals Δx, Δy, Δz to form Cartesian coordinates x, y, z, respectively. Velocity components are specified at grid positions that are offset by half intervals from the corresponding stress components.

To propagate spatial quantities in time, the classic time-staggering approach is often used to estimate stress and velocity at alternating time intervals. We chose an alternative method, the *forward-backward differencing* technique [110], where velocities and stresses are computed at each time interval. The system is initially at rest so that we can view the initial transient response if needed. Issues of computational load, memory usage, and stability should be considered when deciding between approaches. Readers are referred to the book by Durran [110] for this discussion.

The net FDTD approach is illustrated by expressing the first and fourth

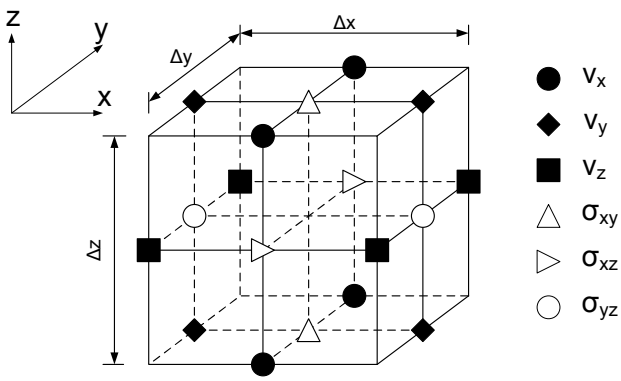

Figure 6.1: Diagram of the staggered grid discretization of the medium with positions of the wave-field variables. Black symbols denote particle velocities and white symbols denote stresses.

lines in Eq. 6.1 in discrete form as follows:

$$\begin{aligned} v_x^{n+1}|_{i,j,k} &= v_x^n|_{i,j,k} + \frac{\triangle t}{\rho \triangle y}(\sigma_{xy}^n|_{i,j+\frac{1}{2},k} - \sigma_{xy}^n|_{i,j-\frac{1}{2},k}) \\ &+ \frac{\triangle t}{\rho \triangle z}(\sigma_{xz}^n|_{i,j,k+\frac{1}{2}} - \sigma_{xz}^n|_{i,j,k-\frac{1}{2}}) \end{aligned} \tag{6.2}$$

$$\begin{aligned} \sigma_{xy}^{n+1}|_{i,j+\frac{1}{2},k} &= \sigma_{xy}^n|_{i,j+\frac{1}{2},k} + \frac{\mu \triangle t}{\triangle y}(v_x^{n+1}|_{i,j+1,k} - v_x^{n+1}|_{i,j,k}) \\ &+ \frac{\mu \triangle t}{\triangle x}(v_y^{n+1}|_{i+\frac{1}{2},j+\frac{1}{2},k} - v_y^{n+1}|_{i-\frac{1}{2},j+\frac{1}{2},k}) \\ &+ \frac{\eta}{\triangle y}(v_x^{n+1}|_{i,j+1,k} - v_x^{n+1}|_{i,j,k}) \\ &- \frac{\eta}{\triangle y}(v_x^n|_{i,j+1,k} - v_x^n|_{i,j,k}) \\ &+ \frac{\eta}{\triangle x}(v_y^{n+1}|_{i+\frac{1}{2},j+\frac{1}{2},k} - v_y^{n+1}|_{i-\frac{1}{2},j+\frac{1}{2},k}) \\ &- \frac{\eta}{\triangle x}(v_y^n|_{i+\frac{1}{2},j+\frac{1}{2},k} - v_y^n|_{i-\frac{1}{2},j+\frac{1}{2},k}) \ , \end{aligned} \tag{6.3}$$

where spatial indices are subscripts and temporal indices are superscripts. To ensure numerical stability, spatial heterogeneities are handled by volume harmonic averaging of $\mu(\boldsymbol{x})$ and $\eta(\boldsymbol{x})$ with their 26 nearest neighbor grid values [108, 109]. A straightforward augmentation to the derivations for elastic media found in [108] allowed us to include viscoelastic properties.

Reflections at outer boundaries of the simulation domain were minimized

by applying an absorption boundary layer. The layer is defined by a loss profile chosen within a perfectly matched absorptive layer (PML) [109, 111]. The attenuation factor τ is given by

$$\tau(i) = \tau_{max} \left(\frac{i - i_{pml}}{N_{pml}} \right)^m \tag{6.4}$$

where we set $m = 2.1$ and $\tau_{max} = 0.1$. The term $i - i_{pml}$ indicates position within the PML and $N_{pml} = 10$ is the layer thickness in grid points. For example, within the layer near field boundaries, the velocity $v_x^{n+1}|_{i_{pml}} = v_x^{n+1}|_i - \tau(i)(v_x^{n+1}|_i - v_{target})$, where $v_{target} \to 0$.

The vibrating needle source was introduced to the simulation by setting v_z at grid points within the needle at the instantaneous vibration amplitude. Because grid sampling in the plane normal to the needle axis was set to $\triangle x = \triangle y = 1$ mm, the needle was modeled with a 1 mm $\times$ 1 mm cross sectional profile.

The FDTD algorithm was implemented in a fully parallel fashion using the C language and parallelized using OpenMP API. The code was written to run on two systems: a dual core workstation and a multi-core SGI Altix supercomputer at the National Center for Supercomputing Applications (NCSA) located at the University of Illinois campus.

6.2.2 Direct Inversion of the Wave Equation

In this section, we describe the AHI algorithm for imaging the complex modulus from the spatial patterns of measured or simulated shear waves.

Assuming that the viscoelastic properties of the medium are isotropic and there is negligible compression applied to the medium by the source, the particle velocity vector $\boldsymbol{v} = (v_x, v_y, v_z)$ can be described by the Navier wave equation in a homogeneous solid,

$$\rho \frac{\partial^2 \boldsymbol{v}(\boldsymbol{x}, t)}{\partial t^2} = G'(\boldsymbol{x}, t) \nabla^2 \boldsymbol{v}(\boldsymbol{x}, t) \ . \tag{6.5}$$

Under these assumptions, it is sufficient to estimate just one velocity component, e.g., v_z, to estimate modulus values. Component v_z is selected because the axes of the Doppler beam and needle are aligned with the z axis. Consequently, each pulsed Doppler echo frame forms a plane where scattering

particles move vertically and shear waves move horizontally.

Direct inversion of the wave equation solves Eq. 6.5 for the complex modulus either in the time domain $G'(\boldsymbol{x}, t)$ or temporal frequency domain $G(\boldsymbol{x}, \omega)$. When the temporal Fourier transform of particle velocity exists, frequency-domain inversions are desired to reduce the number of derivatives calculated on noise corrupted particle velocity fields [22].

The needle is vibrated harmonically in time according to $-v_0 \sin(\omega_o t)$, so we begin by taking the temporal Fourier transform of the particle velocity maps in a region surrounding the source, i.e., $V_z(\boldsymbol{x}, \omega_0) = \mathcal{F}_t\{v_z(\boldsymbol{x}, t)\}|_{\omega=\omega_0}$, saving only the value at the excitation frequency ω_0. This is a noise reduction process, whereby many time-varying velocity estimates measured at each spatial location are compressed into a single complex number. Equation 6.5 becomes the Helmholtz equation

$$\left(\frac{G(\boldsymbol{x}, \omega)}{\rho} \nabla^2 \; + \; \omega^2 \right) V_z(\boldsymbol{x}, \omega) \Big|_{\omega=\omega_0} = 0 \; , \tag{6.6}$$

where for $G(\boldsymbol{x}, \omega_0) = \mu(\boldsymbol{x}) - i\omega_0 \eta(\boldsymbol{x})$ direct inversion yields

$$\mu(\boldsymbol{x}) = \Re \left\{ \frac{-\rho\omega^2 V_z(\boldsymbol{x}, \omega_0)}{\nabla^2 V_z(\boldsymbol{x}, \omega_0)} \right\}, \quad \eta(\boldsymbol{x}) = \Im \left\{ \frac{-\rho\omega V_z(\boldsymbol{x}, \omega_0)}{\nabla^2 V_z(\boldsymbol{x}, \omega_0)} \right\} \; . \tag{6.7}$$

We investigated how modulus parameters are distorted when this algebraic Helmholtz inversion of velocity data is applied in two spatial dimensions instead of three. Specifically, we asked what is the effect of using either $v_z(x, z, t)$ or $v_z(x, y, z, t)$ to compute the Laplacian? In the 2-D case, $\partial^2 v_z / \partial y^2$ was set to zero, where the y axis is normal to the scan plane of the Doppler probe. We examined related effects of material property symmetry in this regard.

Prior to applying Eq. 6.7, we spatially filter $V_z(\boldsymbol{x}, \omega_0)$ in three dimensions using a low-pass second-order Butterworth filter with a cutoff frequency of 160 m^{-1}. Since the direct inversion process is not regularized, spatial filtering is essential [106]. For 2-D reconstructions, we filter with a 2-D low-pass Butterworth filter. After inversion, μ and η images are again spatially filtered by a median filter with a symmetric kernel size of 15 in either two or three spatial dimensions.

6.2.3 Experimental Approach

This section introduces our experimental approach to 3-D shear wave imaging. We begin by explaining the synchronized acquisition of Doppler echo signals that effectively samples shear waves in a volume up to 1000 volumes per second. We review the process of estimating velocity from echo signals, and finish by summarizing the procedure for heterogeneous phantom preparation.

Data Acquisition

Ideally we would transmit and receive Doppler echoes from the entire scan volume simultaneously at a rate more than twice the highest shear wave frequency and with a spatial sampling that prevents spatial aliasing. Without this capability, we are relegated to sequential echo acquisitions where time series of echo signals are recorded in phase with the vibration of the needle. Our method is to record a 3000-pulse Doppler ensemble at a rate of 8000 pulses/s sequentially for each value on the x, y plane sampling grid (0.46 mm $\times$ 1.0 mm). Echoes are recorded as a function of fast and slow time without moving the aperture, as is the convention for spectral Doppler recordings. Fast-time series samples give range echoes along the z-axis, while slow-time series samples become the velocity time axis t. We then index the beam aperture electronically along the lateral x axis and mechanically along the elevational y axis to obtain ensembles from the entire volume and in time but always synchronized to the phase of the vibrating needle. Phase-lock repeatability of the acquisition was tested previously [20]. Each 3-D acquisition requires several hours to scan one phantom at each shear wave frequency.

Doppler Imaging

A Sonix-RP system (Ultrasonix Medical Corporation, Richmond, Canada) was used to transmit and receive narrow-band Doppler pulses as described above. We used two sequential linear array transducers (BW-14/60 and BW-14/40) that differed in the lateral line density and extent (x axis) of the recorded field. Six-cycle pulses were transmitted at a center frequency of 6.67 MHz and a zero Doppler angle (beam and needle axes were parallel).

The peak echo frequency was found to be $\sim$ 6 MHz. We used the default beamformer resulting in 128 A-lines separated laterally by a 0.46-mm array pitch for a BW-14/60 and 0.3-mm array pitch for BW-14/40. The 3000-pulse ensemble was recorded at each of the 128 lateral spatial locations. Echoes were sampled in fast time at 40 Msamples/s and then downsampled internally by a factor of two before data were transferred for off-line processing on a PC. The slow-time sampling rate was 8 kilo-pulses/s.

At each spatial position, the 3000 time series in the echo ensemble were divided into six sequential, non-overlapping groups to estimate instantaneous particle velocities using a lag-5 autocorrelator [20]. Thus, at every point in the volume, we acquired a time series of 500 velocity estimates at an effective sampling interval of 0.75 ms. This velocity estimator was described previously [20]. The spatial sampling intervals for velocity estimates were 0.46 mm $\times$ 1.0 mm $\times$ 0.39 mm for the BW-14/60 array (lateral x, elevational y, range z) and 0.30 mm $\times$ 1.0 mm $\times$ 0.39 mm for the BW-14/40 array. For both transducers, the range interval of 0.39 mm was determined by downsampling velocities a factor of 10 using averaging.

Phantom Preparation

Gelatin gel phantoms (250 bloom strength, Type B, Rousselot, Buenos Aires, Argentina) were constructed for two purposes. First, we validated the accuracy of shear waves simulated by the FDTD solver. Second, we tested the accuracy of the AHI algorithm at forming elastic modulus images from shear wave measurements. Independent measurements of the elastic modulus for each phantom component were obtained during a prior study [19, 20].

Using construction techniques described in [20], a molten gelatin preparation containing undissolved cornstarch particles is poured into an acrylic mold (height 9.5 cm, width 9.5 cm and length 12.5 cm) and sealed. Within the acrylic box, there is a solid cylindrical rod (15-mm dia) fastened to opposite interior walls and sprayed with a mold release. The rod creates a void where later the inclusion will be formed. The solution is allowed to congeal quiescently at room temperature for 24 hrs. Then the acrylic rod is removed and molten gel of different gelatin concentration is poured into the cylindrical void. This heterogeneous phantom is again sealed and allowed to congeal for another 24 hrs before testing.

Phantoms were constructed with a gelatin concentration of 8% (by weight) in the background and 4% in the inclusion. The background and inclusion regions contained 3% and 6% cornstarch, respectively. Two nominally identical phantoms were constructed weeks apart, one for each experiment at 100 Hz and 150 Hz shear wave frequencies.

6.3 Results

In the following section we compare particle velocity images from shear waves simulated using the 3-D FDTD solver with those measured experimentally in a gelatin phantom for matched conditions. We then apply the AHI algorithm to both types of data to form shear modulus images using either 2-D or full 3-D velocity maps.

6.3.1 Experimental Validation

A needle was inserted about 5 cm into a phantom for shear wave imaging. The needle axis was oriented parallel to the axis of the soft, 15-mm diameter cylindrical inclusion (along the z axis) but the two axes were separated by approximately 20 mm. The two C-scans in the left column of Fig. 6.2 display x, y image planes at a z-axis depth of several centimeters below the top surface of the phantoms. The view is from the Doppler probe looking down the beam axis. The needle is positioned about 15 mm above the top of the images (out of view) and vibrated along its long axis.

The three images in the top row of Fig. 6.2 were generated for one of the two phantoms at a needle vibration frequency of 100 Hz. The bottom row of three images was generated for the second phantom at a needle vibration frequency of 150 Hz. The pitch and length of the linear arrays are different for the two phantoms, as described above, which changes pixel sizes and makes the circular cross sections of the inclusion appear different sizes.

The middle column of images in Fig. 6.2 are the experimentally recorded maps of particle velocity caused by cylindrically diverging shear waves radiating from the needle. Images in the right column are numerically simulated with the 3-D FDTD solver for the same experimental conditions. Black and white pixels indicate motion along the z axis, away and toward the probe.

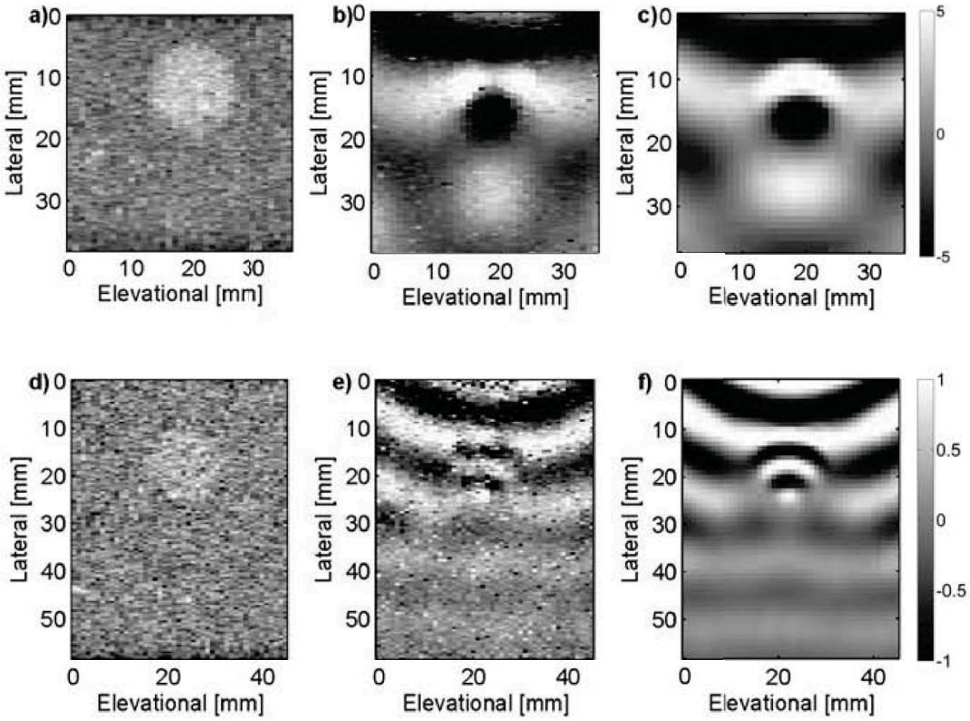

Figure 6.2: Phantom images for comparing FDTD simulations with Doppler measurements of shear-wave-induced particle velocities. The velocity range displayed is ±5 mm/s in the top row and ±1 mm/s in the bottom row. The needle source (positioned approximately at (22 mm, -5 mm)) was vibrated at 100 Hz (top row) and 150 Hz (bottom row). (a) and (d) are 6 MHz C-scans of the phantom, (b) and (e) are measured shear wave images. (c) and (f) are simulated under the same conditions. Bright and dark regions indicate particle velocities toward and away from the Doppler probe. The lateral dimension is the x axis and the elevational dimension is the y axis. The Doppler linear array aperture was oriented vertically with the beam oriented into the scan plane.

We measured modulus constants in the phantoms and applied those values in the simulations. The spatially averaged values in the inclusion at 100 Hz were found to be $\mu_{inc} = 1.1$ kPa and $\eta_{inc} = 0.1$ Pa·s. In the background at 100 Hz, we found $\mu_{bck} = 4.0$ kPa and $\eta_{bck} = 0.5$ Pa·s. In the inclusion at 150 Hz, we measured $\mu_{inc} = 0.95$ kPa and $\eta_{inc} = 0.2$ Pa s, and in the background at 150 Hz we have $\mu_{bck} = 4.4$ kPa and $\eta_{bck} = 0.5$ Pa·s. We assumed the density $\rho = 10^3$ kg/m^3 throughout the volumes.

During the experiments, the needle was vibrated for 2 s before data were recorded. This recording delay ensured that the transient responses were negligible. Thus the measured and simulated shear wave images describe the steady-state response at the same instant in time. Shear wave reflections from the outer boundary were not observed. Because the background is stiffer than the inclusion, we see that the shear wavelength is reduced in the inclusion region. Although the phase front is distorted, the wavelength in the background material distal to the inclusion is restored – an effect more obvious when the shear wavelength is smaller that the inclusion size. Clearly shear waves are attenuated more at higher frequencies. Note that we are displaying velocity images at a specific depth, $V_z(x, y, z_0, \omega_0)$; however, the z component of velocity was measured throughout the 3-D volume.

The FDTD solver assigns relative values to particle velocities in the shear wave simulations. Therefore we selected a single overall scale factor for the images in the right column of Fig. 6.2 to facilitate comparisons. Furthermore, we plotted in Fig. 6.3 the vertical lines of 100 Hz velocity data through the inclusions of Figs. 6.2(b) and (c) at $y = 20$ mm.

Overall the measured and simulated data agree well. However there is evidence that the non-slip condition at the inclusion surface assumed in the simulation was violated experimentally. We found the surfaces were very weakly bonded because of the use of mold release during construction.

Applying the AHI algorithm to the measured and simulated 3-D velocity estimates, we reconstructed μ and η images at 100 Hz and 150 Hz. We summarize results only for the elastic shear modulus μ at 150 Hz. Results generated from measured experimental velocities are shown in Fig. 6.4 and those from simulated velocities in Fig. 6.5. In both figures, the top row of images are from the x, y plane of Fig. 6.2 (short-axis view), and the bottom row of images are from the orthogonal x, z plane near the center of the cylindrical inclusion (long-axis view). Elastic modulus values in both figures

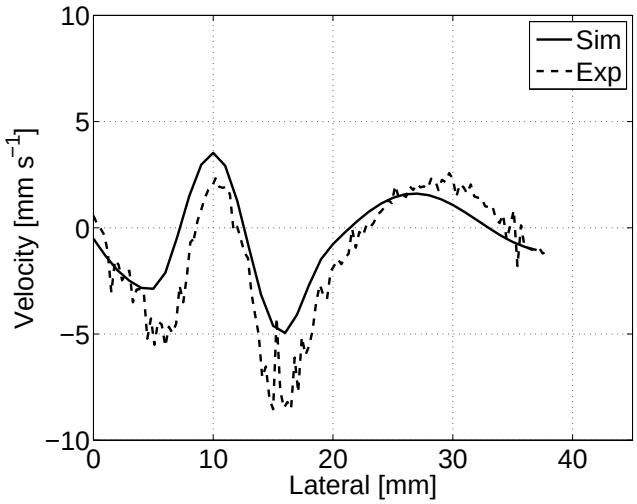

Figure 6.3: Lateral cut through the inclusion center for both experimental and simulation data for shear wave excitation at 100 Hz. Slight differences are attributed to the stronger reflections within the inclusion in experimental data due to the boundary conditions.

have the same scale.

The two levels of spatial filtering applied in the AHI algorithm clearly reduce spatial resolution. Notice the gray band surrounding the inclusion in every view. The differences are particularly clear between Fig. 6.5(a), elastic modulus map input into the shear wave simulator, and Fig. 6.5(b), the elastic modulus reconstructed from those simulated shear waves.

Figure 6.4 shows there is good spatial registration between the C-scan and μ images. The C-scan inclusion echogenicity contrast is from differences in scatterer number density and μ-image stiffness contrast is due to different gelatin concentrations. The appearance of the inclusion in cross section is consistent for μ images generated from 2-D and 3-D velocity data. However the appearance of the inclusion in long-axis view is distorted when 2-D velocity data, $V_z(x, z, \omega_0)$, are used. The appearance of the inclusion in long axis is not distorted for 3-D velocity data, $V_z(x, y, z, \omega_0)$, and these observations hold for both the experimentally acquired and the simulated velocity data. In Fig 6.6 we present a volume rendering of the reconstructed 3-D elastic shear modulus.

Using 2-D velocity data, we have no information about $\partial^2 v_z/\partial y^2$ in Eq. 6.7. Setting this derivative to zero ignores the flow of mechanical energy through the image plane. In the presence of strong out-of-plane energy fluxes, as for

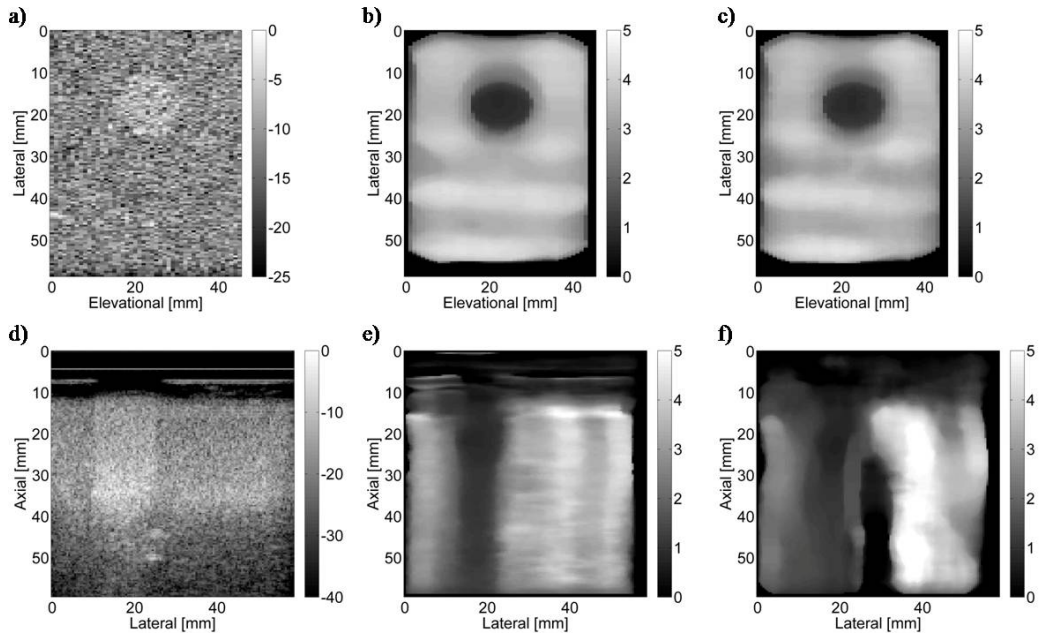

Figure 6.4: Algebraic Helmholtz Inversion (AHI) reconstructions of elastic shear modulus μ [kPa] from experimental velocity data obtained from a gelatin phantom at 150 Hz. Image (a) is an ultrasonic C-scan image at the same depth as the $\mu(x, y)$ images shown in (b) and (c). The B-scan in (d) is registered to the $\mu(x, z)$ images in (e) and (f). Images (b) and (e) are reconstructed from v_z data acquired in three dimensions, while images in (c) and (f) are from 2-D v_z data acquired in the plane of the image.

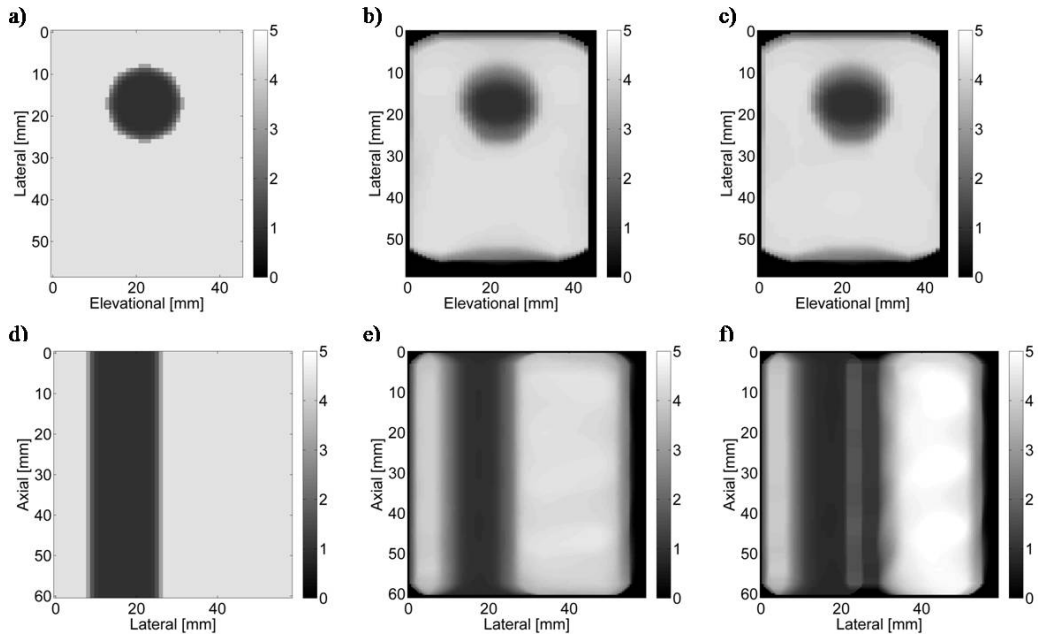

Figure 6.5: AHI reconstructions of elastic shear modulus μ [kPa] from simulated velocity data at 150 Hz. Images (a) and (d) show the modulus image input into the 3-D FDTD solver, and images (b), (c), (e), (f) correspond to those of the experiment shown in Fig. 6.4.

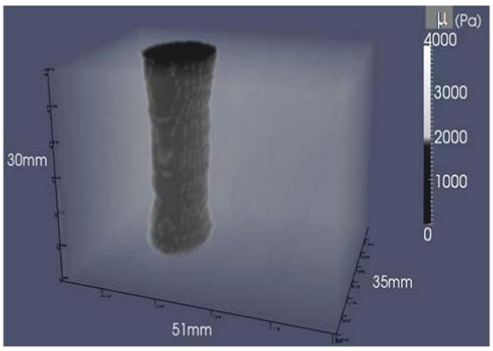

Figure 6.6: Volume rendering of 3-D reconstructed elastic modulus from 150 Hz experimental data set.

the long-axis view, artifacts are generated. In the short-axis view, however, energy flow is almost entirely in the image plane because object properties change negligibly along the y axis. Images of the dynamic viscous coefficient η were very noisy for experimentally acquired and simulated data in 2-D or 3-D.

6.4 Discussion

An advantage of using phantoms to develop imaging techniques is that the internal geometry and constituent component properties are generally known. Unfortunately, the low dynamic viscosity of gelatin, as compared with the estimation noise, means that gelatin, as we prepare it, is not a reliable medium for testing the fidelity of the AHI algorithm for reconstructing η. Other investigators reported similar troubling results for the viscous constant [105]. Since the difficulty lies in calculating Laplacians in noisy measurements, one solution is to test the algorithm in a more dispersive medium such as liver tissue.

We applied the 3-D FDTD solver, now experimentally validated in phantoms, to the same phantom geometry but with liver-like material properties to further investigate AHI performance. Previous measurements by our lab (Chapter 5) and others [18] showed liver to be more dispersive and therefore of substantially higher dynamic viscosity than gelatin gels. At the same time, μ for the two media are comparable. Measurements in fresh porcine liver gave an elastic modulus $\mu = 2.2$ kPa and dynamic shear viscosity $\eta = 1.8$ Pa·s. We also measured the properties of thermally damaged porcine liver and found $\mu = 5.0$ kPa and $\eta = 5.8$ Pa·s. Using fresh liver values to represent the background material and thermally-damaged liver for the inclusion, we simulated 150 Hz shear waves propagating through a "liver phantom". The results are presented in Fig. 6.7.

Reconstructed values of μ and η in the short-axis views of Fig. 6.7(b) and (c) are within 10% of the values input into the shear-wave simulator. However, the inclusion shape is distorted in both images. The degree of distortion increases with η. The inclusion appears to be shorted in the direction of wave propagation for both images, and shifted away from the incoming wave for μ images and toward the incoming wave for η images. Combining the two

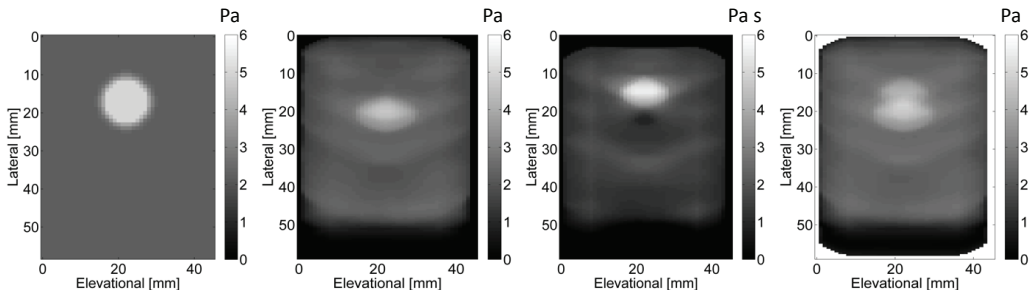

Figure 6.7: AHI reconstructions from simulated shear-wave particle velocity data of liver containing a thermal lesion. The magnitude of the complex shear modulus input into the FDTD solver is shown in (a). Background properties of the region are taken from measurements on fresh porcine liver, while properties for the bright target area are from stiff, thermally-damaged liver. Shown are an elastic shear modulus μ image in (b) and a dynamic shear viscosity η image in (c) resulting from reconstructing a shear-wave simulation. (d) is given by combining images in (b) and (c) to form the magnitude of the estimated complex shear modulus, $\sqrt{\mu^2 + \omega^2\eta^2}$.

images using $(\mu^2+\omega^2\eta^2)^{1/2}$, we can recover the general shape of the inclusion, as in Fig. 6.7d), regardless of the wavelength or viscosity.

Although the phase gradient method for estimating complex modulus values suffers from biases induced by medium heterogeneities [20], they appear to be more sensitive to low values of dynamic viscosity, even at low shear-wave frequencies, when those results are compared to the results from AHI algorithm.

Recently in the literature, several authors have addressed the effects of coupling between shear and pressure waves [112]. These studies were conducted using a Green's function approach and the assumption of acoustic radiation force excitation. In our simulations and experiments, we can safely ignore pressure wave propagation because very little is generated by the vibrating needle except near its tip. One reason for choosing the needle over a radiation force stimulus is to lower the computational complexity by ignoring compressional waves.

In classical computational fluid dynamics, the stability condition requires $c\Delta t/\Delta x < 1$, where c represents the velocity of the fastest wave in the simulation domain and Δt and Δx are the temporal and spatial sampling intervals. We would have to decrease Δt in the simulator by three orders of magni-

tude to avoid undersampling the compressional waves in time, and reduce Δx similarly in all three spatial dimensions to avoid spatial aliasing. These reductions increase the computational load by many orders of magnitude. Although we neglected coupling between compressional and shear waves, we have not observed any consequences as a result. We showed [20] that the needle generates waves that can be modeled as cylindrically diverging with enough accuracy to solve the wave equation for that geometry and therefore apply analytical expressions to the phase gradient estimation of the complex modulus. Needle vibration opens up the possibility of more general model-based reconstructions of the complex modulus that can reduce image noise significantly when compared with direct inversion approaches. With noise reduction comes improved spatial resolution as the need for spatial filtering is reduced. The needle is an invasive technique, and therefore most appropriate for basic science investigations.

6.5 Conclusions

This chapter presents a developed and implemented finite-difference time-domain technique for simulating shear waves in heterogeneous 3-D viscoelastic media. The simulator is straightforward to code and generates 3-D shear waves in time within a few days of processing on a desktop workstation, but it is representative of experimental results only when minimal compressional wave energy is present. The simulator was validated experimentally using a cylindrical source of shear waves. A comparison is presented of simulated particle velocity fields in heterogeneous phantoms of known properties with experimental estimates of the spatial wavelength, amplitude attenuation and refraction patterns. The results were found to be in good qualitative agreement.

The simulator was then used to study the accuracy of the algebraic Helmholtz inversion algorithm. The images of complex modulus constants can be distorted in patterns that depend on the shear wavelength and the amount of dispersion in the medium. These distortions were minimized simply by imaging the magnitude of the complex shear modulus. To avoid additional artifacts it is essential to measure velocity components in all three spatial dimensions for which medium heterogeneities have significant curvature. How-

ever it is sufficient to make measurements in just three adjacent scan planes when estimating the Laplacian from the AHI algorithm. Sufficient data may be obtained by translating the aperture in elevation either mechanically or electronically, e.g., using a 1.25D array. Alternatives include model-based reconstruction methods (Chapter 7) where the shear field is known analytically and therefore the wave equation can be solved in closed form. The vibrating needle generates nearly cylindrical waves that can provide the missing velocity information needed to avoid artifacts.

The conducted study of the influence of viscosity on shear wave propagation in heterogeneous materials provided further evidence of the added value of information in viscosity reconstruction. By reconstructing complex shear modulus we were able to spatially register highly viscous inclusion and to avoid artifacts that one might encounter when reconstructing only elastic modulus.

This type of artifact would not appear if a phase gradient method for the reconstruction of the shear wave speed were used. The reason for this is that the shear wave speed already contains viscoelastic information, so the image of the inclusion based on the shear wave speed reconstruction would be properly registered. Nevertheless, due to boundaries within the inclusion, the reconstructed shear wave velocity would be biased.

Work presented in this chapter brought several aspects of this dissertation to our attention regarding proposed methods for shear wave imaging. First of all, wave propagation is a 3D phenomenon; any reconstruction from 2D acquired fields without proper correction for the out-of-field component will be biased and prone to artifacts in the reconstructed images of the complex shear modulus. This conclusion applies for algebraic reconstruction methods. With the phase gradient method, by estimating the shear wave speed, we can reconstruct localized material properties that are unbiased and without artifacts for 2D case if material is homogeneous. On the other hand, in the presence of the inclusions and reflections from boundaries the phase gradient method will be biased and artifacts would be produced in the reconstructed images. Algebraic reconstruction can resolve material properties in the presence of reflections from the boundaries because it inverts the wave equation. Depending on the application and based on these engineering tradeoffs, one can decide on the best suited method for his needs.

In the next chapter a different method is pursued. The idea is to use 2D

particle velocity fields for the reconstruction of the material properties because such approach is practical and common in ultrasound imaging. Moreover, *a priori* knowledge of the wave dynamics is used to our advantage when estimating complex shear modulus. In the next chapter a model based Bayesian approach to reconstruction of complex shear modulus is presented.

CHAPTER 7

MODEL-BASED COMPLEX SHEAR MODULUS RECONSTRUCTION: A BAYESIAN APPROACH

7.1 Introduction

In previous chapters, important experimental results were obtained with methods for complex shear modulus estimation. In particular, statistically significant differences between fresh and thermally damaged tissues were observed. In spite of their usefulness, the studied methods, i.e., phase gradient and algebraic inversion methods, suffer from practical limitations. First, neither one of these two methods is suitable for online implementation. Second, the phase gradient method required fitting to a shear wave dispersion equation where data had to be available at several frequencies, although 1D and 2D data could be used. In contrast, direct algebraic inversion required 3D data, although data at one frequency was sufficient for shear modulus estimation. Therefore, there is a need to develop inversion methods that are more suitable for online implementation while combining some of the advantages of the algorithms explored in Chapters 4-6, i.e., ability to both properly handle 1D, 2D data and obtain inversions with single frequency data. In this chapter, an approach to complex shear modulus reconstruction is introduced that can circumvent a few of the drawbacks of methods studied in Chapters 4-6. The method is described for obtaining quantitatively accurate estimates of the complex shear modulus from a harmonic source at individual frequencies using 1-D spatial information.

The proposed method is based on a Bayesian approach, where material parameters are assumed to be random variables whose particular realization must be estimated [113]. This approach departs from the one followed in Chapters 3-6 where the underlying material properties were assumed to be

This chapter 7 is an extended version of M. Orescanin and M. F. Insana, "Bayesian reconstruction of complex shear modulus images," *Proc. IEEE International Ultrasonics Symposium*, San Diego, October 2010.

deterministic but unknown constants. The reasoning behind the proposed Bayesian approach is that knowledge about tissue parameters, if available, can be integrated in the estimator in order to improve estimation accuracy [113]. This method requires an assumption that parameters being estimated are random variables with prior probability density function (pdf).

In the case of shear wave imaging, like in many other applications, an approximate dynamical model with uncertain estimates of initial and boundary conditions is available. In addition, we have measurements of the model solution collected at different spatial and temporal locations depending on the engineering properties of our imaging system. The inverse problem to address in the proposed approach is the calculation of the pdf of the model solution conditioned on the measured observations. More often this approach is referred to as data assimilation [114]. We describe a new technique based on spatiotemporal nonlinear stochastic filtering of Doppler-detected particle velocities. Parameters derived from a maximum a posteriori (MAP) estimate of particle velocities are regularized by a dynamic wave propagation model to quickly obtain low-noise estimates of complex shear modulus parameters.

In the field of elasticity imaging several researchers used stochastic filtering for the reconstruction of underlying material properties. Zheng et al. [115] implemented a linear Kalman filter for the reconstruction of the harmonic motion of particle velocities at distinct spatial locations. Their approach is to model displacement at the spatial point of interest as a sinusoidal function of time. From estimated quantities, absolute phase at a distinct spatial location can be found. By repeating the same procedure for another location a phase difference is found similar to the method proposed in Chapter 4. Shear wave speed and shear wave dispersion curves are estimated over a frequency bandwidth and, via a fit, material properties are obtained. The stochastic filtering approach helped the authors to obtain optimal estimates of the temporal phase at the given spatial location from available IQ data, but their approach to material properties estimation is similar to the one proposed in Chapter 4. A drawback of this method is that, although optimal estimates of the particle velocities are provided, reconstruction of complex shear modulus is not optimal and is a post-processing procedure requiring several shear wave frequency measurements.

For thin tissue constructs, the modulus reconstruction of Liu and Ebbini [116] proposed a second-order dynamical model similar to the one presented

in Chapter 3. Their approach was to displace a tissue construct at the distinct spatial location by using acoustic radiation force. They track tissue displacement and use an extended Kalman filter (EKF) approach to reconstruct material properties at the given location. The EKF approach is necessary since the dynamical model used is a non-linear function of the underlying material parameters. Scanning samples in the raster manner, they form images of the underlying material properties. Similarly to Zheng, their approach is limited to single spatial location during filtering. A drawback of the Liu and Ebbini [116] method is that the force magnitude needs to be known for the calculations.

The above mentioned approaches can be classified as temporal reconstructions [117] of the underlying parameters using stochastic filtering. A different approach was taken by Tada et al. [118] for the material properties reconstruction during indentation tests. Instead of reconstructing material properties from dynamics of a single spatial point, they used an FEM simulator to link the field of the spatial points and their dynamics during indentation procedure. Observations of the material displacement over time are obtained using MRE. Material properties are reconstructed using an EKF to obtain low variance estimates.

In this dissertation, we favor the latter approach, where spatial area, not just one point, is evolved over time. We call this the spatiotemporal approach [117], where the spatial solution of the shear wave equation evolves over time. This approach is common in more mature fields such as geophysical sciences [114]. Comparing the spatiotemporal approach to the temporal approach of Zheng et al. [115], material properties can be reconstructed from estimated particle velocities per frequency in real-time.

The emphasis in this dissertation chapter is not on developing a new stochastic filtering framework for data assimilation. Rather, the intention is to adapt a well-developed method and study the feasibility of the data assimilation approach for the complex shear modulus reconstruction. This chapter is organized as follows. Section 7.2 provides a background on the stochastic filtering needed for understanding the Bayesian approach taken and the results in this chapter. This brief introduction to stochastic filtering is followed in Section 7.3 by details of the adapted approach. Specifically, the system model equation is derived; a joint parameter and state estimation problem is formulated via augmented state representation; and details

of the adapted stochastic ensemble filter, the maximum liklehood ensemble filter (MLEF) [119], are explained. Furthermore, our version of an ultrasonic Doppler simulator capable of simulating realistic moments of particle velocities based on the imaging parameters is outlined. In Section 7.4, numerical and experimental results are presented. Finally, in Section 7.5 concluding remarks are provided.

7.2 Background

A model-based processor is formulated on the analytical solution to the cylindrical shear wave equation. A Bayesian MAP solution for the resulting time-variable wave system and the processor is shown to be a recursive solution that can be solved using stochastic filtering techniques. In this chapter, the focus is on the practical application of the stochastic filtering; specifically, the discrete stochastic filtering problem is addressed. The discrete stochastic filtering problem is a dynamic system that can assume the following form:

$$\mathbf{x}_k = \mathcal{M}(\mathbf{x}_{k-1}), \quad k = 0, 1, \ldots \tag{7.1}$$

$$\mathbf{y}_k = \mathcal{H}(\mathbf{x}_k) + \boldsymbol{\epsilon}_k, \quad k = 0, 1, \ldots \tag{7.2}$$

where k is the discrete time index, $\mathbf{x}_k$ is the N dimensional state vector, $\mathcal{M}$ is the deterministic, possibly non-linear, mapping function, $\mathbf{y}_k$ is the observation vector, $\mathcal{H}$ is the deterministic (observation operator), possibly non-linear, mapping function of $\mathbf{x}_k$, and $\boldsymbol{\epsilon}_k$ is an independent observation noise sequence.

Equation 7.1 is the state equation or the system model equation. Physical processes subject to random disturbances, whose state can be represented as a finite-dimensional vector, can be modeled via a vector difference equation [120]. Equation 7.2 is the observation operator equation. The Bayesian approach suggests that we calculate density $p(\mathbf{x}_k|\mathbf{y}_k)$, also called *a posteriori* pdf, which encapsulates the information on the state vector, $\mathbf{x}_k$, that is contained in the observations $\mathbf{y}_k$ and the prior distribution of $\mathbf{x}_k$ [113].

According to Bayes theorem, the posterior pdf follows from the relation

$$p(\mathbf{x}|\mathbf{y}) \propto p(\mathbf{y}|\mathbf{x})p(\mathbf{x}). \tag{7.3}$$

In the MAP estimation approach, we chose $\hat{\mathbf{x}}$ to maximize the posterior pdf or $\hat{\mathbf{x}} = \arg\max_x p(\mathbf{x}|\mathbf{y})$ [113]. Hence, the MAP estimator is $\hat{\mathbf{x}} = \arg\max_x p(\mathbf{y}|\mathbf{x})p(\mathbf{x})$. In this thesis, several assumptions are made regarding the pdf's of the processes of interest. We model pdf's as Gaussian [121, 122]. Specifically, for generality we drop time index k. Therefore, the error marginal density $p(\mathbf{x})$ is given with the error distribution $\boldsymbol{\epsilon}_f = (\mathbf{x}^f - \mathbf{x}) \sim \mathcal{N}(0, \mathbf{P}_f)$

$$p(\mathbf{x}) = \frac{1}{(2\pi)^{N/2}|\mathbf{P}_f|^{\frac{1}{2}}} \exp\left(-\frac{1}{2}(\mathbf{x} - \mathbf{x}^f)^T \mathbf{P}_f^{-1}(\mathbf{x} - \mathbf{x}^f)\right), \tag{7.4}$$

where $\mathbf{x}^f$ is the predicted state value, $\mathbf{P}_f$ is predicted covariance (positive-definite matrix), and $|\mathbf{P}_f|$ is the determinant of $\mathbf{P}_f$. The conditional mean, $\mathbf{x}^f$, and the covariance $\mathbf{P}_f$ are obtained via the model state equation evolution of the prior mean and the covariance. The likelihood pdf, or the observation error conditional pdf, is assumed to be Gaussian with $\boldsymbol{\epsilon}_r = (\mathbf{y} - \mathcal{H}(\mathbf{x}^f)) \sim \mathcal{N}(0, \mathbf{R})$ [114]

$$p(\mathbf{y}|\mathbf{x}) = \frac{1}{(2\pi)^{N/2}|\mathbf{R}|^{\frac{1}{2}}} \exp\left(-\frac{1}{2}(\mathbf{y} - \mathcal{H}(\mathbf{x}))^T \mathbf{R}^{-1}(\mathbf{y} - \mathcal{H}(\mathbf{x}))\right), \tag{7.5}$$

where $\mathbf{R}$ is positive-definite matrix and $|\mathbf{R}|$ is the determinant of $\mathbf{R}$.

With help from Eqs. 7.4 and 7.5, Eq. 7.3 can be written as

$$\begin{aligned} p(\mathbf{x}|\mathbf{y}) \propto \quad & \frac{1}{(2\pi)^{N/2}|\mathbf{P}_f|^{\frac{1}{2}}} \exp\left(-\frac{1}{2}(\mathbf{x} - \mathbf{x}^f)^T \mathbf{P}_f^{-1}(\mathbf{x} - \mathbf{x}^f)\right) \\ & \times \frac{1}{(2\pi)^{N/2}|\mathbf{R}|^{\frac{1}{2}}} \exp\left(-\frac{1}{2}(\mathbf{y} - \mathcal{H}(\mathbf{x}))^T \mathbf{R}^{-1}(\mathbf{y} - \mathcal{H}(\mathbf{x}))\right). \end{aligned} \tag{7.6}$$

Equivalent to maximizing the *a posteriori* probability, we can take the logarithm of Eq. 7.6, $\ln p(\mathbf{x}|\mathbf{y})$, and minimize the cost function $\mathcal{J}$[121, 122]:

$$\mathcal{J}(x) \;=\; \frac{1}{2}(\mathbf{x} - \mathbf{x}^f)^T \mathbf{P}_f^{-1}(\mathbf{x} - \mathbf{x}^f) + \frac{1}{2}(\mathbf{y} - \mathcal{H}(\mathbf{x}))^T \mathbf{R}^{-1}(\mathbf{y} - \mathcal{H}(\mathbf{x})). \tag{7.7}$$

The least square solution $\mathbf{x}^a = x_{opt}$, that gives minimum $\mathcal{J}$, also yields the maximum for $p(\mathbf{x}|\mathbf{y})$, hence it is the maximum liklehood estimate. A detailed derivation of the cost function can be found in books by Evensen [114] and Van Der Heijden [122]. The optimal $\mathbf{x}$ can be determined using iterative

unconstrained minimization methods.

In this dissertation, for the task of minimizing the cost function defined by Eq. 7.7, we adapt a Maximum Liklehood Ensemble Filter (MLEF) [119]. MLEF is a stochastic filter capable of handling nonlinear dynamical models and nonlinear observation operators. More details about this specific stochastic filter and its adaptation are provided in the next section.

7.3 Methods

A mechanical actuator harmonically drives a stainless steel needle placed in the medium to generate narrow-band cylindrical shear waves. Shear waves are imaged in a radial plane using a multi-lag phase estimator, which leverages the narrow-band wave feature to extend standard pulse-pair (lag-one) processing for reduced velocity variance (Chapter 4). By applying a vibrating-needle source, we can model shear wave dynamics as the solution to the Helmholtz equation with a cylindrical geometry. A well-defined source geometry provides exclusively cylindrical shear wave propagation from the source, except in the region around the needle tip. Strong coupling between the source vibration energy and the propagating shear wave results in large particle displacement amplitudes along the path of propagation. This cylindrical wave model is applied in developing a prediction filter used to model the nonlinear relationship between wave dynamics and material parameters. Consequently, we adapted a Maximum Likelihood Ensemble Filter (MLEF) [119] for this estimation. The feasibility of this technique is demonstrated via simulations with realistic imaging parameters and from ultrasonic measurements of mechanical properties in tissue-like hydrogels. Details of the experimental setup are found in Chapter 4.

7.3.1 System Model Equation

In Chapter 4, narrow-band cylindrical shear waves excited by a harmonically driven needle were studied. It was shown that spatiotemporal shear wave dynamics can be accurately modeled with an analytical expression for

cylindrical shear wave propagation along the radial axis,

$$v(r,t) = \frac{1}{\sqrt{r}} A e^{-\alpha r} \cos(\omega t - k_s r) \ , \tag{7.8}$$

where v is the particle velocity, r is the radial distance from the needle in the plane, t is the time, A is the magnitude of the wave at the source location, α is the absorption or imaginary part of the complex shear wave number, and k_s is the real part of the complex shear wave number at angular shear frequency ω. Validity of the proposed model was verified via comparison with experimentally acquired data as illustrated in Fig. 4.3. Equation 7.8 needs to be transformed into a difference system model equation to be used within the theoretical framework discussed in Section 7.2.

In the following equations, we derive the generalized difference form of Eq. 7.8. We start with a generalized version of Eq. 7.8 given by

$$v_k = \frac{1}{\sqrt{r - r_0}} A e^{-\alpha(r-r_0)} \cos(\omega k \triangle t - k_s(r - r_0) - \phi) \ , \tag{7.9}$$

where index k denotes discrete time, r_0 is the initial distance from the source, $\triangle t$ denotes discrete time step and ϕ represents initial temporal phase. Equation 7.9 can be represented as a function of previous time step,

$$\begin{aligned} v_k &= \frac{1}{\sqrt{r - r_0}} A e^{-\alpha(r-r_0)} \cos(\omega(k - 1 + 1)\triangle t - k_s(r - r_0) - \phi) \\ &= \frac{1}{\sqrt{r - r_0}} A e^{-\alpha(r-r_0)} \cos((\omega(k - 1)\triangle t - k_s(r - r_0) - \phi) - \omega \triangle t) \ . \end{aligned} \tag{7.10}$$

Using the trigonometric identity,

$$\cos(\varphi - \theta) = \cos(\varphi)\cos(\theta) - \sin(\varphi)\sin(\theta) \ , \tag{7.11}$$

one can derive from Eq. 7.10

$$\begin{aligned} v_k = \frac{1}{\sqrt{r - r_0}} A e^{-\alpha(r-r_0)} [&\cos(\omega(k - 1)\triangle t - k_s(r - r_0) - \phi)\cos(\omega \triangle t) \\ &- \sin(\omega(k - 1)\triangle t - k_s(r - r_0) - \phi)\sin(\omega \triangle t)] \ . \end{aligned} \tag{7.12}$$

Following the definition in Eq. 7.9

$$v_{k-1} = \frac{1}{\sqrt{r - r_0}} A e^{-\alpha(r-r_0)} \cos(\omega(k-1)\triangle t - k_s(r - r_0) - \phi) \ . \tag{7.13}$$

From Eq. 7.12 and Eq. 7.13 it follows that

$$\begin{aligned} v_k = v_{k-1} \cos(\omega \triangle t) - \frac{1}{\sqrt{r - r_0}} A e^{-\alpha(r-r_0)} \\ \times \sin(\omega(k-1)\triangle t - k_s(r - r_0) - \phi) \sin(\omega \triangle t) \ . \end{aligned} \tag{7.14}$$

This model allows for appropriate initialization of the forward model that is capable of predicting spatiotemporal cylindrical shear wave dynamics in a recursive manner. Equivalently, model state equation Eq. 7.14 takes the form

$$\mathbf{v}_k = \mathcal{M}(\mathbf{v}_{k-1}; \boldsymbol{\theta}) \ , \quad \boldsymbol{\theta} = [r_0 \ \phi \ A \ \alpha \ k_s]^T \tag{7.15}$$

where $\mathcal{M}$ is the nonlinear forward model assuming that the parameter vector $\boldsymbol{\theta}$ represents unknown variables assumed spatially constant, i.e., $\nabla \boldsymbol{\theta} = 0$. If the parameter vector represents known constants, the derived model would be considered linear with respect to particle velocities.

7.3.2 Observation Model Equation

In general the observational equation is a nonlinear function of the state vector, characterized by the nonlinear operator $\mathcal{H}$, Eq. 7.2. Operator $\mathcal{H}$ models the transfer function between the true underlying particle motion, $\mathbf{v}$, and estimated particle velocities, $\hat{\mathbf{v}}$. Ultrasound systems do not detect particle velocities directly; rather, a change in the phase shift between two received pulses is estimated and velocity estimate is formed using this information (see Chapter 4). In practice, ultrasound systems can be modeled using linear systems theory. One can find linear observation operator $\mathbf{H}$ for the given system at hand to model US Doppler detection. With the assumption that all particles within imaging pulse volume move with constant velocity $\mathbf{v}$, estimated velocity within the pulse volume for this case corresponds to the averaged value of the velocity within the pulse volume. Hence, estimated velocity is given with $\hat{\mathbf{v}} = \mathcal{H}(\mathbf{v}) = \frac{1}{N} \sum_{i=1}^{N} \mathbf{v}_i = \mathbf{v}$, where N is the number of

particles. Number of particles is a scaling constant that affects imaging SNR and does not affect estimated velocity within the pulse volume. Under these conditions, $\mathcal{H} = \mathbf{H} = \mathbf{I}$ (ideal Doppler imaging system), the observation equation, Eq. 7.2, becomes

$$\hat{\mathbf{v}}_k = \mathbf{I}\mathbf{v}_k + \boldsymbol{\epsilon}_k \ , \quad k = 0, 1, \ldots \tag{7.16}$$

The noise term varies by application; it is directly related to the variance of Doppler velocity estimates. The variance of Doppler velocity estimates depends on several engineering parameters of the system and the magnitude of the particle velocity. More details are provided in the Section 7.3.5. Noise is modeled as Gaussian, $\boldsymbol{\epsilon} = \mathcal{N}(0, \mathbf{R})$, where $\mathbf{R}$ is a diagonal covariance matrix.

7.3.3 Augmented State-Space Representation

The joint state and parameter estimation problem is treated as an augmented state estimation problem for the nonlinear model equation represented by [120, 123, 114],

$$\mathbf{x}_k = \begin{bmatrix} \mathbf{v}_k \\ \boldsymbol{\theta}_k \end{bmatrix} = \begin{bmatrix} \mathcal{M}\left(\mathbf{v}_{k-1}; \boldsymbol{\theta}_{k-1}\right) \\ \boldsymbol{\theta}_{k-1} \end{bmatrix} \ , \tag{7.17}$$

where $\mathbf{v}$ is the vector of radial particle velocities and $\mathcal{M}$ is the nonlinear forward operator, both defined by Eq. 7.14. In Eq. 7.17, the state vector of radial particle velocities is augmented with the vector of the unknown parameters. The relationship between $\boldsymbol{\theta}_k$ and $\boldsymbol{\theta}_{k-1}$ was obtained assuming material parameters to be constant during the data acquisition time; i.e., $\dot{\boldsymbol{\theta}} = 0$. This is a sound assumption since data acquisition occurs over a time frame of one hour. During that time and at the constant temperature, gelatin is not expected to change physical properties. For specific gelatin concentrations, the complex shear modulus change as a function of age is illustrated in Figs. 3.5 and 3.6.

Similarly, using Eq. 7.16, the augmented measurement equation gives the vector of velocity estimates $\hat{\mathbf{v}}$ as

$$\mathbf{y}_k = \begin{bmatrix} \hat{\mathbf{v}}_k \\ \mathbf{0} \end{bmatrix} = [\mathbf{I}\ \mathbf{0}] \begin{bmatrix} \mathbf{v}_k \\ \boldsymbol{\theta}_k \end{bmatrix} + \begin{bmatrix} \boldsymbol{\epsilon}_0 \\ 0 \end{bmatrix} \ . \tag{7.18}$$

The parameter vector $\boldsymbol{\theta}$ is not directly observable by the ultrasound system and is therefore zeroed in the observation model in Eq. 7.18. The joint state and parameter estimation problem can now be understood as a state estimation problem for the augmented nonlinear system given by Eqs. 7.17 and 7.18.

7.3.4 Maximum Likelihood Ensemble Filter (MLEF)

The augmented non-linear system formulation given by Eqs. 7.17 and 7.18 leads to a filtering problem solved using MLEF [119, 124]. MLEF estimates the state vector through the minimization $\hat{\mathbf{x}} = \arg\min_{x} \mathcal{J}(\mathbf{x})$. The computational steps of MLEF are similar to those of other stochastic filters that adopt a form of feedback control estimation. The filter predicts the process state at regular time points from a model with assumed parameters. It uses measurements to then correct the state vector for parameter inaccuracies. The equations fall in two general groups: a forecasting step that predicts the state of the system and an analysis step that makes corrections to the predicted state. In the forecasting step, the current state and error covariance matrix are projected forward in time to provide the *a priori* estimates for the next time step. The analysis step provides the feedback correction with *a posteriori* data information. Details about the derivation of the algorithm and minimization of the cost function can be found in [119] and [124].

The first step in MLEF filtering is the initialization of the state vector $\mathbf{x}^0 = [\mathbf{v}_0 \ \boldsymbol{\theta}_0]^T$ and the error square-root covariance matrix with

$$\mathbf{P}_0^{1/2} = [\mathbf{p}_1 \ \mathbf{p}_2 \ \cdots \ \mathbf{p}_s], \ \mathbf{p}_i = \begin{bmatrix} p_{1,i} \\ p_{2,i} \\ \vdots \\ p_{N,i} \end{bmatrix}, \tag{7.19}$$

where index N defines the dimension of the state vector and index S defines the number of ensembles. Generally, MLEF is a reduced rank filter, i.e., $S < N$, although it could be full rank.

The expressions for forecasting and analysis steps in MLEF filtering often imply time index k while explicitly indicating quantities determined through the forecasting process by subscript f and those from the analysis process

by subscript a. We outline the algorithm below

- *Forecast step*

  1) Project the state

$$\mathbf{x}^f = \begin{bmatrix} \mathbf{v}_f \\ \boldsymbol{\theta}_f \end{bmatrix} = \begin{bmatrix} \mathcal{M}\left(\mathbf{v}_a; \boldsymbol{\theta}_a\right) \\ \boldsymbol{\theta}_a \end{bmatrix}, \ \mathbf{x}^a = [\mathbf{v}_a \ \boldsymbol{\theta}_a]^T. \tag{7.20}$$

  2) Project the error covariance matrix

$$\begin{aligned} \mathbf{P}_f^{1/2} &= [\mathbf{b}_1 \ \mathbf{b}_2 \ \cdots \mathbf{b}_s], \\ \mathbf{b}_i &= \mathcal{M}(\mathbf{x}^a + \mathbf{p}_i^a) - \mathcal{M}(\mathbf{x}^a). \end{aligned} \tag{7.21}$$

- *Analysis step*

  3) Update state estimate

$$\begin{aligned} \mathbf{x}^a &= \mathbf{x}^f + \\ &\mathbf{P}_f^{1/2}[\mathbf{I} + \mathbf{Z}_f^T \mathbf{Z}_f]^{-1} \mathbf{Z}_f^T [\mathbf{R}^{-1/2}(\mathbf{y} - \mathcal{H}(\mathbf{x}^f))], \end{aligned} \tag{7.22}$$

  where $\mathbf{Z}_f$ is the observed perturbation matrix defined as

$$\begin{aligned} \mathbf{Z}_f &= [\mathbf{z}_1(\mathbf{x}^f) \ \mathbf{z}_2(\mathbf{x}^f) \ \cdots \ \mathbf{z}_s(\mathbf{x}^f)], \\ \mathbf{z}_i(\mathbf{x}^f) &= \mathbf{R}^{-1/2}[\mathcal{H}(\mathbf{x}^f + \mathbf{p}_i^f) - \mathcal{H}(\mathbf{x}^f)]. \end{aligned} \tag{7.23}$$

  4) Update error covariance matrix

$$\mathbf{P}_a^{1/2} = \mathbf{P}_f^{1/2}[\mathbf{I} + \mathbf{Z}_a^T \mathbf{Z}_a]^{-1/2}, \tag{7.24}$$

  where $\mathbf{Z}_a$ is the observed perturbation matrix defined as

$$\begin{aligned} \mathbf{Z}_a &= [\mathbf{z}_1(\mathbf{x}^a) \ \mathbf{z}_2(\mathbf{x}^a) \ \cdots \ \mathbf{z}_s(\mathbf{x}^a)], \\ \mathbf{z}_i(\mathbf{x}^a) &= \mathbf{R}^{-1/2}[\mathcal{H}(\mathbf{x}^a + \mathbf{p}_i^f) - \mathcal{H}(\mathbf{x}^a)]. \end{aligned} \tag{7.25}$$

  5) Repeat steps 1-4 when the new observation vector becomes available.

Following the form of a feedback controlled estimation, upon initialization, we first evolve in time the state vector and the covariance matrix (Forecast

step, Eqs. 7.20 and 7.21). This is our best guess of the state of the system in current time step without available measurement. When measurement for the current time step becomes available, we first calculate the observation perturbation matrix $\mathbf{Z}_f$ and update the state estimate (Analysis step, Eqs. 7.23 and 7.22). With the optimal state estimate for the current time step, $\mathbf{x}_a$, we calculate the observation perturbation matrix $\mathbf{Z}_a$, which we use to update the error covariance matrix $\mathbf{P}_a$ (Analysis step, Eqs. 7.25 and 7.24). In sequential manner we repeat Forecast steps and Analysis Steps whenever new measurement becomes available.

7.3.5 Simulation

One-dimensional random scattering fields were generated in MATLAB (The MathWorks, Inc., Natick, MA), using Monte Carlo methods, to facilitate simulation of RF echo Doppler pulses of a vibrating scattering medium. For the purposes of the model presented in this article, the scatterers are uniformly distributed within a volume and each has unity reflectivity. The mean number of scatterers positioned along the entire axis was selected to be greater than 20 per pulse length to ensure fully developed speckle conditions. The mean was introduced into a Poisson random number generator to select the actual number of identical point scatterers present for each Monte Carlo realization [125]. The scattering field was numerically generated so that the coordinate of each scatterer was preserved as a floating-point value. Scatterers were displaced by shear-wave energy based on the velocity within the resolution element as defined by Eq. 7.9.

Calculated displacements were used to reposition each scatterer in the scattering field to simulate vibration at the given shear frequency. The result was convolved with an ultrasonic linear time invariant impulse response of the system, given by the Gaussian modulated sinusoid

$$h(t) = e^{-t^2/2\sigma_t^2} \sin(2\pi f_c t) \ . \tag{7.26}$$

The carrier frequency of the pulsed transmission was $f_c = 6$ MHz, c = 1540 m/s, and σ_t is the pulse-duration parameter. The effective fractional bandwidth is given with $\mathrm{B}_{eff}/\mathrm{f_c} = 1/(2\mathrm{f_c}\sigma_t\sqrt{\pi})$ [125]. We considered pulse fractional bandwidth of $\mathrm{B}_{eff}/\mathrm{f_0} = 0.2$. White Gaussian noise was added to the

signal and the RF echo signal was decimated to give a vibration Doppler echo signal at 20 Msamples/s.

To verify the performance of the simulator, we compare simulated velocity variances with theoretically predicted velocity variances for a well-described case. To simplify the analysis, we assume that the particle velocity is constant throughout the resolution volume. This would correspond to steady flow velocity scenario. An expression for the variance of the velocity estimator from the correlated pulse pairs embedded in white Gaussian noise (WGN) is given by [57]

$$\begin{aligned}\sigma_{\hat{v}}^2 = & \frac{c^2}{32\pi^2 T_{\text{prf}} \varrho^2(T_{\text{prf}}) f_c^2 (M-1)} \times \Big\{ [1 - \varrho^2(T_{\text{prf}})] \\ & \sum_{k=-(M-2)}^{(M-2)} \varrho^2(kT_{\text{prf}}) \times ((M-1) - |k|) \\ & + \frac{1}{(M-1)SNR^2} + \frac{2}{(M-1)SNR} \\ & \times \left[1 + \varrho(2T_{\text{prf}})(\frac{1}{(M-1)} - 1) \right] \Big\} \end{aligned} \tag{7.27}$$

where $\varrho(kT_{\text{prf}}) = \frac{\hat{\phi}_k}{\hat{\phi}_0}$ is the magnitude of the normalized signal correlation (correlation coefficient). The expression defined by Eq. 7.27 is valid under the assumption of a large ensemble, M.

Doppler power spectrum can be modeled as Gaussian with spectrum width σ_{vD} at 6 dB [56]. Doppler spectrum width and spectral broadening depend on various parameters, such as length of the pulse, beam-characteristics, dispersion of velocity within the resolution volume, and vector velocity direction to name a few [56, 57, 126, 127]. Discussing statistical properties of the estimator with respect the normalized spectrum width, $\sigma_{vn} = \sigma_{vD}/2\upsilon_a$ [m s^{-1}], includes many combinations of these parameters that can be estimated for the specific experimental conditions. Equation 7.27 was experimentally verified in [88] in ultrasound detected flow of blood mimicking fluid. Assuming that velocity is constant over the ensemble time and the transit time effect is negligible, the width of the Doppler spectrum is

$$\sigma_{fD} = \frac{1}{\sqrt{2}2\pi\sigma_t} \frac{2\upsilon}{c} \; [Hz] \; . \tag{7.28}$$

Spectrum width in the velocity domain, σ_{vD}, is related to spectrum width in the frequency domain via $\sigma_{vD} = \sigma_{fD}\lambda/2$ [m s^{-1}]. From Eq. 7.28 it follows, that for the given pulse parameters, Doppler spectral broadening is directly proportional to the change in the velocity within the resolution volume. With increase in the spectrum width, for the given SNR ratio, correlation within the ensemble is decreasing, $\varrho(kT_{\text{prf}})$, and the variance of velocity increases. Doppler estimation benefits from the high ensemble correlation; however, with a decrease in SNR ratio, the variance of the velocity increases due to the small number of independent estimates within the ensemble due to the high correlation. We demonstrated this in the study based on the lag-one estimator approach (Chapter 4).

In Fig. 7.1, we present Eq. 7.27 for three values of normalized spectrum width σ_{vn} of 0.01, 0.02 and 0.047 m s^{-1} and large ensemble size of M = 128 pulses. The results are from the Monte Carlo simulation with 200 realizations of the uniform constant velocity shift within the resolution volume. Very good agreement exists between the analytical expression and the result of the simulation, thus verifying the statistical accuracy of the simulator.

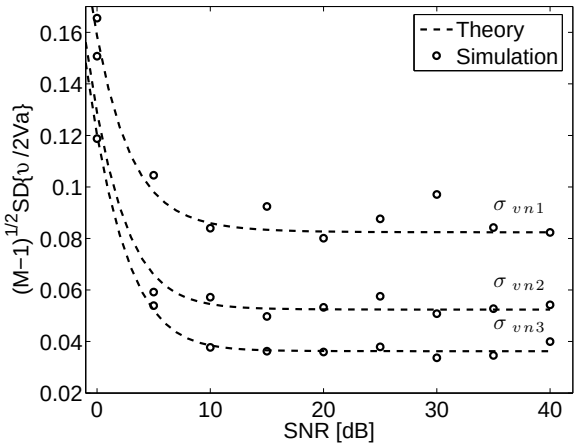

Figure 7.1: Standard deviation of mean Doppler velocity estimates, $\hat{v}$, vs. the SNR for three values of normalized spectrum width, $\sigma_{vn1} = 0.047$, $\sigma_{vn2} = 0.02$ and $\sigma_{vn3} = 0.01$ m s^{-1} and large ensemble size of M = 128. Dashed lines show theoretical predictions and *circles* show results from the simulations (200 realizations).

In order to verify the performance of the proposed MLEF filtering for the reconstruction of the complex shear modulus, several simulations were conducted. Simulation parameters were selected to match those measured during

imaging experiments where the assumption was made that within the imaging pulse length particle velocity is constant. This is a reasonable assumption for the cylindrical wave propagation in the homogeneous material since, axially, particles displace continuously in phase with the same velocity. This was verified experimentally in Chapter 6. The Doppler processing scheme follows the recommendation of Chapter 4 and is based on lag-k estimator with the same settings as in Chapters 4-6.

7.4 Results

The algorithm described above was tested by estimating the complex modulus from shear waves passing through a homogeneous block of 4%-concentration gelatin gel. The gelatin phantom is tested with three different excitation amplitudes to check for linearity. A mechanical actuator harmonically vibrates a 1.5-mm diameter needle at frequency values in the range of 50-450 Hz. We use data collected over 40 spatial locations sampled regularly on the interval 0.46 mm for a total length of 18.4 mm. We make an assumption that the first spatial location is immediately adjacent to the needle, and we allow that parameter to vary with r_0. The filter is initialized as follows. The first observation of particle velocity over the 18.4 mm length is assigned to $\mathbf{v}_0$. Parameter r_0 is assigned 0.3 mm with the error of 0.1 mm; phase correction constant ϕ and the amplitude A with the errors are estimated from the first period of the particle velocities at the first spatial position. Material parameters are assigned from measurements of gelatin [20], where $\alpha = 23$ Np m^{-1} and $k_s = 414$ m^{-1}, that are obtained assuming a K-V model for an elastic shear modulus of $\mu = 570$ Pa and shear dynamic viscosity of $\eta = 0.2$ Pa·s. We assumed that material parameters are known within a 20% error following the work presented in Chapters 3 and 4 and correspond to sample variability. The initial covariance matrix for the analysis error, Eq. 7.19, is defined using ensemble members initiated by randomly perturbing errors of the state vector, Eq. 7.19.

Under these conditions, we estimated the values of shear wavenumber and attenuation as a function of frequency that are shown in Fig. 7.2 and Fig. 7.3, respectively.

Measurements were acquired for actuator voltages of 5, 10, and 15 V that

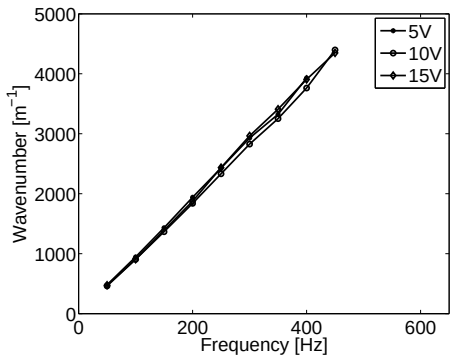

Figure 7.2: Estimated wavenumber of 4% gelatin gel as a function of shear wave frequency for three excitation voltages.

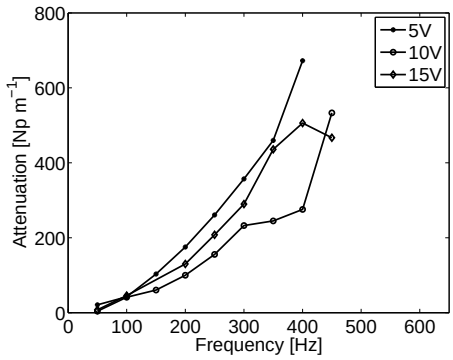

Figure 7.3: Estimated shear attenuation of 4% gelatin as a function of shear wave frequency for three excitation voltages.

provided proportional particle displacement amplitudes at the needle surface. From Doppler estimates of the shear waves, we estimated k_s and α at each source frequency. Agreement among estimates at the three applied strains confirms the assumption of linearity in gelatin between 50 and 450 Hz.

As an example of the MLEF performance in Figs. 7.4 and 7.5, convergence of the parameters, α and k_s, as a function of time steps is presented. Both parameters converge within 50 time steps where wavenumber converges within 1% of variation.

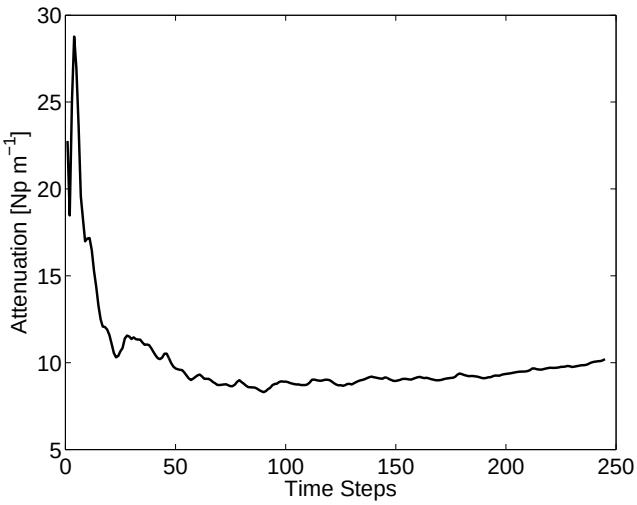

Figure 7.4: Convergence of the attenuation parameter α as a function of time steps for experimentally acquired data set at 50 Hz. For the given initialization filter converges within 50 time steps.

Since we are estimating parameters not only but particle velocities as well, in Fig. 7.6, the last estimate of state space is compared to the last observation. For particle velocities stochastic filtering is a denoising operation. Hence, the MLEF estimate of the state space is smooth compared to the observation data.

Particle velocities at distinct spatial locations as a function of time steps are compared for observational data and MLEF filtered data. Two locations, first at 4.6 mm from the source and second at 13.8 mm from the source, are illustrated in Figs. 7.7 and 7.8 respectively. At each of the spatial locations particle velocities are time harmonic functions with constant amplitude and at frequency of 50 Hz. Amplitude of the sinusoidal function closer to the source is larger because the wave is less attenuated. Also, in Fig. 7.8, variance of the sinusoidal signal is larger compared to the Fig. 7.8. The reason for this

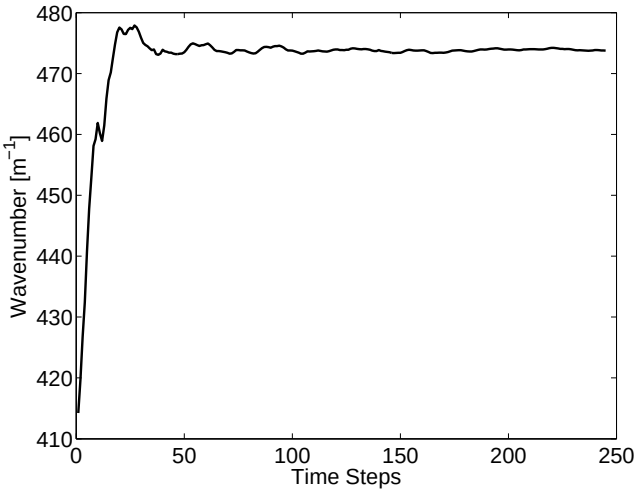

Figure 7.5: Convergence of the wavenumber parameter k_s as a function of time steps for experimentally acquired data set at 50 Hz. In the first 50 time steps of the filter, the parameter converges to be within 1% variation.

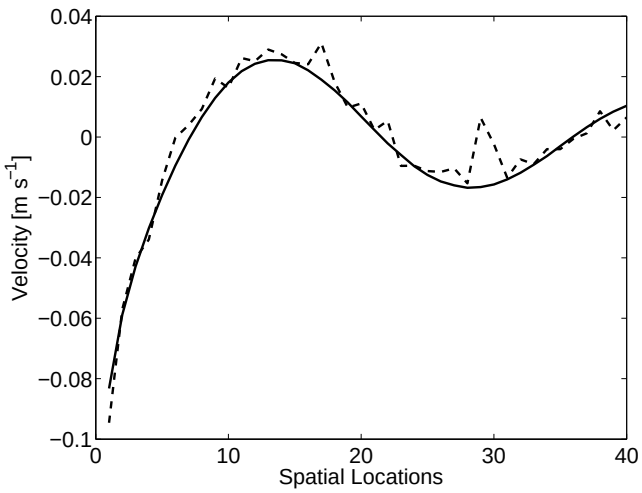

Figure 7.6: Doppler estimates of particle velocities are compared with those estimated by the MLEF filter as a function of space. Data are compared for the final time step. Doppler measurements are indicated by a dashed black line and MLEF tracking estimates by a solid black line.

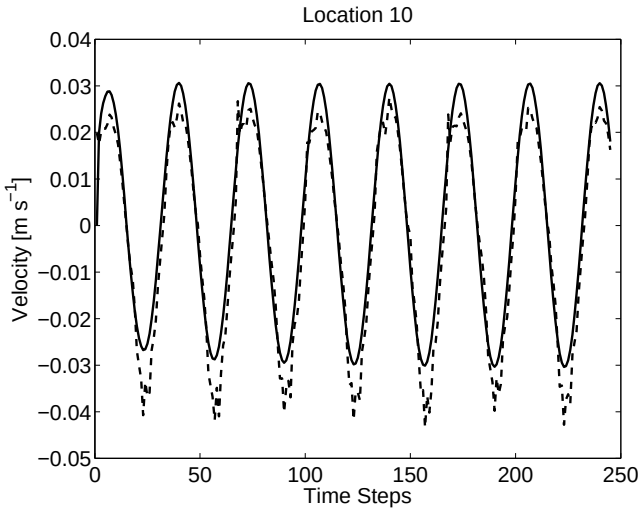

Figure 7.7: Doppler estimates of particle velocities are compared with those estimated by the MLEF filter as a function of time. Data are compared for distinct spatial location 4.6 mm from the source. Doppler measurements are indicated by a dashed black line and MLEF tracking estimates by a solid black line.

is that the shear wave is attenuated and for smaller magnitude of particle velocities variance of estimation increases.

In Chapter 4 we discussed two rheological models for modeling viscoelastic material properties of gelatin phantoms. First, we addressed Kelvin-Voigt model as a standard model used in complex shear modulus reconstruction. Second, we tested a standard solid body model, the Zener model. We compared the two based on the shear wave dispersion fitting. Results were inconclusive. Within the bandwidth of the measurement one model could not be favored over the other. We concluded in Chapter 4 that, due to the uncertainties in dispersion equation estimation, larger bandwidth of the measurements of up to 1 kHz would be needed to resolve the two models. Complex shear modulus constants are estimated from complex wave number

$$k^* = (\rho\omega^2/G^*)^{1/2} = k_s - i\alpha \ . \tag{7.29}$$

By applying standard relationships as found in [20], we tested whether the K-V or Zener model represented wave dynamics in gelatin by estimating the complex modulus constants, $G^* = G' - iG''$, where G' is the elastic storage modulus and G'' is the viscous loss modulus. The results are presented in

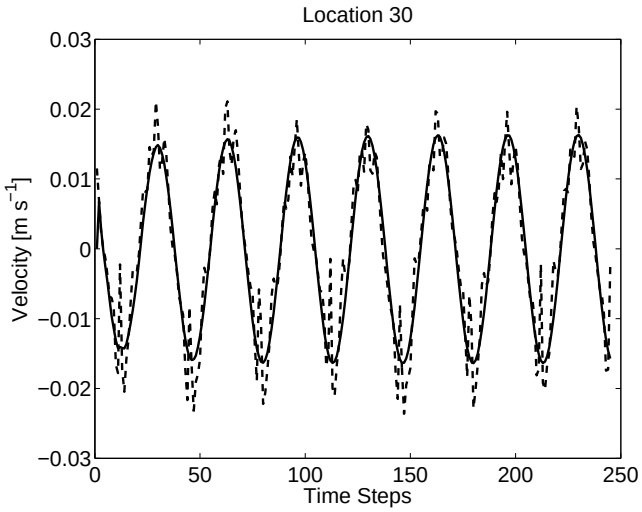

Figure 7.8: Doppler estimates of simulated particle velocities are compared with those estimated by the MLEF filter as a function of time. Data are compared for distinct spatial location 13.8 mm from the source. Doppler measurements are indicated by a dashed black line and MLEF tracking estimates by a solid black line.

Fig. 7.9.

For weakly viscous media such as gelatin gels the storage modulus is expected to be much larger than the viscous modulus within this bandwidth. In many applications, it is of interest to express material properties not in terms of the complex shear modulus but in terms of rheological models describing elastic and viscous properties of the material. Deciding on the model best suited to describe viscoelastic characteristics of the material will depend on the shape of the frequency dependant storage and loss modulus curves. Figure 7.9 shows that shear storage modulus is approximately constant with frequency and the loss modulus increases linearly with frequency. The simplest model that can describe this behavior is the Kelvin-Voigt (KV) model, where $G' = \mu$ and $G'' = \omega\eta$. We estimated the mean shear elastic modulus over three voltage excitations to be $\mu = 428 \pm 30$ Pa and the shear dynamic viscosity $\eta = 0.05 \pm 0.019$ Pa·s. These estimates of μ agree with those made using the phase gradient approach while estimates η are comparatively smaller Chapter 4. Moreover, the Zener model assumes frequency dependent storage modulus, which for the given data is not the case. Hence, the Zener model is not appropriate to model viscoelastic properties of gelatin.

To evaluate the performance of the MLEF Bayesian estimator we simulate

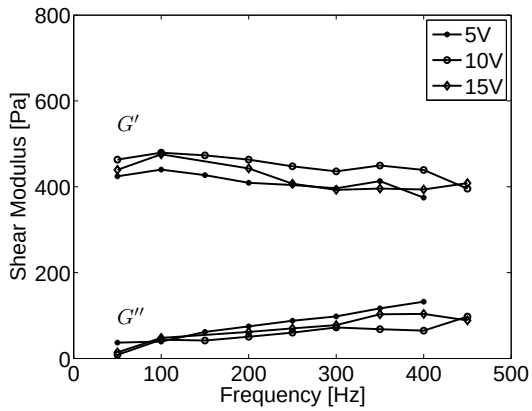

Figure 7.9: Estimated storage and loss moduli, G' and G'', from shear waves in 4% gelatin gel and for three actuator voltage amplitudes.

spatiotemporal particle velocities in media using proposed Doppler simulator. Material properties simulated are $\alpha = 11.5$ Np m^{-1} and $k_s = 416$ m^{-1}. Cylindrical wave equation is numerically imaged over 60 spatial locations sampled on the interval 0.46 mm (pitch of the Doppler array). These material properties correspond to a shear elastic modulus $\mu = 570$ Pa and shear dynamic viscosity $\eta = 0.1$ Pa·s. The ensemble size used in this study was $S = 30$.

Convergence of the parameters for one of the realizations at 50 Hz is illustrated in Figs. 7.10 and 7.11. Convergence of the parameters, α and k_s, as a function of time steps is presented. Attenuation, Fig. 7.10, converges within 50 time steps. Solid line represents true value and dashed line represents parameter value. Convergence is the approach from initial guess toward a definite value, a true value in the case of simulation. After 30 time steps, the filter converges within 5% error compared to the true value of the attenuation. This is similar to the the experimental data set case, Fig. 7.4. Wavenumber, Fig. 7.11, converges faster than the attenuation and within 15 steps is within 2% error compared to the true wavenumber.

Similarly to the experimental data case, the last estimate of state space is compared to the last observation of particle velocities in Fig. 7.12. The MLEF estimate of the state space is smooth compared to the simulated observation data.

Particle velocities at distinct spatial locations as a function of time steps are compared for simulated observational data and MLEF filtered data. Three locations at 4.6, 13.8 and 27.4 mm from the source are illustrated in Figs. 7.13,

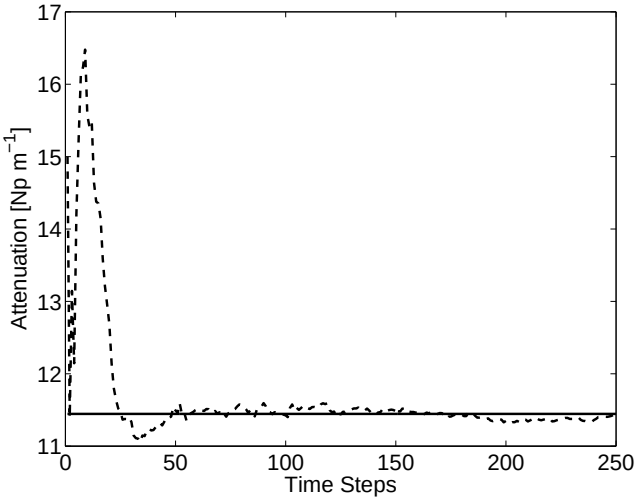

Figure 7.10: Convergence of the attenuation parameter α as a function of time steps for simulated data set. True value of the attenuation is indicated by a solid black line and MLEF tracking by a dashed black line. After 30 time steps the filter converges within 5% error compared to true value of the attenuation.

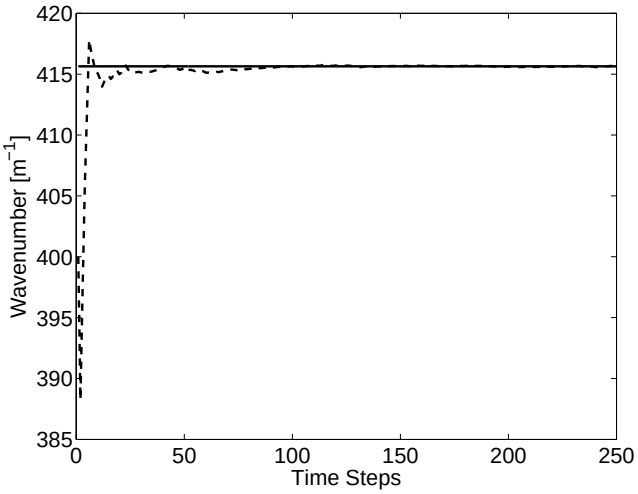

Figure 7.11: Convergence of the wavenumber parameter k_s as a function of time steps for simulated data set. True value of the wavenumber is indicated by a solid black line and MLEF tracking by a dashed black line. The filter quickly converges within 15 steps with error less than 2% compared to true value of wavenumber.

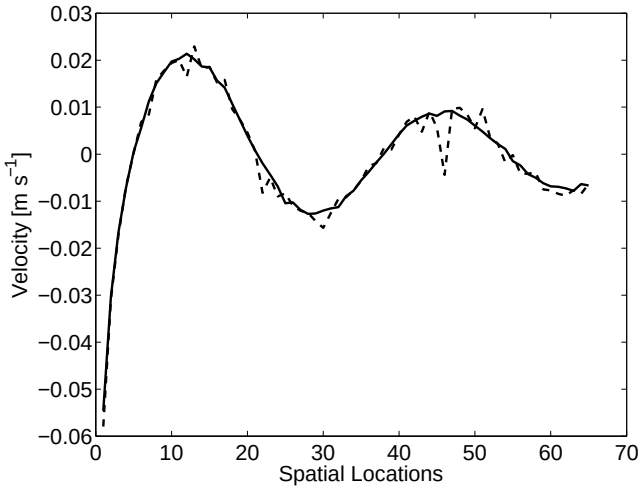

Figure 7.12: Doppler estimates of simulated particle velocities are compared with those estimated by the MLEF filter as a function of space. Data are compared for the final time step. Doppler measurements are indicated by a dashed black line and MLEF tracking estimates by a solid black line.

Table 7.1: Estimated material parameters over 20 realizations using MLEF.

Freq. [Hz]	μ [Pa]	η [Pa s]
50	571.2 ± 0.9	0.0985 ± 0.0071
100	570.1 ± 0.4	0.0995 ± 0.0020
150	570 ± 0.56	0.0991 ± 0.0010

7.14 and 7.15 respectively. Similarly to experimental data, amplitude of the sinusoidal function closer to the source is larger because the wave is less attenuated. Also, in Fig. 7.15, variance of the sinusoidal signal is larger compared to the Figs. 7.14 and 7.13.

We tested MLEF performance over 20 realizations for three frequencies of 50, 100 and 150 Hz. The results are summarized in Table 7.1. We found excellent agreement between MLEF estimated parameters and input simulation parameters as characterized by a standard error less than 2%.

On the same data sets we estimated complex shear modulus using AHI (Chapter 6). The algorithm was adapted for 1-D data. We followed the same computational steps as in Chapter 6. Performance of AHI is evaluated over 20 realizations and three frequencies, the same as MLEF, on the same simulated data sets. Results are summarized in Table 7.2. The 1-D algorithm is suited for plane wave propagation and cannot compensate for the diffrac-

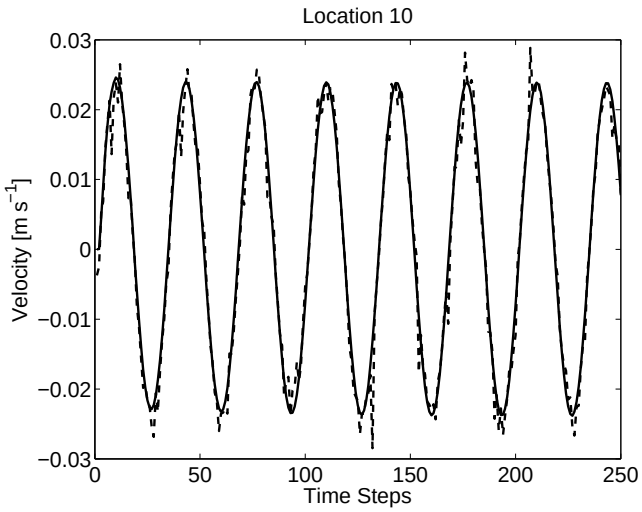

Figure 7.13: Doppler estimates of simulated particle velocities are compared with those estimated by the MLEF filter as a function of time. Data are compared for distinct spatial location 4.6 mm from the source. Doppler measurements are indicated by a dashed black line and MLEF tracking estimates by a solid black line.

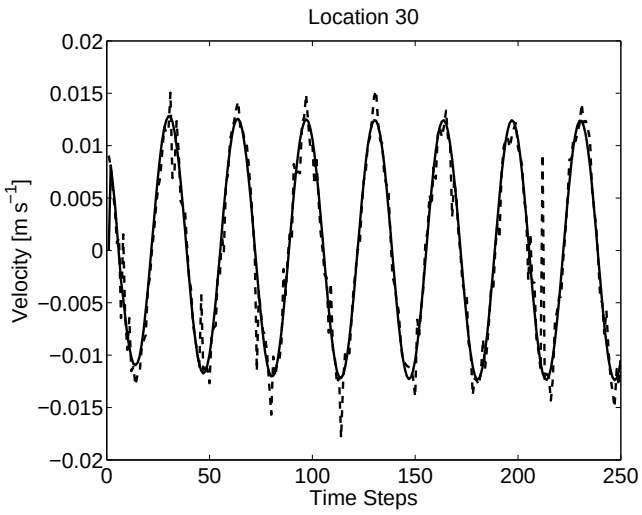

Figure 7.14: Doppler estimates of simulated particle velocities are compared with those estimated by the MLEF filter as a function of time. Data are compared for distinct spatial location 13.8 mm from the source. Doppler measurements are indicated by a dashed black line and MLEF tracking estimates by a solid black line.

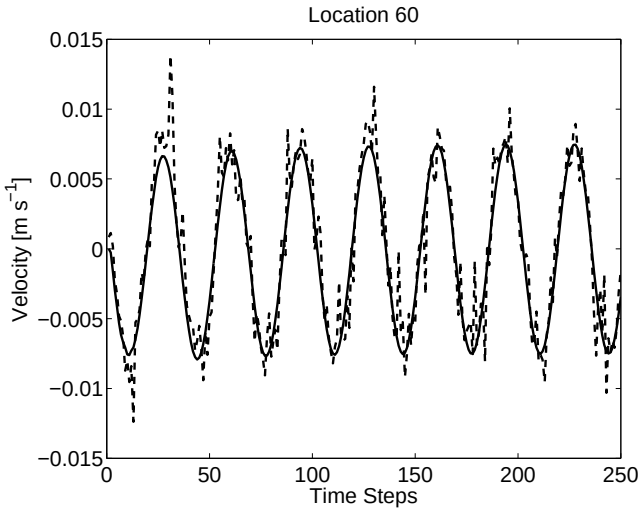

Figure 7.15: Doppler estimates of simulated particle velocities are compared with those estimated by the MLEF filter as a function of time. Data are compared for distinct spatial location 27.6 mm from the source. Doppler measurements are indicated by a dashed black line and MLEF tracking estimates by a solid black line.

Table 7.2: Estimated material parameters over 20 realizations using 1-D AHI.

Freq. [Hz]	μ [Pa]	η [Pa s]
50	559.4 ± 2.8	0.39 ± 0.014
100	566.8 ± 1.6	0.17 ± 0.003
150	576 ± 6.3	0.13 ± 0.047

tion effect of the cylindrical shear wave propagation, hence reconstructed values will be biased [33]. This bias affects stronger the reconstruction of the low magnitude value of the shear viscosity compared to the shear elastic modulus reconstruction.

7.5 Conclusion

A complex shear modulus reconstruction method based on the inversion of shear wave spatiotemporal propagation excited by a vibrating needle is presented. In our study we demonstrate the feasibility of using shear wave propagation and a stochastic filter to estimate the underlying material parameters.

Quantitative estimation of the viscoelastic properties is demonstrated on soft gelatin gel samples.

We established the feasibility of estimating complex shear modulus constants for single shear wave excitation frequencies. Moreover, since phase gradient methods require large bandwidths for the dispersion reconstruction, an advantage of the MLEF approach is the direct reconstruction of the complex shear modulus per shear wave excitation frequency. Hence, MLEF reconstructs complex shear modulus with higher spectral resolution compared to the phase gradient methods. This allows for better rheological modeling of material parameters.

Spatiotemporal MLEF filter reconstruction of the shear complex modulus compares closely to values estimated by a standard shear wave dispersion technique for the Kelvin-Voigt assumption. Moreover, results in Fig. 7.9 support the Kelvin-Voigt model since the storage modulus is roughly constant across the bandwidth of the measurement and the loss modulus increases linearly across the same bandwidth. This conclusion coincides with our previous finding [20] that the Kelvin-Voigt model provides representative description of the gelatin shear modulus in the 50-450 Hz bandwidth.

We compared the algebraic inversion method for the complex shear modulus reconstruction used in Chapter 6 with MLEF estimation. MLEF reconstruction of complex shear modulus is characterized by lower variance of the estimates and higher accuracy in the estimation of the mean material properties compared to AHI. With AHI estimation, large error in estimated mean dynamic viscosity is observed at 50 Hz. This agrees with reports by other investigators with similar troubling results for the viscous constant [105].

The work presented in this chapter mitigated the major limitations of the phase gradient approach (Chapter 4), and the algebraic Helmholtz inversion (Chapter 6). Furthermore, in the current form the technique can be easily adapted for commercial medical systems that use acoustic radiation force excitation. However, for the commercial systems based on the acoustic radiation force excitations using proposed cylindrical shear wave model could result in the systematic bias in estimated material properties. By reducing the number of spatial locations used for the filtering, potentially, images of the complex shear modulus might be made in 2D. Moreover, provided results motivate further explorations of stochastic filtering for complex shear modulus reconstruction. The possibility exists, similar to Tada et al. [118], to

use the numerical 3-D FDTD model developed in Chapter 6 with the MLEF filter to reconstruct 3-D complex shear modulus in an online manner. Such an approach would not suffer from the loss of spatial resolution, as do the phase gradient method and the proposed implementation of MLEF.

CHAPTER 8

CONCLUDING REMARKS

Ultrasonic shear wave imaging is sufficiently established to provide methodologies for clinical imaging. As a result, there exists an excellent qualitative understanding of shear elastic modulus and shear wave velocity reconstruction in elastic and viscoelastic materials. Fundamental laws governing shear wave propagation in homogenous viscoelastic materials are well known. This theoretical picture is in remarkable agreement with observations, as discussed in Chapters 4 and 6. However, sources of viscoelastic contrast are still poorly understood. Lacking is a theoretical framework linking the tissue pathology to viscoelastic contrast. Moreover, in clinical settings, results relate mostly to stiffness, shear elastic modulus or shear wave velocity. The reason for this is in part, that the elastic modulus is directly related to stiffness, which physicians are accustomed to using via palpation. Although stiffness is correlated to pathology, it is not a sufficient criterion for diagnosis [39]. Arguably, other mechanical parameters such as shear viscosity could be very useful for increasing the mechanical contrast in measurements [49]. Lack of evidence in the literature that viscosity carries diagnostic information limits clinicians from demanding tools capable of providing viscoelastic reconstructions.

For that reason this dissertation work presented several developments in the field of ultrasound elasticity imaging and complex shear modulus reconstruction. Most importantly, it provides evidence that there is useful additional information when reconstructing the complex shear modulus. Specifically, several developed techniques in this dissertation demonstrated quantitative complex shear modulus reconstruction under various assumptions. A comprehensive approach includes experimental studies, analytical studies and numerical simulations. Experimental studies were designed to address specific aims in characterization of proposed techniques. Also, models and numerical methods for simulating shear wave propagation in viscoelastic heterogeneous media and the Doppler estimation of particle velocities have been

presented, which serve to further understanding of current and future applications.

The initial idea was to follow the mainstream approach and use acoustic radiation force for the excitation of the shear wave propagation. First, a calibration technique was adapted in Chapter 2, which quickly led to developing the first quantitative method based on the acoustic radiation force step response as presented in Chapter 3. Compared to other similar methods, the calculation of radiation force on the sphere is not crucial in the application described in this dissertation, because complex shear modulus can be determined without the knowledge of the magnitude of the force. The only assumption made, if comparing results with other methods, is that the measurement was made in the linear range of the material. This is a valid assumption for gelatin phantoms, as addressed several times throughout this dissertation. The primary disadvantage of this method is the requirement of a calibrated target. This can limit the application potential of this technique. Nevertheless, if applicable, this simple yet elegant time domain measurement yields an estimate of complex shear modulus under the Kelvin-Voigt assumption. The analytical framework presented in Appendix A could be extended to include higher order models. One application in mind when this technique was developed was characterization of engineered tissue samples and 3-D cell cultures. The proposed approach is feasible for these applications, since known scatterers can be embedded in the process of sample preparation.

In the latter chapters of this dissertation a different approach was favored over acoustic radiation force for shear wave excitation. Several reasons led to choosing harmonic shear wave excitation using a steel needle vibrated by an external mechanical actuator. First, strong coupling between the needle and the material results in large displacement of the medium which is a favorable condition for the Doppler estimation of particle velocities. Second, excited waves are not only exclusively shear waves but have a well-defined geometry of cylindrical shear wave propagation that is used to our advantage to reconstruct complex shear modulus. In this way, the requirement of a calibrated target is eliminated and images of shear properties can be formed if the object is scanned and local homogeneity is assumed. While others seek diagnostic methods, the agenda in this dissertation is to develop sophisticated tools to further the understanding of the basic science which enables use of more-invasive methods for shear wave excitation.

Using the proposed approach for shear-wave excitation, a phase gradient-based method was developed for shear-wave velocity estimation from which the complex shear modulus can be reconstructed via a fit to the dispersion equation. In order to enhance the quality of estimated complex shear modulus, possible sources of variance in this measurement were examined. Quality of estimation for any of the methods presented in this dissertation will depend on the quality or velocity signal-to-noise ratio of estimated particle velocities using the Doppler approach, where lower variance of estimates defines better quality of data for use with the next level estimators. In order to reduce variance of the estimated particle velocities, a lag-k estimator is adapted from weather radar literature in Chapter 4. Performance of the proposed estimator is statistically studied via experiments and simulations. For the given imaging conditions of high imaging SNR (>25 dB), improvement in statistics of up to 15 % was registered. Feasibility of the proposed method for the complex shear modulus reconstruction was demonstrated and the technique was characterized on gelatin phantoms. The quantitative nature of measurements is verified via comparison with rheometer. Excellent agreement was found between elastic shear modulus values estimated by rheometer and those estimated by the shear-wave imaging. Experimental results suggest the Kelvin-Voigt model is capable of capturing viscoelastic properties of the gelatin phantoms.

Previous study provided confidence in the accuracy of this method and results and it was used to study viscoelastic properties of soft biological tissues (Chapter 5). The initial idea was to observe how well standard rheological models represent measurements of shear-wave speed in parenchymal tissues. The complex modulus of fresh, ex vivo, porcine liver was estimated. Moreover, complex shear modulus was modified by heating the tissue to enhance viscoelastic effects. Porcine liver was chosen because measurements could be readily verified through literature comparisons, and the results contribute to the accumulating data on assessments of thermal tissue damage induced during ablation procedures.

Analysis of the shear-wave dispersion curves confirmed that due to thermal damaging, liver undergoes substantial changes in complex shear modulus. Interestingly, the dynamic viscosity "constant" η, for liver tissue was found to exhibit greater sensitivity than elastic shear modulus, μ_1, to thermal damage. This offset in contrast, where the dynamic viscosity increased three fold and

the elastic shear modulus increased twofold, represents the first evidence of the value in complex shear modulus reconstruction. Our data on estimated dispersion for the fresh porcine liver, in agreement with results from other groups, provided evidence supporting several other claims. First, the agreement suggests that liver perfusion, temperature, and measurement technique are not major factors in shear-wave measurements of μ_1. Second, for comparison with human liver, although the findings are consistent and perhaps expected given known differences in lobular collagen content between humans and pigs, none of the observed species-specific differences in shear properties can be considered statistically significant when measurement uncertainties are considered. Hence, based on the shear wave measurements within the given bandwidth, inter-species differentiation is not possible. It is important to point out that the heating regimen thermally induced biochemical changes to liver tissue and influenced the complex modulus to a greater extent than variations in anatomical structure. Histology reports showed no apparent thermally-induced changes in cellular architecture. Therefore, this result suggests that shear wave imaging is more sensitive than histology given experimental conditions described.

To study limitations imposed by the various assumptions in shear-wave imaging, a finite-difference time-domain numerical method was developed (Chapter 6). The developed 3-D FDTD solver is capable of simulating shear-wave propagation in time and three spatial dimensions in heterogeneous media. These numerical methods are based on an extensive seismic research literature, e.g., [107, 108, 109]. The role of simulation is thus twofold here; simulations can be used for testing different complex shear modulus imaging techniques, and estimating their accuracy. In addition, simulations can provide important insight on how to design experiments to reduce the errors in shear-wave velocity estimation due to reflections. For example, the simulations can help in the selection of geometry based on the excitation frequency, or in selection of a better suited shear-wave excitation. In both cases, understanding 3-D shear-wave propagation in heterogeneous viscoelastic media is crucial. Better understanding of these effects will open a new avenue in quantitative shear wave imaging and complex shear modulus reconstruction.

The direct algebraic Helmholtz inversion (AHI) algorithm was studied, and sensitivity of various assumptions intrinsic to the AHI algorithm were tested by comparing imaging results from simulated and experimental data. It was

found that it is essential to measure velocity components in all three spatial dimensions for which medium heterogeneities have significant curvature in order to avoid artifacts. Moreover, the conducted study of the influence of viscosity on shear wave propagation in heterogeneous materials provided further evidence of the added value of information in viscosity reconstruction. By reconstructing complex shear modulus it was possible to spatially register highly viscous inclusion and to avoid artifacts that one might encounter when reconstructing only the elastic modulus.

To alleviate degradation of the spectral resolution of the phase gradient method and bias associated with algebraic inversion when imaging in 1-D or 2-D this research project examined the applicability of a stochastic filtering approach to complex shear modulus reconstruction (Chapter 7). A recursive dynamic cylindrical shear wave model is introduced and utilized to reconstruct complex shear modulus from noisy observations of particle velocities. Specifically, it was demonstrated using stochastic filtering that the proposed method can reconstruct the complex shear modulus per excitation frequency in homogeneous materials. It was also illustrated on the experimentally acquired data of shear wave propagation in gelatin phantoms that the best way to decide on the appropriate model of the material is from the complex modulus spectra. Presented results support previous findings throughout this dissertation work that the gelatin can be modeled via Kelvin-Voigt viscoelastic model. Accuracy of the proposed method was studied via numerical simulations with realistic Doppler imaging parameters. Simulation results yield high accuracy of proposed approach with error within 2%.

When 3-D dynamic data sets are available, data processing time is not of interest, and material is sufficiently viscous, algebraic inversion is recommended over any of the other methods studied in this dissertation. It provides reconstruction per frequency with high spatial resolution that the other methods do not provide. In contrast, when the spatial requirement is not met for homogeneous materials, stochastic filtering with the cylindrical shear wave model provides optimal estimates of the complex shear modulus. Moreover, with stochastic filtering the complex shear modulus can be estimated in an online manner per frequency with low variance.

This dissertation presented work that is part of a larger interdisciplinary group effort. The major focus is to develop an experimental and theoretical framework capable of linking physical to biological sources of viscoelastic

contrast. Physical sources of elasticity contrast are related to the spatial variations in flow velocity of fluids through the extracellular matrix (poroelasticity) and the rate at which the matrix itself mechanically relaxes (viscoelastic) in response to applied forces.To study the relationships between two sources of contrast, 3-D cell cultures are developed as controllable biological phantoms. Understanding these relationships is the way to bridge molecular, cellular, and tissue biology and might lead to new approaches in the treatment of patients [6].

This dissertation provided evidence of an added value of information in reconstruction of the complex shear modulus. Studies like this one can motivate further studies to determine quality of the loss modulus or dynamic viscosity (in the case of K-V model) as a diagnostic parameter. Such a research endeavor would require not only clinical studies but also an interest by some of the big manufacturers to adapt for medical grade ultrasound systems techniques capable of reconstructing the complex shear modulus. Ultimately, contrast to variability (whether from noise or biologic variability) determines the quality of a parameter for specific diagnosis, not just the contrast.

8.1 Future Outlook

In this dissertation several experimental and theoretical aspects of shear wave imaging and complex shear modulus reconstruction are addressed. Still, it is by no means the final word on that topic. The following presents some directions for future work.

Variance of the estimated particle velocities could be further decreased. It is common practice in ultrasound shear wave imaging to average axially the estimated particle velocities or displacements to reduce the variance. This is an acceptable loss of axial spatial resolution since axial sampling is usually much larger than lateral (> 10 times). Nevertheless, averaging L correlated samples does not reduce variance L times. One way to overcome this would be to statistically decorrelate the range samples in such a manner that, upon averaging, the variance of the velocity would be reduced by L times. This could be achieved by using a statistical whitening transform [128]. It was demonstrated in weather radar literature that such an approach is feasible [129]. Any improvement in the quality of estimated particle velocities has a

direct impact on the next level of estimators that produce quantities from the particle velocity data. Moreover, the impact of the method could be broader since it is directly applicable to blood flow imaging problems.

The favored approach in this dissertation for shear wave excitation is needle vibration. Although invasive, such an approach is acceptable for studying complex shear modulus of engineered tissues and 3-D cell cultures. Nevertheless, the proposed methods under specific conditions can complement current biopsy procedures and be implemented in clinical settings. Ideally, the proposed method could be coupled with an optical method such as Fourier transform infrared (FTIR) spectroscopy (a common technique employed to identify a material and relate its properties to the molecular structure). A multi-modal approach could yield both chemical and mechanical properties of tissue during a biopsy procedure, as in the case of breast cancer.

The proposed stochastic filtering approach for complex shear modulus reconstruction can be further extended to include more-complicated dynamic models. As an example, the proposed approach using MLEF filter can be coupled with the developed 3-D FDTD solver to potentially reconstruct the complex shear modulus in 3D. Such optimal reconstruction of the complex shear modulus would not suffer from blurring like the AHI method. Moreover, stochastic filtering allows for tracking of the dynamics of the parameters. The 3-D FDTD solver can be extended to include heat transfer. Such a solver could be used to simulate shear wave propagation during ablation procedures. Via data assimilation approach, the ablation temperature and the extent of thermal damage could be monitored in real time.

APPENDIX A

MATERIAL PROPERTIES FROM MECHANICAL IMPEDANCE

The viscoelastic material properties of the gel medium surrounding a rigid sphere are frequently characterized by the mechanical impedance, Z, which relates, in three spatial dimensions, $\mathbf{y} = y_1, y_2, y_3$, and time, t, the resistance force of the sphere to motion, $\mathbf{F}(t, \mathbf{y})$, and the resulting sphere velocity, $\mathbf{v}_s(t, \mathbf{y})$, via the Ohm's law-like expression [58]

$$\mathbf{F}(t, \mathbf{y}) = -Z \times \mathbf{v}_s(t, \mathbf{y}) \ . \tag{A.1}$$

Force and velocity are vector quantities, impedance is a scalar, and all three are complex quantities in this expression. Stationary harmonic forces at radial frequency ω applied along the y_1 axis and of the form $F(t) = F_{\omega,1} \exp(-i\omega t)$ generate sphere velocities of the form $v_s(t) = v_{\omega,1} \exp(-i\omega t)$. In that situation, the material properties that influence Z are gel density $\rho \simeq 1$ g/cm^3, sphere radius $a = 0.75$ mm, and the complex Lamè moduli $\mu' = \mu_1 - i\omega\mu_2$ and $\lambda' = \lambda_1 - i\omega\lambda_2$. Parameter μ_1 is shear elasticity, μ_2 is shear viscosity, λ_1 is volume compressibility, and λ_2 is volumetric viscosity. For the small forces used in our experiments, it is assumed the gel responds linearly so the sphere velocity for an arbitrary time-varying force is a weighted linear superposition of velocities at each frequency in the force bandwidth. Further, it is assumed that the sphere is bound to the continuous, homogeneous, and isotropic gel.

Of course, the force and velocity vectors also vary spatially. For harmonic, compressional, plane waves traveling along the y_1 axis, $F(t, \mathbf{y})\, \hat{\mathbf{y}}_\mathbf{1} = F_{\omega,1} \exp(ky_1 - \omega t)$, the impedance is straightforward to find from Eq. A.1 and the 1-D wave equation, as shown in standard texts [58].

The mechanical impedance Z for the case of an oscillating sphere was found by Oestreicher [130]. Making use of the spherical symmetry, he separately solved for the irrotational and incompressible components of the wave equa-

tion relating pressure and displacement in terms of spherical harmonics [70]. Integrating the pressure over the sphere to find force and for $v_s(t) = -i\omega x(t)$, he found

$$Z = -\frac{4}{3}\pi a^3 \rho i\omega \left\{ 1 - \left[\frac{1}{3}\left(1 - \frac{3(1 - ik_c a)}{k_c^2 a^2}\right)^{-1} - \frac{2}{3}\left(1 - \frac{3(1 - ik_s a)}{k_s^2 a^2}\right)^{-1} \right]^{-1} \right\} . \tag{A.2}$$

The above expression is the form given by Norris (see Eq. 5 in Ref.[131]). In Eq. A.2, $k_c = (\rho\omega^2/(2\mu' + \lambda'))^{1/2}$ and $k_s = (\rho\omega^2/\mu')^{1/2}$ are, respectively, the compressional and shear complex wave numbers. The wave number $k_s = \omega/c_s + i\alpha_s$ may also be written as a function of the shear wave speed and shear wave attenuation constant, respectively [84],

$$c_s = \omega/\Re\{k_s\} = \sqrt{\frac{2(\mu_1^2 + \omega^2\mu_2^2)}{\rho(\mu_1 + \sqrt{\mu_1^2 + \omega^2\mu_2^2})}} \tag{A.3}$$

and

$$\alpha_s = \Im\{k_s\} = \sqrt{\frac{\rho\omega^2(\sqrt{\mu_1^2 + \omega^2\mu_2^2} - \mu_1)}{2(\mu_1^2 + \omega^2\mu_2^2)}} . \tag{A.4}$$

Oestreicher [130] comments that the number of constants in the Lamè moduli increases if time derivatives of order greater than one are required to model the data. For harmonic oscillations, the corresponding Lamè moduli will have added terms multiplied by increasing powers of $-i\omega$. Higher-order time derivatives generate frequency dependent Lamè moduli that appear experimentally as dispersion; i.e., frequency dependent wave speeds. It was shown experimentally [67] that gelatin is non-dispersive for compressional waves between 1 and 10 MHz with and without particle scatterers. Applying Eq. A.3 and the values of μ_1 and μ_2 reported in Chapter 3, it can be seen that c_s varies by less than 0.7% for clear gelatin gels at shear-wave frequencies less than 50 Hz. Consequently, it is reasonable to assume non-dispersive media for our low-frequency experiments.

In incompressible viscoelastic gels, the bulk modulus $\lambda + 2\mu/3$ becomes infinite while μ remains finite [131]. We measured $c_c = 1506$ m/s and $\mu_1 = 317$ Pa for clear 3% gelatin gels, and adopt $\mu_2 = 0.1$ Pa·s as Ilinskii [37].

Applying the expressions from the paragraph below Eq. A.2, we estimate that $c_s = 0.56$ m/s and $\lambda_1 = 2.25 \times 10^9$ Pa. Further, like Oestreicher [130], we assume $\lambda_2 = 0$. Consequently, $k_c/k_s \ll 1$, and Eq. A.2 reduces to

$$Z' = -\frac{6\pi a \mu'}{i\omega}\left[\frac{k_s^2 a^2}{9} - \left(1 - ik_s a\right)\right] \tag{A.5}$$

provided the sphere remains bound to the gelatin [131]. Expanding Eq. A.5 using $\mu' = \mu_1 - i\omega\mu_2$, we find

$$\begin{aligned} Z' = &-6\pi a\left[\mu_2\left(1 - \frac{k_s^2 a^2}{9}\right) + \frac{\mu_1}{\omega}k_s a\right] \\ &- i6\pi a\left[\frac{\mu_1}{\omega}\left(1 - \frac{k_s^2 a^2}{9}\right) - \mu_2 k_s a\right] . \end{aligned} \tag{A.6}$$

Noting that $\mu_2/\mu_1 \ll 1$ and $a = 7.5 \times 10^{-4}$, we neglect all terms $\mathcal{O}(a^3)$ and $\mathcal{O}(\mu_2 a^2)$ to find

$$Z'' \simeq -6\pi a\left(\mu_2 + \frac{\mu_1 k_s a}{\omega} - i\frac{\mu_1}{\omega}\right) . \tag{A.7}$$

Finally, expanding k_s as a function of c_s and α_s we can rewrite Eq. A.7 as

$$Z'' = -6\pi a\left(\mu_2 + \frac{\mu_1 a}{c_s} - i\frac{\mu_1}{\omega}(1 + \alpha_s a)\right) . \tag{A.8}$$

Impedance, Z, and its approximations, Z' and Z'', were evaluated numerically using values for constants listed above. The real parts are plotted in Fig. A.1 and the imaginary parts in Fig. A.2. There is no significant difference among the three expressions provided $\omega/2\pi < 100$ Hz, where we are free to adopt Eq. A.8. The damping constant, R from Eq. 3.4, corresponds to the real part of the mechanical impedance, Z''. Comparing R in Eq. 3.6 with $\Re\{Z''\}$ in Eq. A.8, we find $\eta = \mu_2 + \mu_1 a/c_s$. Also, since $v_s(t) = -i\omega x(t)$, comparing μ from Eq. 3.7 with $\Im\{Z''\}$ in Eq. A.8 yields $\mu = \mu_1(1+\alpha_s a) \simeq \mu_1$ for our experimental conditions.

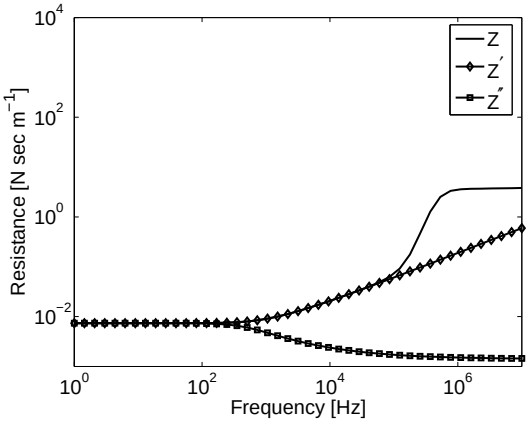

Figure A.1: Mechanical resistance (real part of impedance) for an oscillating sphere in 3% gelatin gel.

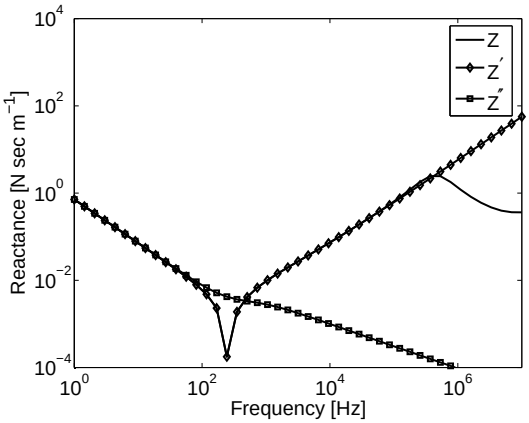

Figure A.2: Mechanical reactance (imaginary part of impedance) for an oscillating sphere in 3% gelatin gel.

APPENDIX B

SPATIAL PHASE ESTIMATION

This appendix shows that the model for the spatial phase gradient of shear waves described by Eq. 5.2 is related to lateral estimates of spatial phase from Eq. 5.1 by the equation $d\psi/dx \simeq \arg(\hat{\psi})/X$. This discussion follows a derivation by Jensen [56].

The analytic signal for particle velocity as a function of lateral position $\hat{v}'(x)$ is a function of the Hilbert transform of velocity $\hat{v}_h(x)$, viz.,

$$\begin{aligned}\hat{v}'(x) &= \hat{v}(x) + i\hat{v}_h(x) \\ &= \sqrt{\hat{v}^2 + \hat{v}_h^2}\, e^{i\tan^{-1}(\hat{v}_h/\hat{v})} = A(x)e^{i\psi(x)} \ . \end{aligned} \tag{B.1}$$

Noting explicitly that x is sampled and that $\psi[\ell] \triangleq \psi(x[\ell])$, we have

$$\begin{aligned}\triangle\psi[\ell] &= \psi[\ell+1] - \psi[\ell] \\ &= \tan^{-1}\left(\frac{\hat{v}_h[\ell+1]}{\hat{v}[\ell+1]}\right) - \tan^{-1}\left(\frac{\hat{v}_h[\ell]}{\hat{v}[\ell]}\right) \ . \end{aligned} \tag{B.2}$$

Using the identity

$$\tan(A-B) = \frac{\tan(A) - \tan(B)}{1 + \tan(A)\tan(B)} \ , \tag{B.3}$$

we find

$$\triangle\psi[\ell] = \tan^{-1}\left(\frac{\hat{v}_h[\ell+1]\hat{v}[\ell] - \hat{v}_h[\ell]\hat{v}[\ell+1]}{\hat{v}[\ell+1]\hat{v}[\ell] + \hat{v}_h[\ell]\hat{v}_h[\ell+1]}\right) \ . \tag{B.4}$$

Turning to measurements, the kernel of the lag one correlation estimate

without averaging is

$$\begin{aligned}\hat{v}'^*[\ell]\,\hat{v}'[\ell+1] &= (\hat{v}[\ell] - i\hat{v}_h[\ell])\,(\hat{v}[\ell+1] + i\hat{v}_h[\ell+1]) \\ &= (\hat{v}[\ell]\hat{v}[\ell+1] + \hat{v}_h[\ell]\hat{v}_h[\ell+1]) \\ &\quad + i(\hat{v}[\ell]\hat{v}_h[\ell+1] - \hat{v}_h[\ell]\hat{v}[\ell+1])\ . \end{aligned} \tag{B.5}$$

So we can write

$$\begin{aligned}\arg(\hat{\psi}[\ell]) &= \tan^{-1}\left(\frac{\hat{v}_h[\ell+1]\hat{v}[\ell] - \hat{v}_h[\ell]\hat{v}[\ell+1]}{\hat{v}[\ell+1]\hat{v}[\ell] + \hat{v}_h[\ell]\hat{v}_h[\ell+1]}\right) \\ &= \triangle\psi[\ell], \end{aligned} \tag{B.6}$$

and finally

$$\frac{d\psi}{dx} \simeq \frac{\triangle\psi[\ell]}{X} = \frac{\arg(\hat{\psi}[\ell])}{X} \tag{B.7}$$

provided $X \ll 2\pi c_s/\omega$.

APPENDIX C

KALMAN FILTER DERIVATION

The purpose of this appendix is to supplement the derivation of the cost function found in Chapter 7. Explicitly, we show that by minimizing the cost function defined by Eq. 7.7 using Newton's approach, a linear Kalman filter is derived under the assumptions of a linear models equation and linear observer operator. Similar derivations can be found in Jazwinski [120], Section 7.3, Example 7.3 (maximum liklehood) or in [122]. Moreover, we show a classical approach for dealing with nonlinear systems by using Taylor series expansion. This is the so-called "extended Kalman Filter approach." We present a study on de-noising particle velocity images using the extended Kalman filter approach.

Assume linear observation and prediction model operator, i.e. quadratic cost function. The cost function is derived in Chapter 7, Eq. 7.7. Optimal $\mathbf{x}$ can be found using Newton's method for optimization, which theoretically converges in a single iteration for quadratic cost function. The solution is

$$\mathbf{x}^{k+1} = \mathbf{x}^k + \alpha^k d^k \tag{C.1}$$

where k is the minimization iteration index, α is the line search (step-length) constant, and d is the descent direction vector. Since the cost function is quadratic (observation operator, $\mathbf{H}$, is linear), the Newton's method produces an optimal line search $\alpha = 1$ (e.g. Luenberger and Ye [132]). In Newton's method,

$$d = -\left(\frac{\partial^2 \mathcal{J}}{\partial \mathbf{x}^2}\right)^{-1} \left(\frac{\partial \mathcal{J}}{\partial \mathbf{x}}\right) , \tag{C.2}$$

where $\left(\frac{\partial^2 \mathcal{J}}{\partial \mathbf{x}^2}\right)^{-1}$ is inverse Hessian and $-\left(\frac{\partial \mathcal{J}}{\partial \mathbf{x}}\right)$ is a negative gradient of the

cost function. Starting from $\mathbf{x}^f$ as the first guess in minimization, as the best available initial value, one can write optimal solution of Eq. 7.7 as

$$\mathbf{x} = \mathbf{x}^f - \left(\frac{\partial^2 \mathcal{J}}{\partial \mathbf{x}^2}\right)^{-1} \left(\frac{\partial \mathcal{J}}{\partial \mathbf{x}}\right), \tag{C.3}$$

with the assumption of $\alpha = 1$. The gradient and the Hessian of the function can be explicitly calculated using next matrix identities:

$$\frac{\partial}{\partial \mathbf{x}}(\mathbf{x}^T C \mathbf{x}) = 2C\mathbf{x}, \tag{C.4}$$

and

$$\frac{\partial}{\partial \mathbf{x}}(A\mathbf{x} + B)^T C(A\mathbf{x} + B) = 2A^T C(A\mathbf{x} + B), \tag{C.5}$$

where C is symmetric matrix for both Eqs. C.4 and C.5.

The gradient of Eq. 7.7 at $\mathbf{x} = \mathbf{x}^f$ is

$$\frac{\partial \mathcal{J}}{\partial \mathbf{x}} = \mathbf{P}_f^{-1}(\mathbf{x} - \mathbf{x}^f) - \mathbf{H}^T\mathbf{R}^{-1}(\mathbf{y} - \mathbf{H}\mathbf{x})|_{\mathbf{x}=\mathbf{x}^f} = \mathbf{H}^T\mathbf{R}^{-1}(\mathbf{y} - \mathbf{H}\mathbf{x}^f), \tag{C.6}$$

and the Hessian of Eq. 7.7 at $\mathbf{x} = \mathbf{x}^f$ is

$$\frac{\partial^2 \mathcal{J}}{\partial \mathbf{x}^2} = \mathbf{P}_f^{-1} + \mathbf{H}^T\mathbf{R}^{-1}\mathbf{H}. \tag{C.7}$$

A straightforward substitution of Eq. C.6 and Eq. C.7 in Eq. C.3 gives

$$\mathbf{x} = \mathbf{x}^f - (\mathbf{P}_f^{-1} + \mathbf{H}^T\mathbf{R}^{-1}\mathbf{H})^{-1}\mathbf{H}^T\mathbf{R}^{-1}(\mathbf{y} - \mathbf{H}\mathbf{x}^f). \tag{C.8}$$

Since the analysis error covariance is equal to the inverse Hessian [122], we have

$$\mathbf{P}_a = (\mathbf{P}_f^{-1} + \mathbf{H}^T\mathbf{R}^{-1}\mathbf{H})^{-1}. \tag{C.9}$$

The expressions Eqs. C.8 and C.9 are identical to Kalman filter analysis equations. Too see that, use the matrix identity (e.g., Jazwinski [120],

Appendix 7B, (7B.6))

$$(\mathbf{P}_f^{-1} + \mathbf{H}^T\mathbf{R}^{-1}\mathbf{H})^{-1}\mathbf{H}^T\mathbf{R}^{-1} = \mathbf{P}_f\mathbf{H}^T(\mathbf{H}\mathbf{P}_f\mathbf{H}^T + \mathbf{R})^{-1} \tag{C.10}$$

in Eq. C.8 to obtain the standard Kalman filter solution

$$\begin{aligned}\mathbf{x} &= \mathbf{x}^f - \mathbf{P}_f\mathbf{H}^T(\mathbf{H}\mathbf{P}_f\mathbf{H}^T + \mathbf{R})^{-1}(\mathbf{y} - \mathbf{H}\mathbf{x}^f) \\ &= \mathbf{x}^f - \mathbf{K}(\mathbf{y} - \mathbf{H}\mathbf{x}^f),\end{aligned} \tag{C.11}$$

where $\mathbf{K}$ is the Kalman gain. After applying Woodbury matrix identity

$$(A + UCV)^{-1} = A^{-1} - A^{-1}U(C^{-1} + VA^{-1}U)^{-1}VA^{-1} \tag{C.12}$$

to Eq. C.13, one obtains

$$\begin{aligned}\mathbf{P}_a &= \mathbf{P}_f - \mathbf{P}_f\mathbf{H}^T(\mathbf{H}\mathbf{P}_f\mathbf{H}^T + \mathbf{R})^{-1}\mathbf{H}\mathbf{P}_f \\ &= (\mathbf{I} - \mathbf{K}\mathbf{H})\mathbf{P}_f.\end{aligned} \tag{C.13}$$

In summary, following the state and covariance propagation (Chapter 7), Kalman filter algorithm is given with:

- *Forecast Step*

$$\mathbf{x}^f = \mathbf{M}\mathbf{x}^a \tag{C.14}$$

$$\mathbf{P}_f = \mathbf{M}\mathbf{P}_a\mathbf{M}^T \tag{C.15}$$

- *Analysis Step*

$$\mathbf{K} = \mathbf{P}_f\mathbf{H}^T(\mathbf{H}\mathbf{P}_f\mathbf{H}^T + \mathbf{R})^{-1} \tag{C.16}$$

$$\mathbf{x}^a = \mathbf{x}^f - \mathbf{K}(\mathbf{y} - \mathbf{H}\mathbf{x}^f) \tag{C.17}$$

$$\mathbf{P}_a = (\mathbf{I} - \mathbf{K}\mathbf{H})\mathbf{P}_f \tag{C.18}$$

In the case of non-linear prediction model $\mathcal{M}$ and non-linear observation operator $\mathcal{H}$, one could use the extended Kalman filter (EKF) equations, which are of the same form as Eqs. C.15-C.18, but with

$$\mathbf{M} = \left(\frac{\partial \mathcal{M}}{\partial \mathbf{x}}\right) \tag{C.19}$$

$$\mathbf{H} = \left(\frac{\partial \mathcal{H}}{\partial \mathbf{x}}\right). \tag{C.20}$$

The Jacobians in Eqs. C.19 and C.20 are calculated at the first guess.

C.1 De-Noising Particle Velocity Images

In this section a conducted study using the EKF approach is described. This material is presented as an appendix because it did not fit the main argument of Chapter 7; nevertheless, it represents a significant amount of work that led toward developments in Chapter 7. The study conducted was de-noising images of estimated particle velocities using stochastic filtering. This work was motivated by the results presented in Chapter 6. Direct algebraic reconstruction of the complex shear modulus operates on the images of Fourier transformed particle velocities Eq. 6.7. Prior to applying Eq. 6.7, we spatially filter $V_z(\boldsymbol{x}, \omega_0)$ in three dimensions using a low-pass second-order Butterworth filter with a cutoff frequency of 160 m^{-1}. Since the direct inversion process is not regularized, spatial filtering is essential [106]. Such filtering will act as a blurring function and, depending on the spatial features of wave patterns, results might be biased. Instead of spatially filtering an image in postprocessing, an alternative is to use stochastic filtering to de-noise particle velocities during acquisition (on-line estimation).

The simplest, yet an effective, approach is to perform temporal stochastic filtering. From the harmonic cylindrical shear wave equation solution, Eq. 4.9, it follows that in every spatial point of the medium only one harmonic component at the frequency of the excitation propagates. This can be modeled by sinusoidal function with known frequency and unknown phase and amplitude. With that in mind, and following the approach outlined in Chapter 7, a model equation for particle velocity at the given location is

given by

$$v_k = v_{k-1}\cos(\omega\triangle t) - A\sin(\omega(k-1)\triangle t - \phi)\sin(\omega\triangle t). \tag{C.21}$$

In Chapter 7 it was outlined that an approach to solving this problem is to form an augmented state vector. Similarly, as in Chapter 7, a direct observability of the particle velocities is assumed (ideal Doppler system). An augmented state estimation problem for the presented case is given by

$$\mathbf{x}_k = \begin{bmatrix} \mathbf{v}_k \\ \boldsymbol{\theta}_k \end{bmatrix} = \begin{bmatrix} \mathcal{M}\left(\mathbf{v}_{k-1}; \boldsymbol{\theta}_{k-1}\right) \\ \boldsymbol{\theta}_{k-1} \end{bmatrix}, \tag{C.22}$$

where $\mathbf{v}$ is the vector of radial particle velocities from Eq. C.21, $\boldsymbol{\theta} = [A\ \phi]^T$ is the parameter vector and $\mathcal{M}$ is the nonlinear forward operator defined by Eq. C.21. Material parameters are constant during data acquisition; i.e., $\dot{\boldsymbol{\theta}} = 0$.

Similarly, the augmented measurement equation gives the vector of velocity estimates $\hat{\mathbf{v}}$ as

$$\mathbf{y}_k = \begin{bmatrix} \hat{\mathbf{v}}_k \\ \mathbf{0} \end{bmatrix} = [\mathbf{I}\ \mathbf{0}] \begin{bmatrix} \mathbf{v}_k \\ \boldsymbol{\theta}_k \end{bmatrix} + \begin{bmatrix} \boldsymbol{\epsilon}_0 \\ 0\ . \end{bmatrix} \tag{C.23}$$

The augmented non-linear system formulation given by Eqs. C.22 and C.23 is solved following the extended Kalman filter approach presented in this appendix.

Data used in this experiment were collected from scanning a cylindrical inclusion phantom. Details about cylindrical inclusion phantom preparation are given in Chapter 6. The phantom used in this study was prepared with a stiff inclusion compared to the background. Inclusion was made with 8% gelatin concentration and the background was made with 4% gelatin concentration. Doppler imaging parameters are identical to those in Chapter 7 for the BW-14/60 probe, with the exception of PRF = 8 kHz. Shear wave excitation is at 100 Hz.

Figure C.1 illustrates spatial distribution of Doppler estimated particle velocities at approximately 375 ms from the start of the data acquisition. Change of wavelength is observed in the stiff inclusion compared to the background. Spatial noise in the image correlates with depth. For fixed focusing, SNR changes with depth. The deeper the acquisition, the lower the SNR and more variance can be observed in the image. In Fig. C.1, from 40 to 50

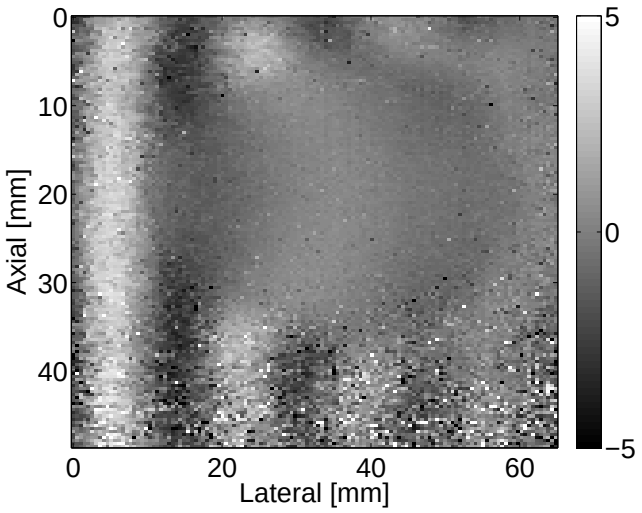

Figure C.1: Particle velocity image of a 100 Hz shear wave in gelatin phantom with cylindrical inclusion. Waves are generated by a needle vibrating outside of the image plane on the left-hand side. Bright and dark regions indicate particle velocities toward and away from the Doppler probe. The velocity range displayed is between -5 and +5 mm/s.

mm, an axially noisy feature is very strong and it is hard to resolve the wave pattern in this region. This is especially exaggerated in the lower right-hand side of the image where the magnitude of the shear wave velocity is smaller due to the attenuation effect of wave propagation through the sample.

In Fig. C.2 spatial distribution of EKF filtered particle velocities 375 ms from the start of the data acquisition is presented. Overall variance of the image is significantly reduced, especially in the deeper region between 40 and 50 mm axially. The wave pattern is clearly resolvable in the lower right-hand corner.

Calculation of Laplacians in Chapter 6 can benefit from this considerable reduction of variance in images. Moreover, the image de-noising procedure described does not affect the resolution of the produced images. The advantage of this approach is that it can be performed in an online manner during data acquisition. Alternatively, instead of performing algebraic inversion in the frequency domain, a time domain application could be feasible that would reduce the processing time before displaying the images. One of the main objections for the algebraic inversion methods for MRI applications is high computational load and long processing times before the image is available for the physician.

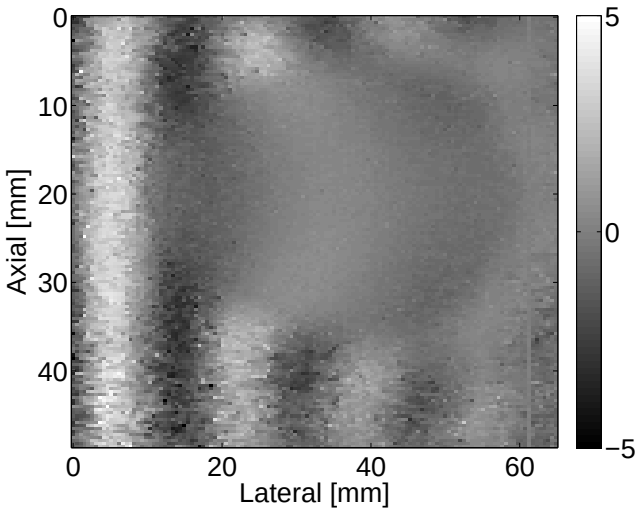

Figure C.2: An image of EKF filtered particle velocities. Bright and dark regions indicate particle velocities toward and away from the Doppler probe. The velocity range displayed is between -5 and +5 mm/s.

APPENDIX D

ACADEMIC ACHIEVEMENTS

This appendix reflects significant academic achievements produced by the candidate during the course of his graduate education. These achievements include published peer-reviewed papers, conference proceedings papers and presentations, awards, a grant for computational time, a patent application and an invited talk. These accomplishments are listed below.

D.1 Peer-reviewed Journal Publications

- **M. Orescanin**, Y. Wang, and M. F. Insana, "3-D FDTD simulation of shear waves for evaluation of complex modulus imaging," *IEEE Transactions on Ultrasonics, Ferroelectrics and Frequency Control*, accepted for publication.
- **M. Orescanin**, M. A. Qayyum, K. S. Toohey, and M. F. Insana, "Dispersion and shear modulus measurements of porcine liver," *Ultrasonic Imaging*, accepted for publication.
- **M. Orescanin** and M. F. Insana, "Shear modulus estimation with vibrating needle stimulation," *IEEE Transactions on Ultrasonics, Ferroelectrics and Frequency Control*, vol. 57, no. 6, pp. 1358-1367, 2010.
- X. Liang, **M. Orescanin**, K. S. Toohey, M. F. Insana, and S. A. Boppart "Acoustomotive optical coherence elastography for measuring material mechanical properties," *Optics Letters*, vol. 34, no. 19, pp. 2894-2896, 2009.
- **M. Orescanin**, K. S. Toohey, and M. F. Insana, "Material properties from acoustic radiation force step response," The Journal of the Acoustical Society of America, vol. 125, no. 5, pp. 2928-2936, 2009.

- T.-Y. Yu, **M. Orescanin**, C. D. Curtis, D. S. Zrnic, and D. E. Forsyth, "Beam multiplexing using the phased array weather radar", *Journal of Atmospheric and Oceanic Technology*, vol. 24 , no. 4, pp. 616- 626, 2007.

D.2 Conference Proceedings and Presentations

- **M. Orescanin**, and M. F. Insana, "Bayesian reconstruction of complex shear modulus images," *Proc. IEEE International Ultrasonics Symposium*, San Diego, October 2010.
- **M. Orescanin**, and Y. Wang, and M. F. Insana, "3D shear wave imaging: A simulation and experimental study," *Proc. IEEE International Ultrasonics Symposium*, San Diego, October 2010.
- Y. Wang, **M. Orescanin**, and M. F. Insana. "In vivo measurement of the complex shear modulus of rat mammary tumors using shear wave imaging techniques," *Proc. IEEE Engineering in Medicine and Biology Society*, Buenos Aires, August 2010.
- J. Sanchez, **M. Orescanin**, and M. Oelze, "Improving image contrast using coded excitation for ultrasonic imaging," *Proc. IEEE Electro-Information Technology Conference*, Bloomington, May 2010.
- **M. Orescanin**, M. A. Qayyum, K. S. Toohey and M. F. Insana, "Quantitative estimation of complex shear modulus of liver and hydrogels through shear-wave imaging," *Acoustical Society of America 158th meeting*, San Antonio, October 2009.
- **M. Orescanin**, K. S. Toohey, and M. F. Insana, "Quantitative shear wave imaging of cell culture gels," *Proc. IEEE International Ultrasonics Symposium*, Rome, September 2009.
- **M. Orescanin**, M. Qayyum, K. Toohey, and M. Insana, "Complex shear modulus of thermally-damaged liver," *Proc IEEE International Ultrasonics Symposium*, Rome, September 2009.
- R. J. Lavarello, M. L. Oelze, M. Berggren, S. Johnson, M. Orescanin, R. Yapp,"Implementation of Scatterer Size Imaging on an Ultrasonic

Breast Tomography Scanner," *Proc IEEE International Ultrasonics Symposium*, Rome, September 2009.

- X. Liang, V. Crecea, M. Orescanin, M. F. Insana, S. A. Boppart, "In vivo application of dynamic optical coherence elastography," *Engineering Conferences International: Advances in Optics for Biotechnology, Medicine, and Surgery XI: Clinical Challenges and Research Solutions*, Burlington, VT, June 2009.

- M. F. Insana, **M. Orescanin**, J. Xu, and R. D. Yapp, "On the mechanisms producing elasticity imaging contrast in breast cancer," *Ultrasonic Imaging and Tissue Characterization*, 34th International Symposium, Arlington VA, June 2009.

- **M. Orescanin**, K. S. Toohey and M. F. Insana, "Bio-material evaluation using ultrasound radiation force", *Society of Engineering Science*, 45th meeting, October 2008.

- K. S. Toohey, **M. Orescanin** and M. F. Insana, "Determining material properties from an oscillating sphere in viscoelastic media," *Society of Engineering Science*, 45th meeting, October 2008.

- X. Liang, A. L. Oldenburg, V. Crecea, **M. Orescanin**, M. F. Insana and S. A. Boppart, "Measuring tissue mechanical properties using dynamic optical coherence elastography," *Biomedical Engineering Society 2008 Annual Meeting*, Saint Louis, October 2008.

- V. Crecea , A. L. Oldenburg, X. Liang, T. S. Ralston, **M. Orescanin**, M. F. Insana, and S. A. Boppart, "Magnetomotive optical coherence elastography for measuring biomechanical properties of tissue using magnetic nanoparticles," *American Physical Society Annual Meeting*, New Orleans, LA, March 10-14, 2008.

- **M. Orescanin**, D. Mahr, K. S. Toohey, S. Kalyanam and M. F. Insana, "Acoustic radiation force biorheology", *Acoustical Society of America 154th meeting*, New Orleans, November 2007.

- **M. Orescanin** and M. F. Insana, "Ultrasonic radiation forces for elasticity imaging of 3-D tissue models", *Proc. SPIE*, vol. 6513, pp.OH1-11 , San Diego, February 2007.

- T.-Y. Yu, **M. Orescanin**, C. D. Curtis, D. S. Zrnic, and D. E. Forsyth, "Optimization of weather update time and data quality using phased-array radar," *23rd Conference on International Interactive Information and Processing Systems (IIPS)*, January 2007.

- **M. Orescanin**, T.-Y. Yu, C. D. Curtis, D. S. Zrnic and D. E. Forsyth, "Signal processing of beam-multiplexed data from phased-array weather radar", *Proc. 32nd Conference on Radar Meteorology*, Albuquerque, October 2005.

D.3 Patent Application

A method that utilized portions of this dissertation work has been used to apply for a patent with the United States Patent and Trademark Office, assigned Publication No. US-2010-0191110-A1 July 29, 2010.

"Techniques to Evaluate Mechanical Properties of a Biologic Material," Michael F. Insana, **Marko Orescanin** and Kathleen Toohey.

D.4 Academic Awards

In conjunction with presenting portions of this thesis work, I was awarded a Student Travel Award by the College of Engineering of the University of Illinois at Urbana-Champaign to attend the 2009 IEEE International Ultrasonics Symposium.

During my M.S. work at the University of Oklahoma, Norman, OK, I received the Spiros G. Geotis Prize, for the year 2006, of the American Meteorological Society (AMS) for the paper "Signal processing of beam-multiplexed data from phased-array weather radar."

D.5 Invited Talks

M. Orescanin, "Ultrasound shear wave imaging," Bradley University, Peoria, IL, April 15, 2010.

D.6 Grant

I am a co-PI on the grant for computational resources by National Science Foundation through TeraGrid resources under grant number [TG-DMR080068N].

REFERENCES

[1] K. L. Mathis, T. L. Hoskin, J. C. Boughey, B. S. Crownhart, K. R. Brandt, C. M. Vachon, C. S. Grant, and A. C. Degnim, "Palpable Presentation of Breast Cancer Persists in the Era of Screening Mammography," *Journal of the American College of Surgeons*, vol. 210, no. 3, pp. 314–318, 2010.

[2] D. Saslow, J. Hannan, J. Osuch, M. Alciati, C. Baines, M. Barton, J. Bobo, C. Coleman, M. Dolan, G. Gaumer et al., "Clinical breast examination: practical recommendations for optimizing performance and reporting," *CA: A Cancer Journal for Clinicians*, vol. 54, no. 6, p. 327, 2004.

[3] Y. Qiu, M. Sridhar, J. K. Tsou, K. K. Lindfors, and M. F. Insana, "Ultrasonic viscoelasticity imaging of nonpalpable breast tumors: preliminary results," *Academic Radiology*, vol. 15, no. 12, pp. 1526–1533, 2008.

[4] S. Kalyanam, R. D. Yapp, and M. F. Insana, "Poro-viscoelastic behavior of gelatin hydrogels under compression-implications for bioelasticity imaging," *Journal of Biomechanical Engineering*, vol. 131, p. 081005, 2009.

[5] M. S. Keralapura, "Imaging viscoelasticity in hydropolymers and breast tissue with ultrasound," Ph.D. dissertation, University of California, Davis, 2007.

[6] R. S. Gieni and M. J. Hendzel, "Mechanotransduction from the ECM to the genome: Are the pieces now in place?" *Journal of Cellular Biochemistry*, vol. 104, no. 6, pp. 1964–1987, 2008.

[7] A. Itoh, E. Ueno, E. Tohno, H. Kamma, H. Takahashi, T. Shiina, M. Yamakawa, and T. Matsumura, "Breast disease: clinical application of US elastography for diagnosis," *Radiology*, vol. 239, no. 2, p. 341, 2006.

[8] L. Castéra, J. Vergniol, J. Foucher, B. Le Bail, E. Chanteloup, M. Haaser, M. Darriet, P. Couzigou, and V. de Lédinghen, "Prospective comparison of transient elastography, Fibrotest, APRI, and liver

biopsy for the assessment of fibrosis in chronic hepatitis C," *Gastroenterology*, vol. 128, no. 2, pp. 343–350, 2005.

[9] L. Huwart, C. Sempoux, N. Salameh, J. Jamart, L. Annet, R. Sinkus, F. Peeters, L. C. ter Beek, Y. Horsmans, and B. E. Van Beers, "Liver fibrosis: Noninvasive assessment with MR elastography versus aspartate aminotransferase–to-platelet ratio index," *Radiology*, vol. 245, no. 2, p. 458, 2007.

[10] I. Sack, J. Rump, T. Elgeti, A. Samani, and J. Braun, "MR elastography of the human heart: Noninvasive assessment of myocardial elasticity changes by shear wave amplitude variations," *Magnetic Resonance in Medicine*, vol. 61, no. 3, pp. 668–677, 2009.

[11] R. Weiss, V. Egorov, S. Ayrapetyan, N. Sarvazyan, and A. Sarvazyan, "Prostate mechanical imaging: A new method for prostate assessment," *Urology*, vol. 71, no. 3, p. 425, 2008.

[12] I. Sack, B. Beierbach, J. Wuerfel, D. Klatt, U. Hamhaber, S. Papazoglou, P. Martus, and J. Braun, "The impact of aging and gender on brain viscoelasticity," *NeuroImage*, vol. 46, no. 3, pp. 652–657, 2009.

[13] D. E. Discher, P. Janmey, and Y. Wang, "Tissue cells feel and respond to the stiffness of their substrate," *Science*, vol. 310, no. 5751, p. 1139, 2005.

[14] T. A. Krouskop, P. S. Younes, S. Srinivasan, T. Wheeler, and J. Ophir, "Differences in the compressive stress-strain response of infiltrating ductal carcinomas with and without lobular features– Implications for mammography and elastography," *Ultrasonic Imaging*, vol. 25, no. 3, pp. 162–170, 2003.

[15] G. M. Baxter, P. L. P. Allan, and P. Morley, *Clinical Diagnostic Ultrasound*. Malden, MA: Wiley-Blackwell, 1999.

[16] A. P. Sarvazyan, O. V. Rudenko, S. D. Swanson, J. B. Fowlkes, and S. Y. Emelianov, "Shear wave elasticity imaging: A new ultrasonic technology of medical diagnostics," *Ultrasound in Medicine & Biology*, vol. 24, no. 9, pp. 1419–1435, 1998.

[17] J. F. Greenleaf, M. Fatemi, and M. F. Insana, "Selected methods for imaging elastic properties of biological tissues," *Annual Review of Biomedical Engineering*, vol. 5, p. 57, 2003.

[18] S. Chen, M. W. Urban, C. Pislaru, R. Kinnick, Y. Zheng, A. Yao, and J. F. Greenleaf, "Shearwave dispersion ultrasound vibrometry (SDUV) for measuring tissue elasticity and viscosity," *IEEE Transactions on*

Ultrasonics, Ferroelectrics and Frequency Control, vol. 56, no. 1, pp. 55–62, 2009.

[19] M. Orescanin, K. S. Toohey, and M. F. Insana, "Material properties from acoustic radiation force step response," *Journal of the Acoustical Society of America*, vol. 125, no. 5, pp. 2928–2936, 2009.

[20] M. Orescanin and M. F. Insana, "Shear modulus estimation with vibrating needle stimulation," *IEEE Transactions on Ultrasonics, Ferroelectrics, and Frequency Control*, vol. 57, no. 6, pp. 1358–1367, June 2010.

[21] B. J. Fahey, S. J. Hsu, P. D. Wolf, R. C. Nelson, and G. E. Trahey, "Liver ablation guidance with acoustic radiation force impulse imaging: Challenges and opportunities," *Physics in Medicine and Biology*, vol. 51, no. 15, pp. 3785–3808, 2006.

[22] A. Manduca, T. E. Oliphant, M. A. Dresner, J. L. Mahowald, S. A. Kruse, E. Amromin, J. P. Felmlee, J. F. Greenleaf, and R. L. Ehman, "Magnetic resonance elastography: Non-invasive mapping of tissue elasticity," *Medical Image Analysis*, vol. 5, no. 4, pp. 237–254, 2001.

[23] R. Sinkus, K. Siegmann, T. Xydeas, M. Tanter, C. Claussen, and M. Fink, "MR elastography of breast lesions: Understanding the solid/liquid duality can improve the specificity of contrast-enhanced MR mammography," *Magnetic Resonance in Medicine*, vol. 58, no. 6, pp. 1135–1144, 2007.

[24] K. R. Nightingale, M. L. Palmeri, R. W. Nightingale, and G. E. Trahey, "On the feasibility of remote palpation using acoustic radiation force," *Journal of the Acoustical Society of America*, vol. 110, p. 625, 2001.

[25] A. Oldenburg, F. Toublan, K. Suslick, A. Wei, and S. Boppart, "Magnetomotive contrast for in vivo optical coherence tomography," *Optics Express*, vol. 13, no. 17, pp. 6597–6614, 2005.

[26] J. Bercoff, M. Tanter, and M. Fink, "Supersonic shear imaging: a new technique for soft tissue elasticity mapping," *IEEE Transactions on Ultrasonics, Ferroelectrics, and Frequency Control*, vol. 51, no. 4, pp. 396–409, 2004.

[27] Q. C. C. Chan, G. Li, R. L. Ehman, R. C. Grimm, R. Li, and E. S. Yang, "Needle shear wave driver for magnetic resonance elastography," *Magnetic Resonance in Medicine*, vol. 55, no. 5, pp. 1175–1179, 2006.

[28] P. J. McCracken, A. Manduca, J. Felmlee, and R. L. Ehman, "Mechanical transient-based magnetic resonance elastography," *Magnetic Resonance in Medicine*, vol. 53, no. 3, pp. 628–639, 2005.

[29] R. Sinkus, M. Tanter, T. Xydeas, S. Catheline, J. Bercoff, and M. Fink, "Viscoelastic shear properties of in vivo breast lesions measured by MR elastography," *Magnetic Resonance Imaging*, vol. 23, no. 2, pp. 159–165, 2005.

[30] K. C. Siegmann, T. Xydeas, R. Sinkus, B. Kraemer, U. Vogel, and C. D. Claussen, "Diagnostic value of MR elastography in addition to contrast-enhanced MR imaging of the breast–initial clinical results," *European Radiology*, vol. 20, no. 2, pp. 318–325, 2010.

[31] S. K. Venkatesh, Y. Meng, J. F. Glockner, N. Takahashi, P. A. Araoz, J. A. Talwalkar, and R. L. Ehman, "MR elastography of liver tumors: Preliminary results," *American Journal of Roentgenology*, vol. 190, no. 6, pp. 1534–1540, 2008.

[32] J. L. Gennisson, T. Deffieux, E. Macé, G. Montaldo, M. Fink, and M. Tanter, "Viscoelastic and anisotropic mechanical properties of in vivo muscle tissue assessed by supersonic shear imaging," *Ultrasound in Medicine & Biology*, vol. 36, no. 5, pp. 789–801, 2010.

[33] S. Catheline, J. L. Gennisson, G. Delon, M. Fink, R. Sinkus, S. Abouelkaram, and J. Culioli, "Measurement of viscoelastic properties of homogeneous soft solid using transient elastography: An inverse problem approach," *Journal of the Acoustical Society of America*, vol. 116, pp. 3734–3741, 2004.

[34] M. Yin, J. Woollard, X. Wang, V. E. Torres, P. C. Harris, C. J. Ward, K. J. Glaser, A. Manduca, and R. L. Ehman, "Quantitative assessment of hepatic fibrosis in an animal model with magnetic resonance elastography," *Magnetic Resonance in Medicine*, vol. 58, no. 2, pp. 346–353, 2007.

[35] T. Hasegawa, "Acoustic-radiation force on a solid elastic sphere," *Journal of the Acoustical Society of America*, vol. 46, pp. 1139–1143, 1969.

[36] G. R. Torr, "The acoustic radiation force," *American Journal of Physics*, vol. 52, pp. 402–408, 1984.

[37] Y. A. Ilinskii, G. D. Meegan, E. A. Zabolotskaya, and S. Y. Emelianov, "Gas bubble and solid sphere motion in elastic media in response to acoustic radiation force," *Journal of the Acoustical Society of America*, vol. 117, pp. 2338–2346, 2005.

[38] S. Chen, M. Fatemi, and J. F. Greenleaf, "Remote measurement of material properties from radiation force induced vibration of an embedded sphere," *Journal of the Acoustical Society of America*, vol. 112, pp. 884–889, 2002.

[39] T. Deffieux, G. Montaldo, M. Tanter, and M. Fink, "Shear wave spectroscopy for in vivo quantification of human soft tissues visco-elasticity." *IEEE Transactions on Medical Imaging*, vol. 28, no. 3, pp. 313–322, 2009.

[40] C. Fierbinteanu-Braticevici, D. Andronescu, R. Usvat, D. Cretoiu, C. Baicus, and G. Marinoschi, "Acoustic radiation force imaging sonoelastography for noninvasive staging of liver fibrosis," *World Journal of Gastroenterology: WJG*, vol. 15, no. 44, pp. 5525–5532, 2009.

[41] C. I. D. Branch, "Information for Manufacturers Seeking Marketing Clearance of Diagnostic Ultrasound Systems and Transducers."

[42] K. F. Graff, *Wave Motion in Elastic Solids*. Mineola, NY:Dover, 1991.

[43] S. A. Goss, R. L. Johnston, and F. Dunn, "Comprehensive compilation of empirical ultrasonic properties of mammalian tissues," *Journal of the Acoustical Society of America*, vol. 64, pp. 423–457, 1978.

[44] S. A. Goss, R. L. Johnston, and F. Dunn, "Compilation of empirical ultrasonic properties of mammalian tissues. II," *Journal of the Acoustical Society of America*, vol. 68, pp. 93–108, 1980.

[45] J. M. Mamou, "Ultrasonic characterization of three animal mammary tumors from three-dimensional acoustic tissue models," Ph.D. dissertation, University of Illinois at Urbana-Champaign, 2005.

[46] F. A. Duck, *Physical Properties of Tissue: A Comprehensive Reference Book*. San Diego, CA: Academic Press, 1990.

[47] I. M. Ward and P. R. Pinnock, "Review Articles: The mechanical properties of solid polymers," *British Journal of Applied Physics*, vol. 17, pp. 3–32, 1966.

[48] S. Chen, M. Fatemi, and J. F. Greenleaf, "Quantifying elasticity and viscosity from measurement of shear wave speed dispersion," *Journal of the Acoustical Society of America*, vol. 115, pp. 2781–2785, 2004.

[49] M. Orescanin, M. A. Qayyum, K. S. Toohey, and M. F. Insana, "Dispersion and shear modulus measurements of porcine liver," *Ultrasonic Imaging*, 2010, accepted for publication.

[50] M. Sridhar, J. Liu, and M. F. Insana, "Elasticity imaging of polymeric media," *Journal of Biomechanical Engineering*, vol. 129, no. 2, pp. 259–272, 2007.

[51] M. Orescanin and M. F. Insana, "Ultrasonic radiation forces for elasticity imaging of 3-D tissue models," in *Society of Photo-Optical Instrumentation Engineers (SPIE) Conference Series*, vol. 6513, 2007, p. 15.

[52] X. Liang, M. Orescanin, K. S. Toohey, M. F. Insana, and S. A. Boppart, "Acoustomotive optical coherence elastography for measuring material mechanical properties," *Optics Letters*, vol. 34, no. 19, pp. 2894–2896, 2009.

[53] M. F. Insana and M. Oelze, "Advanced ultrasonic imaging techniques for breast cancer research," *Emerging Technologies in Breast Imaging and Mammography*, pp. 141–160.

[54] F. Dunn, A. J. Averbuch, and W. D. O'Brien Jr., "A primary method for the determination of ultrasonic intensity with the elastic sphere radiometer," *Acustica*, vol. 38, no. 1, pp. 58–61, 1977.

[55] S. Chen, G. T. Silva, R. R. Kinnick, J. F. Greenleaf, and M. Fatemi, "Measurement of dynamic and static radiation force on a sphere," *Physical Review E*, vol. 71, no. 5, p. 56618, 2005.

[56] J. A. Jensen, *Estimation of Blood Velocities Using Ultrasound: A Signal Processing Approach.* New York, NY: Cambridge University Press, 1996.

[57] R. J. Doviak and D. S. Zrnic, *Doppler Radar and Weather Observations.* Maniola, NY: Dover Publications, Inc., 2006.

[58] L. E. Kinsler, *Fundamentals of Acoustics.* Hoboken, NJ: John Wiley & Sons Inc, 1999.

[59] A. Alizad, M. Fatemi, L. E. Wold, and J. F. Greenleaf, "Performance of vibro-acoustography in detecting microcalcifications in excised human breast tissue: a study of 74 tissue samples," *IEEE Transactions on Medical Imaging*, vol. 23, no. 3, pp. 307–312, 2004.

[60] M. Sridhar and M. F. Insana, "Ultrasonic measurements of breast viscoelasticity," *Medical Physics*, vol. 34, no. 12, pp. 4757–4767, 2007.

[61] M. Fatemi and J. F. Greenleaf, "Ultrasound-stimulated vibro-acoustic spectrography," *Science*, vol. 280, no. 5360, pp. 82–85, 1998.

[62] E. A. Barannik, A. Girnyk, V. Tovstiak, A. I. Marusenko, S. Y. Emelianov, and A. P. Sarvazyan, "Doppler ultrasound detection of shear waves remotely induced in tissue phantoms and tissue in vitro," *Ultrasonics*, vol. 40, no. 1-8, pp. 849–852, 2002.

[63] E. E. Konofagou and K. Hynynen, "Localized harmonic motion imaging: theory, simulations and experiments," *Ultrasound in Medicine & Biology*, vol. 29, no. 10, pp. 1405–1413, 2003.

[64] J. Xu, "Characterization and modeling of cell activation upon TGF-beta 1 stimulation in a 3-D culture system," M.S. thesis, University of Illinois, 2010.

[65] J. D. Ferry, *Viscoelastic Properties of Polymers.* John Wiley & Sons Inc, 1980.

[66] B. Fabry, G. Maksym, J. Butler, M. Glogauer, D. Navajas, N. A. Taback, E. J. Millet, and J. J. Fredberg, "Time scale and other invariants of integrative mechanical behavior in living cells," *Physical Review E*, vol. 68, no. 4, pp. 41 914–1–18, 2003.

[67] E. L. Madsen, J. A. Zagzebski, and G. R. Frank, "Oil-in-gelatin dispersions for use as ultrasonically tissue-mimicking materials," *Ultrasound in Medicine & Biology*, vol. 8, no. 3, pp. 277–287, 1982.

[68] M. Ashfaq, S. S. Brunke, J. J. Dahl, H. Ermert, C. Hansen, and M. F. Insana, "An ultrasound research interface for a clinical system," *IEEE Transactions on Ultrasonics, Ferroelectrics, and Frequency Control*, vol. 53, no. 10, pp. 1759–1771, 2006.

[69] A. W. Al-Khafaji and J. R. Tooley, *Numerical Methods in Engineering Practice.* Oxford University Press, USA, 1986.

[70] H. Lamb, *Hydrodynamics.* Cambridge Univ Pr, 1932.

[71] P. Kundu, I. M. Cohen, and H. H. Hu, *Fluid Mechanics.* Academic Press, 2004.

[72] A. C. Cameron and F. A. G. Windmeijer, "R-squared measures for count data regression models with applications to health-care utilization," *Journal of Business & Economic Statistics*, pp. 209–220, 1996.

[73] P. M. Gilsenan and S. B. Ross-Murphy, "Shear creep of gelatin gels from mammalian and piscine collagens," *International Journal of Biological Macromolecules*, vol. 29, no. 1, pp. 53–61, 2001.

[74] S. R. Aglyamov, A. B. Karpiouk, Y. A. Ilinskii, E. A. Zabolotskaya, and S. Y. Emelianov, "Motion of a solid sphere in a viscoelastic medium in response to applied acoustic radiation force: Theoretical analysis and experimental verification," *Journal of the Acoustical Society of America*, vol. 122, no. 4, pp. 1927–1936, 2007.

[75] J. J. M. Carcione, *Wave Fields in Real Media: Wave Propagation in Anisotropic, Anelastic, Porous and Electromagnetic Media, Handbook of Geophysical Exploration, Seismic Exploration, (Revised and Extended), Vol. 38, edsHelbig K. and Treitel, S.* Elsevier Ltd, Oxford, UK, Amsterdam, The Netherlands, 2007.

[76] J. Vappou, C. Maleke, and E. E. Konofagou, "Quantitative viscoelastic parameters measured by harmonic motion imaging," *Physics in Medicine & Biology*, vol. 54, pp. 3579–3594, 2009.

[77] H. Kanai, "Propagation of spontaneously actuated pulsive vibration in human heart wall and in vivo viscoelasticity estimation," *IEEE Transactions on Ultrasonics, Ferroelectrics, and Frequency Control*, vol. 52, no. 11, pp. 1931–1942, 2005.

[78] V. Dutt, R. Kinnick, R. Muthupillai, T. Oliphant, R. Ehman, and J. Greenleaf, "Acoustic shear-wave imaging using echo ultrasound compared to magnetic resonance elastography," *Ultrasound in Medicine & Biology*, vol. 26, no. 3, pp. 397–403, 2000.

[79] C. Kasai, K. Namekawa, A. Koyano, and R. Omoto, "Real-time two-dimensional blood flow imaging using an autocorrelation technique," *IEEE Transactions on Sonics and Ultrasonics*, vol. 32, no. 3, pp. 458–464, 1985.

[80] P. T. May, T. Sato, M. Yamamoto, S. Kato, T. Tsuda, and S. Fukao, "Errors in the Determination of Wind Speed by Doppler Radar," *Journal of Atmospheric and Oceanic Technology*, vol. 6, pp. 235–242, 1989.

[81] M. Abramovitz and I. Stegun, *Handbook of Mathematical Functions.* Dover, New York, 1972.

[82] K. R. Rajagopal and A. S. Wineman, "A quasi-correspondence principle for Quasi-Linear viscoelastic solids," *Mechanics of Time-Dependent Materials*, vol. 12, no. 1, pp. 1–14, 2008.

[83] L. Khazanovich, "The elastic-viscoelastic correspondence principle for non-homogeneous materials with time translation non-invariant properties," *International Journal of Solids and Structures*, vol. 45, no. 17, pp. 4739–4747, 2008.

[84] E. L. Madsen, H. J. Sathoff, and J. A. Zagzebski, "Ultrasonic shear wave properties of soft tissues and tissuelike materials," *Journal of the Acoustical Society of America*, vol. 74, pp. 1346–1355, 1983.

[85] K. Hoyt, K. J. Parker, and D. J. Rubens, "Real-time shear velocity imaging using sonoelastographic techniques," *Ultrasound in Medicine & Biology*, vol. 33, no. 7, pp. 1086–1097, 2007.

[86] R. C. Aster, C. H. Thurber, and B. Borchers, *Parameter Estimation and Inverse Problems.* Academic Press, 2005.

[87] P. R. Mahapatra and D. S. Zrnic, "Practical algorithms for mean velocity estimation in pulse Doppler weather radars using a small number of samples," *IEEE Transactions on Geoscience and Remote Sensing*, pp. 491–501, 1983.

[88] C. Kargel, G. Plevnik, B. Trummer, and M. F. Insana, "Doppler ultrasound systems designed for tumor blood flow imaging," *IEEE Transactions on Instrumentation and Measurement*, vol. 53, no. 2, pp. 524–536, 2004.

[89] N. W. Tschoegl, *The Phenomenological Theory of Linear Viscoelastic Behavior: An Introduction.* Springer, 1989.

[90] A. Karpiouk, S. Aglyamov, Y. Ilinskii, E. Zabolotskaya, and S. Emelianov, "Assessment of shear modulus of tissue using ultrasound radiation force acting on a spherical acoustic inhomogeneity," *IEEE Transactions on Ultrasonics, Ferroelectrics, and Frequency Control*, vol. 56, no. 11, pp. 2380–2387, 2009.

[91] B. J. Fahey, R. C. Nelson, S. J. Hsu, D. P. Bradway, D. M. Dumont, and G. E. Trahey, "In vivo guidance and assessment of liver radiofrequency ablation with acoustic radiation force elastography," *Ultrasound in Medicine & Biology*, vol. 34, no. 10, pp. 1590–1603, 2008.

[92] D. T. Butcher, T. Alliston, and V. M. Weaver, "A tense situation: forcing tumour progression," *Nature Reviews Cancer*, vol. 9, no. 2, pp. 108–122, 2009.

[93] T. Stylianopoulos, A. Aksan, and V. H. Barocas, "A Structural, Kinetic Model of Soft Tissue Thermomechanics," *Biophysical Journal*, vol. 94, no. 3, pp. 717–725, 2008.

[94] P. Asbach, D. Klatt, U. Hamhaber, J. Braun, R. Somasundaram, B. Hamm, and I. Sack, "Assessment of liver viscoelasticity using multifrequency MR elastography," *Magnetic Resonance in Medicine*, vol. 60, no. 2, pp. 373–379, 2008.

[95] G. D. Ludwig, "The Velocity of Sound through Tissues and the Acoustic Impedance of Tissues," *Journal of the Acoustical Society of America*, vol. 22, pp. 862–866, 1950.

[96] A. E. Kerdok, M. P. Ottensmeyer, and R. D. Howe, "Effects of perfusion on the viscoelastic characteristics of liver," *Journal of Biomechanics*, vol. 39, no. 12, pp. 2221–2231, 2006.

[97] Z. Liua and L. E. Bilstonb, "Large deformation shear properties of liver tissue," *Biorheology*, vol. 39, no. 6, pp. 735–742, 2002.

[98] S. A. Curley and F. Izzo, "Radiofrequency ablation of primary and metastatic hepatic malignancies," *International Journal of Clinical Oncology*, vol. 7, no. 2, pp. 72–81, 2002.

[99] F. Kallel, R. J. Stafford, R. E. Price, R. Righetti, J. Ophir, and J. D. Hazle, "The feasibility of elastographic visualization of HIFU-induced thermal lesions in soft tissues," *Ultrasound in Medicine & Biology*, vol. 25, no. 4, pp. 641–647, 1999.

[100] F. L. Lizzi, R. Muratore, C. X. Deng, J. A. Ketterling, S. K. Alam, S. Mikaelian, and A. Kalisz, "Radiation-force technique to monitor lesions during ultrasonic therapy," *Ultrasound in Medicine & Biology*, vol. 29, no. 11, pp. 1593–1605, 2003.

[101] M. Z. Kiss, M. J. Daniels, and T. Varghese, "Investigation of temperature-dependent viscoelastic properties of thermal lesions in@@ iex vivo@ animal liver tissue," *Journal of Biomechanics*, vol. 42, no. 8, pp. 959–966, 2009.

[102] L. A. Frizzell, E. L. Carstensen, and J. F. Dyro, "Shear properties of mammalian tissues at low megahertz frequencies," *Journal of the Acoustical Society of America*, vol. 60, pp. 1409–1411, 1976.

[103] T. L. Szabo and J. Wu, "A model for longitudinal and shear wave propagation in viscoelastic media," *Journal of the Acoustical Society of America*, vol. 107, pp. 2437–2446, 2000.

[104] N. Akashi, J. Kushibiki, N. Chubachi, and F. Dunn, "Acoustic properties of selected bovine tissues in the frequency range 20-200 MHz," *Journal of the Acoustical Society of America*, vol. 98, pp. 3035–3039, 1995.

[105] T. E. Oliphant, R. R. Kinnick, A. Manduca, R. L. Ehman, and J. F. Greenleaf, "An error analysis of helmholtz inversion for incompressible shear, vibration elastography with application to filter-design for tissue characterization," vol. 2, oct. 2000, pp. 1795 –1798 vol.2.

[106] S. Papazoglou, U. Hamhaber, J. Braun, and I. Sack, "Algebraic Helmholtz inversion in planar magnetic resonance elastography," *Physics in Medicine & Biology*, vol. 53, pp. 3147–3158, 2008.

[107] J. Virieux, "P-SV wave propagation in heterogeneous media: Velocity-stress finite-difference method," *Geophysics*, vol. 51, pp. 889–901, 1986.

[108] P. Moczo, "3D Heterogeneous Staggered-Grid Finite-Difference Modeling of Seismic Motion with Volume Harmonic and Arithmetic Averaging of Elastic Moduli and Densities," *Bulletin of the Seismological Society of America*, vol. 92, pp. 3042–3066, 2002.

[109] C. T. Schroder and W. R. Scott Jr, "A finite-difference model to study the elastic-wave interactionswith buried land mines," *IEEE Transactions on Geoscience and Remote Sensing*, vol. 38, no. 4 Part 1, pp. 1505–1512, 2000.

[110] D. R. Durran, *Numerical Methods for Wave Equations in Geophysical Fluid Dynamics.* Springer Verlag, 1999.

[111] J. B. Freund, "Proposed inflow/outflow boundary condition for direct computation of aerodynamic sound," *Journal of American Institute of Aeronautics and Astronautics*, vol. 35, no. 4, pp. 740–742, 1997.

[112] A. Giannoula and R. S. C. Cobbold, "Narrowband Shear Wave Generation by a Finite-Amplitude Radiation Force: The Fundamental Component," *IEEE Transactions on Ultrasonics, Ferroelectrics, and Frequency Control*, vol. 55, no. 2, pp. 343–358, 2008.

[113] S. M. Kay, *Fundamentals of Statistical Signal Processing: Estimation Theory*, 1993.

[114] G. Evensen, *Data Assimilation: The Ensemble Kalman Filter.* Springer Verlag, 2009.

[115] Y. Zheng, S. Chen, W. Tan, R. Kinnick, and J. F. Greenleaf, "Detection of tissue harmonic motion induced by ultrasonic radiation force using pulse-echo ultrasound and kalman filter," *IEEE Transactions on Ultrasonics, Ferroelectrics, and Frequency Control*, vol. 54, no. 2, pp. 290 –300, feb. 2007.

[116] L. Dalong and E. S. Ebbini, "Viscoelastic property measurement in thin tissue constructs using ultrasound," *IEEE Transactions on Ultrasonics, Ferroelectrics, and Frequency Control*, vol. 55, no. 2, pp. 368 –383, feb. 2008.

[117] V. Chatdarong, "Multi-sensor rainfall data assimilation using ensemble approaches," Ph.D. dissertation, Massachusetts Institute of Technology, 2006.

[118] M. Tada, N. Nagai, and T. Maeno, "Material properties estimation of layered soft tissue based on MR observation and iterative FE simulation," *Medical Image Computing and Computer-Assisted Intervention–MICCAI 2005*, pp. 633–640, 2005.

[119] M. Zupanski, "Maximum likelihood ensemble filter: theoretical aspects," *Monthly Weather Review*, vol. 133, pp. 1710–1726, 2005.

[120] A. H. Jazwinski, *Stochastic Processes and Filtering Theory.* Dover Publications, Inc., 1998.

[121] A. C. Lorenc, "Analysis methods for numerical weather prediction," *Quarterly Journal of the Royal Meteorological Society*, vol. 112, no. 474, pp. 1177–1194, 1986.

[122] F. van der Heijden and D. de Ridder, *Classification, Parameter Estimation, and State Estimation: An Engineering Approach Using MATLAB.* John Wiley & Sons Inc, 2004.

[123] D. Simon, *Optimal State Estimation: Kalman, H [infinity] and Nonlinear approaches.* John Wiley and Sons, 2006.

[124] M. Zupanski, I. M. Navon, and D. Zupanski, "The Maximum Likelihood Ensemble Filter as a non-differentiable minimization algorithm," *Quarterly Journal of the Royal Meteorological Society*, vol. 134, no. 633, pp. 1039–1050, 2008.

[125] J. Liu, C. Abbey, and M. Insana, "Linear approach to axial resolution in elasticity imaging," *IEEE Transactions on Ultrasonics, Ferroelectrics and Frequency Control*, vol. 51, no. 6, pp. 716–725, 2004.

[126] R. S. C. Cobbold, *Foundations of Biomedical Ultrasound.* Oxford University Press, USA, 2007.

[127] P. J. Fish, "Nonstationarity broadening in pulsed Doppler spectrum measurements," *Ultrasound in Medicine & Biology*, vol. 17, no. 2, pp. 147–155, 1991.

[128] R. O. Duda, P. E. Hart, and D. G. Stork, *Pattern Classification.* Wiley-Interscience, 2000.

[129] S. M. Torres, C. D. Curtis, and J. R. Cruz, "Pseudowhitening of weather radar signals to improve spectral moment and polarimetric variable estimates at low signal-to-noise ratios," *IEEE Transactions on Geoscience and Remote Sensing*, vol. 42, no. 5, pp. 941–949, 2004.

[130] H. L. Oestreicher, "Field and impedance of an oscillating sphere in a viscoelastic medium with an application to biophysics," *Journal of the Acoustical Society of America*, vol. 23, pp. 707–714, 1951.

[131] A. N. Norris, "Impedance of a sphere oscillating in an elastic medium with and without slip," *Journal of the Acoustical Society of America*, vol. 119, pp. 2062–2066, 2006.

[132] D. G. Luenberger and Y. Ye, *Linear and Nonlinear Programming*. Springer Verlag, 2008.

AUTHOR'S BIOGRAPHY

Marko Oreščanin obtained his BS degree in Electrical and Computer Engineering at the University of Belgrade, in Belgrade, Serbia in 2003. He began his graduate studies in Electrical and Computer Engineering at the University of Oklahoma (OU) the following year. Mr. Oreščanin finished his masters thesis in the area of Doppler weather radar engineering in 2005 in collaboration with the National Severe Storms Laboratory and under supervision of Dr. Tian You-Yu (OU) and Dr. Dusan Zrnic (NSSL). He received the Spiros G. Geotis Prize in 2006 for his paper "Signal Processing of Beam Multiplexed Data for Phased Array Weather Radar" from the American Meteorological Society based on his work for MS thesis. In early 2006, he continued his graduate education at the University of Illinois at Urbana-Champaign. Here, he started working in the area of ultrasound shear wave imaging in the Ultrasonic Imaging Laboratory. He completed his PhD work in 2010 under direct supervision of Dr. Michael F. Insana. His research interests include ultrasonic imaging, pulsed Doppler imaging, remote sensing and data assimilation. Mr. Oreščanin is a student member of IEEE and the IEEE UFFC Society.